UC Berkeley
UC Berkeley Electronic Theses and Dissertations

Title

Reconstitution and Characterization of Membrane Proximal Signaling Downstream of the T Cell Receptor

Permalink

https://escholarship.org/uc/item/4f525190

Author

DeGrandchamp, Joseph B

Publication Date

2022

Peer reviewed|Thesis/dissertation

eScholarship.org Powered by the California Digital Library
University of California

Reconstitution and Characterization of Membrane Proximal Signaling Downstream of the T Cell Receptor

By

Joseph B. DeGrandchamp

A dissertation submitted in partial satisfaction of the

requirements for the degree of

Doctor of Philosophy

in

Chemistry

in the

Graduate Division

of the

University of California, Berkeley

Committee in charge:

Professor Jay T. Groves, Chair
Professor Ke Xu
Professor Andreas Martin

Fall 2022

Reconstitution and Characterization of Membrane Proximal Signaling Downstream of the T Cell Receptor

Copyright 2022 by
Joseph B. DeGrandchamp

Abstract

Reconstitution and Characterization of Membrane Proximal Signaling Downstream of the T Cell Receptor

by

Joseph B. DeGrandchamp

Doctor of Philosophy in Chemistry

University of California, Berkeley

Professor Jay T. Groves, Chair

Early warning signals in the adaptive immune system originate from T Cell recognition of pathogenic antigens on the surface of Antigen Presenting Cells (APCs). T Cell activation and the production of warning molecules (cytokines) proceeds downstream of antigen binding to T Cell Receptor (TCR) at T Cell:APC membrane interfaces. Complex proofreading mechanisms are required to control T Cell activation, and this process is thought to take place primarily via TCR proximal signaling events on the inner T Cell membrane. A number of critical components for the origination of T Cell activation signals are well known, including the membrane-associated scaffold LAT that becomes phosphorylated following TCR-antigen binding events. LAT recruits a web of cytosolic adapters, like Grb2, and signaling enzymes, such as Sos1 and PLCγ1. LAT has been recognized as a signaling hub wherefrom both proliferation signals, through Sos1 activation of Ras, and cytokine production signals, through PLCγ1-mediated Calcium flux, diverge. Additionally, this hub has been established as a biomolecular membrane protein condensate, with multivalent crosslinking through Grb2 and Sos1 interactions as well as more recently discovered crosslinking through Grb2 dimerization and the SH array of PLCγ1. The consequences of condensation are not yet fully understood, but in new accounts from our lab, it has been suggested to encode information relevant for T Cell activation. Vital to the study of this system, we have established an *in vitro* platform for the study of fluorescently labeled proteins on supported bilayers with visualization through TIRF microscopy. LAT functionalized to these bilayers is capable of both recruitment of solution proteins and forming condensates, and signals from recruited enzymes can be detected using labeled biosensors. This allows for the piece-wise investigation of mechanisms in the formation of this central hub. Herein, I cover our recent efforts to increase reproducibility in the use of this platform and expound on the recent developments in the modes of LAT crosslinking leading to condensation. Then, I demonstrate the effect of LAT condensation on active PLCγ1 from mammalian cell lysate, most notably a marked decrease in activity in pLAT:Grb2 condensates. I conclude with single particle tracking experiments of two Ras isoforms that reveal functional differences in their interactions with the membrane as a function of lipid composition. These stand to be important contributions to the understanding of TCR signaling and will empower future discovery.

To the memory of my loving mother,
Renee DeGrandchamp.

Contents

Contents ii

List of Figures iv

Acknowledgments v

1 Introduction 1

2 Novel modes and increased reproducibility of *in vitro* LAT condensation 6
2.1 Abstract . . . 6
2.2 Introduction . . . 7
2.3 Standardizing *in vitro* LAT condensation experiments . . . 8
The basics of LAT condensation on supported bilayers . . . 8
A new LAT construct for more consistent experiments . . . 10
2.4 Intricacies in the Grb2 dimer mediated condensation of LAT . . . 12
Separating a metastable, artifactual Grb2 dimer by size exclusion chromatography . . . 12
Formation of condensation-competent Grb2 dimers by gentle heat treatment 16
2.5 Novel modes of pLAT condensation by PLCγ1 SHarray . . . 17
2.6 Experimental Methods . . . 21

3 Activity of PLCγ1 from lysate is diminished in LAT:Grb2 condensates 25
3.1 Abstract . . . 25
3.2 Introduction . . . 26
3.3 Results . . . 27
A quantitative activity assay for PLCγ1 direct from cell lysates . . . 27
PLCγ1 activity requires both a kinase and pLAT . . . 29
PLCγ1 localizes strongly to pLAT:Grb2 condensates but displays diminished activity . . . 33
3.4 Discussion . . . 37
3.5 Experimental Methods . . . 40
3.6 Supplementary Figures . . . 47

4 Differential KRas4B diffusion and binding of RBD as a function of PIP2 50
4.1 Abstract 50
4.2 Introduction 51
4.3 Results and Discussion 52
After correcting for anomalies, SPT reveals KRas diffusion slows down as a function of PIP2 52
Tracking of bound RBD reveals differences in binding kinetics depending on diffusive state of Ras 56
4.4 Conclusion 59
4.5 Experimental Methods 59

References 63

List of Figures

2.1 LAT condensation can be induced and visualized in vitro on supported lipid bilayers. . 9
2.2 His10-LAT shows increased stability on the bilayer over His6-LAT. 11
2.3 Purified Grb2 has a metastable dimer dependent on temperature that may be due to misfolding. 14
2.4 Grb2 (without Sos1-PR) only induces phase transition after incubation at low heat. . . 16
2.5 PLCγ1 recruitment to pLAT is mediated by its SHarray. 18
2.6 PLCγ1 SHarray can induce LAT condensation through SH2 and SH3 dependent interactions. 19
3.1 PLCγ1 activity and recruitment can be measured directly from lysate by TIRF imaging of supported lipid bilayers. 28
3.2 PLCγ1-mNG transfected in HEK293T is several times more abundant than endogenous species and can be activated by in vitro phosphorylation. 30
3.3 PLCγ1 requires pLAT and phosphorylation at Y783 to activate on the membrane. . . . 32
3.4 PLCγ1 localizes to the LAT:Grb2:Sos1 condensate, but DAG sensor is not affected at relevant timescales. 34
3.5 PLCγ1 activity is markedly reduced in LAT:Grb2 condensates, regardless of phosphorylation state. 36
3.6 States of PLCγ1 activity in and out of the LAT:Grb2 condensate. 38
3.7 Supplementary Figure 1. Full Western Blot of in vitro PLCγ1 phosphorylation. 47
3.8 Supplementary Figure 2. Lysate assay with PIP2 sensor and pPLCγ1-mNG on a LAT-free bilayer. 48
3.9 Supplementary Figure 3. Validation of the lysate assay with the addition of the LAT:Grb2 condensate. 49
4.1 HRas and KRas diffusion dynamics can be measured using Single Particle Tracking on Supported Lipid Bilayers of varying composition. 52
4.2 Ras diffusion remains single species after correcting for observed erroneous two-species dynamics from motion blur artifacts. 53
4.3 KRas, but not HRas, diffusion becomes slower as a function of PIP2 in the bilayer. . . 55
4.4 RBD can be tracked after binding to GppNP loaded Ras via SNAP647 imaging. 56
4.5 RBD diffusion follows Ras diffusion, while RBD dwell time and recruitment are affected by the diffusive state of Ras. 57
4.6 Ras effectors may be affected by changes in Ras-bilayer interactions related to bilayer composition. 58

Acknowledgments

Firstly, I thank my committee members, Prof. Ke Xu and Prof. Andreas Martin, for their careful review of my dissertation and helpful notes and suggestions. In particular, I thank my chair and advisor Jay T. Groves for his guidance throughout my entire graduate program and for fostering the lab I have called home for half a decade. I know we will continue to have great conversations about the future of science.

I acknowledge and thank my friends and colleagues whose efforts contributed most directly to the work documented here: Young Kwang Lee, Sameer Rajesh, Nugent Lew, and Chun-Wei Lin. I could not have done this without their help and the motivation they gave me. YKL trained me in my first year and completed the Ras experiments with me. Sameer, my student who has now surpassed the master, was present for almost all my work in the last few years, and his incredible work ethic drove me to work harder as well. Nugent was my brother-in-arms ever since he joined the lab, partnering with me on many late-night experiments and purifications. Chun-Wei was constantly challenging my rigid views of our field and contributed heavily to our understanding of Grb2 in the lab. I also thank all my colleagues who throughout the years trained me, held long discussions, went out for drinks, laughed with me, toiled with me, and were truly my found family, including those above and: Mark O'Dair, Jean Chung, Albert (Yuhsien) Lee, Kiera Wilhelm, Laura Nocka, Neil (Hyuneil) Kim, Summer (Simou) Sun, Steven Alvarez, Brittany Stinger, William Huang, Shalini Low-Nam, He Ren, Henry Phan, Shumpei Morita, Sungi Kim, Anand Vissa, Eric Gai, Sarah Hoyle, Saehyun Choi, Darren McAffee, Zhongwen Chen, Jenny Lin, Gabriele Kockelkoren, Eleftheria Kazepidou, and many others. I thank Dimitrios Stamou and Orion Weiner and the entirety of their labs for being great collaborators and guests during our annual Mammoth retreats. And I thank Laurie Mason for being the most fantastic administrative assistant our lab could possibly ask for.

I have many friends and family to thank for my mental well-being throughout graduate school. I am grateful for my mom, who smiled no matter what came her way, and for my dad, who was and still is my geeky inspiration for doing science. I thank my sister, who helped edit my dissertation after I could no longer bring myself to reread it anymore, and my brother for always being there and encouraging me to be who I am. I thank my family in Michigan for fun lakeside getaways. I genuinely would not be who I am today without my group of friends, originally from high school and styling ourselves as 'The Palooza,' who kept me going with many 'Friday Night Throwdowns' and Friendsmases throughout the years. I also thank the friends I have made in the Bay Area that kept me from getting too bogged down in the science. Special shoutouts to Casey Jargo, Amber Warne, Luke Bronx Balancio, Rickie Huang, Minji and Ben (Minbenji), Troy Hughes, Eric Sivonxay, Karen Chiao, and Zeming Wang. Lastly, I want to thank my undergraduate advisor Julio Cárdenas-Rodríguez, who made me believe graduate school was a possibility, and my high school teachers Martin Sade and Robert Hobbins, who both gave me the tools I needed to get started in science. This has been an amazing adventure, and I am so grateful for you all!

Chapter 1

Introduction

The human immune system is a complex patchwork of interconnected cellular and molecular mechanisms. The system consists of both innate immunity, which defends us through pre-defined mechanisms such as the complement system that we are born with, and adaptive immunity, an ever-evolving system of cells that must detect and respond to new threats as well as catalog them for future elimination. At the front line of the adaptive immune system are $CD4^+$ T Cells, commonly referred to as Helper T Cells or white blood cells, that are responsible for the search for and recognition of foreign protein fragments (peptides) called antigens [1]. A class of cells called Antigen Presenting Cells (APCs) assists in this search by processing proteins from the surroundings (often from the debris of dead cells, which may have been infected by a pathogen) and "presenting" corresponding small peptides (p) on the cell surface loaded into Major Histocompatibility Complex Class II (MHCII) membrane structures. $CD4^+$ T Cells probe the surface of APCs using small membrane extrusions, known as microvilli, decorated with the transmembrane T Cell Receptor (TCR) and other costimulatory proteins [2-4]. The TCR binds to pMHCII which, purportedly through a closely controlled but not fully understood proofreading mechanism [5-8], either results in simple unbinding (for self-peptides) or in T Cell activation signals (for true agonists). If a $CD4^+$ T Cell activates fully, it will begin production of extracellular warning molecules (cytokines), to activate the immune system at large, and will start proliferating to amplify this signal [9]. This process is incredibly fine-tuned in both specificity and sensitivity, as it must be since the incorrect recognition of self-peptide could result in catastrophic autoimmune events and inability to detect pathogens would be equally disastrous. In fact, $CD4^+$ T Cells (henceforth, simply "T Cells") must discriminate between self-peptides and antigens that exist simultaneously on APC surfaces, and they can activate on the binding of even a single foreign antigen [10-12]. Where does this almost unbelievable discrimination power come from? And what are the exact molecular events involved in transmitting these vital signals across the T Cell membrane? This is the essence of our research, where we use quantitative biophysical techniques to increase our understanding of the T Cell:APC interface piece by piece.

Thankfully, we are not starting from scratch, as decades of careful biochemical characterization have revealed a number of key players and events in the T Cell activation pathway. Upon TCR binding of an antigen, costimulatory receptors recruit the intracellular Src-family tyrosine kinase Lck, which phosphorylates tyrosines on the Immunoreceptor Tyrosine-based Activation Motifs (ITAMs) on the intracellular tails of the TCR [13-15].

Phosphotyrosines (pY) bind with high affinity and specificity to partner SH2 domains [16-17], with ITAM pYs being recognized by the tandem SH2 domains of the Syk-family kinase Zap70 [18-20]. Initially autoinhibited in the cytosol, Zap70 recruits to phosphorylated ITAMs and is also phosphorylated by Lck, leading to the release of Zap70 autoinhibition through intramolecular binding and reorganization. Active Zap70 then phosphorylates the aptly named Linker for the Activation of T Cells (LAT) [21]. LAT is a 25 kDa, primarily disordered membrane scaffold with four critical tyrosine residues on its membrane-distal end recognized and phosphorylated by Zap70. These LAT-pY residues serve as the basis for what has come to be known, with good reason, as the LAT signaling assembly, which has been substantiated as an integral mediator of T Cell activation [22-26]. Additionally, the LAT signaling assembly has been recognized as a biomolecular condensation, a novel property that is increasingly proving to be relevant to the regulatory function of LAT [12, 25, 27-31].

The LAT signaling assembly is composed of a plethora of cytosolic adapters and signaling enzymes recruited either directly or indirectly to phosphorylated LAT (pLAT). The important pY residues on LAT are known to be pY132, 171, 191, and 226 (numbered according to their position in the sequence of the human "short" LAT isoform) [22-24]. Through just these four phosphotyrosines, LAT is responsible for coordinating a multitude of molecular signaling pathways including the Calcium pathway (which results in cytokine production) and MAPK pathway (which feeds into cell proliferation mechanisms) [26]. In more detail, pY171, 191, and 226 are all recognized by the SH2 domain of the adapter Grb2. The two SH3 domains of Grb2 additionally recruit the Ras activator Sos1, specifically through the binding of the proline-rich (PR) domain of Sos1 (SH3:PR interactions, analogous to SH2:pY, are a common motif in these signaling pathways) [23-25, 27-28]. Multivalent binding of Grb2:Sos1 to pLAT results in extended LAT crosslinking, and under favorable conditions leads to pLAT condensation [27-31]. Subsequently, recruited Sos1 activates Ras, a small membrane GTPase and notorious oncogene due to its central role, which marks the origination of the MAPK pathway [28-29, 33-39]. Furthermore, LAT-pY132 recruits the phospholipase PLCγ1, the primary initiator of the Calcium pathway, via the nSH2 domain of PLCγ1 [9, 24, 26, 40-41]. But the mechanisms by which pLAT condenses are not fully understood, nor is the potential role of pLAT condensation in the activation of PLCγ1. And, further downstream, the role of the membrane in Ras signaling is of interest as well. My work focuses strongly on LAT, PLCγ1, and Ras and their interactions on (and with) the membrane, given their outsized contributions to T Cell signaling.

In order to study these influential signaling facilitators, I focused my efforts on the *in vitro* recapitulation of TCR-proximal signaling pathways. The evident complexity of T Cell signaling is, in some ways, detrimental to its investigation, making it difficult to deconvolve intracellular events. Instead, I examined the components of this system piecewise through reconstitution, while attempting to retain physiological relevance. My contributions were enabled by an elemental tool in our lab, the supported lipid bilayer (SLB) [42]. By forming such synthetic bilayers on microscopy-compatible glass supports, I was able to use fluorescence microscopy to quantitatively study the molecular mechanics of targets *in vitro* in a format directly relatable to TCR-proximal signaling at the membrane [28-29, 43]. These

SLBs were made with defined lipid compositions via vesicle fusion [44-47], and they remained laterally fluid, allowing for the diffusion of both the lipids and lipid-functionalized molecules [42-43, 45, 48-49]. Through linking purified LAT and Ras constructs to the bilayers, I reconstructed, in effect, portions of the inner T Cell membrane machinery. I could then flow solution proteins of interest, either in purified form or in minimally-processed lysate, over these functionalized bilayers with controllable stoichiometry. This allowed careful study of exactly which proteins (or isolated domains) were the primary contributors to mechanistic events, such as pLAT condensation or downstream signaling. Additionally, by utilizing fluorescent fusion proteins and conjugated organic fluorophores linked to my molecules of interest, I observed the spatial organization and temporal dynamics of these proteins on these bilayers simultaneously through Total Internal Reflection Fluorescence (TIRF) microscopy, a surface-selective fluorescence imaging modality [50-53]. With this platform, aided by traditional biochemical techniques, I sought to decipher unknown intricacies in the condensation of LAT and in the signaling of PLCγ1 and Ras.

In Chapter 2, I first introduce the basic preparation of a "pLAT-functionalized SLB," then present my efforts to make these preparations and downstream condensation experiments more reproducible, and lastly demonstrate some unique insights into novel modes of pLAT condensation. Since pLAT-functionalized bilayers form the foundation of many of my experiments (and the experiments of others in the field [27-28, 54-55]), I endeavored to increase consistency in their creation and use by thoughtful redesign of previously utilized LAT constructs. While these types of experiments have been conducted for some time now, there has been an expanding web of LAT constructs for these purposes. I demonstrate some key functional consequences of having disparate LAT constructs, especially in the formation of condensates, and I show the results of the LAT construct I hope becomes a new standard.

With that standard firmly planted, I continue in Chapter 2 with a case study of two recently realized mechanisms of pLAT condensation: through Grb2 dimerization and PLCγ1. While it was first documented almost three decades ago [56], the Grb2 dimer was not considered a relevant contributor to pLAT condensation until a recent investigation from our lab demonstrated its capabilities [57]. That may be due, in part, to misunderstandings surrounding the purification and treatment of Grb2. I detail size exclusion chromatography results that suggested an artifactual Grb2 dimer is formed, perhaps because of misfolding, when Grb2 is expressed in *E*. *Coli* for large batch purification. Then after isolating the correctly folded species, I report a required pre-treatment of Grb2 before it can crosslink phosphotyrosine scaffolds. While not yet fully understood, a gentle heating of Grb2, after initial purification at 4 °C, promoted phase condensation on SLBs, presumably by overcoming an energetic barrier to dimer formation. By documenting these crucial aspects of Grb2 dimerization, I am confident that future Grb2 studies can proceed with greater consistency and less confusion.

In a similar vein to the discovery of pLAT crosslinking through Grb2 dimers, an array of binding domains on PLCγ1 was recently found to possess the ability to condense pLAT [58]. In addition to the aforementioned PLCγ1-nSH2 domain binding to LAT-pY132 [24], PLCγ1

has a cSH2 domain and SH3 domain, in sequence with the nSH2 domain [59]. Collectively, we refer to this as the PLCγ1 "SHarray." The cSH2 domain has canonically been recognized solely as an intramolecularly involved domain, responsible for the autoinhibition and activation of PLCγ1 [59-65]. However, at least *in vitro*, it has demonstrated a penchant for binding to LAT-pY171 [58]. The PLCγ1-SH3 domain is additionally involved in PLCγ1 interactions with LAT, reportedly through binding a site on the PR of the cytosolic scaffold SLP76 which also binds the Grb2-like Gads [24, 41, 66-71]. Gads competes with Grb2 for LAT-pY171 and pY191, and these multivalent interactions ultimately result in the formation of a pLAT:PLCγ1:SLP76:Gads quaternary structure that enhances the binding of all parties [24, 72-74]. Either through this interaction or through the binding of other PR domains, the PLCγ1-SH3 domain facilitates crosslinking of pLAT in cooperation with the nSH2 and cSH2 domains [58, 75]. In the conclusion for Chapter 2, I expound on experiments that both corroborated and broadened our current understanding of pLAT condensation by the SHarray. Chiefly, I show SH3 interactions significantly outweigh the contributions of the cSH2 domain. Finally, I end the chapter with a discussion of potential implications for the physiological signaling pathway.

Building upon the groundwork in Chapter 2, I continue in Chapter 3 to study the full activation pathway of PLCγ1 using SLBs, and I demonstrate the first measurement of PLCγ1 activity in a pLAT condensate. In addition, my methodology allowed me to measure PLCγ1 recruitment to a fluid bilayer as well as its activity simultaneously, again a first for the field. As mentioned previously, PLCγ1 is not simply a structural element, but the initiator of the Calcium pathway in T Cells [40-41, 59-65]. PLCγ1 hydrolyzes PIP2 in the membrane to DAG, which remains in the bilayer and bolsters MAPK signaling, and the cytosolic messenger IP_3, which activates the release of intracellular Calcium stores [9]. In an evolution of previous lysate assay and biosensor development in our lab [29, 39], I was able to measure this enzymatic process using intact PLCγ1-mNG from mammalian cell lysate and a fluorescently labeled DAG binding domain ("DAG sensor") [7-8, 76-78] to measure the hydrolysis of PIP2 in my SLBs. Utilizing PLCγ1-mNG directly from lysate bypassed lengthy and costly purifications and allowed for the rapid generation of mutant PLCγ1 for investigation. The use of the DAG sensor enabled quantitative and immediate measurement of PLCγ1 catalytic activity.

In the most surprising development facilitated by this assay, I found PLCγ1 activity to be observably *decreased* in pLAT:Grb2 condensates. As expected given the structural cooperation of PLCγ1 with pLAT condensation detailed in Chapter 2, PLCγ1 from lysate was heavily incorporated into pLAT condensates, and there was evidence this increased PLCγ1 density at the bilayer. Prior research suggested PLCγ1 activity is enhanced by its inclusion in condensates [79], but that was based on a growth-receptor protein complex. I showed pLAT:Grb2 condensates have the opposite effect, but after incorporating full-length SLP76 and Gads (also from lysate), the canonical adapters of PLCγ1 in T Cells, the activity of PLCγ1 was partially rescued. This suggests a novel form of compositional regulation of PLCγ1. SLP76 and Gads, for instance, are expressed only in T Cells, while PLCγ1 is ubiquitously expressed and plays a role in growth-receptor pathways [59-65, 79]. My findings, and

continued experiments with this now-validated assay platform, could prove to be instrumental in deciphering differential activation of PLCγ1 in divergent signaling pathways.

Lastly, in Chapter 4, we advance downstream of LAT and PLCγ1 and examine dynamics related to active Ras on the membrane. Rather than measuring the activation of Ras, we focus on the effects of the membrane itself on two SLB-tethered Ras isoforms. Ras exists as many isoforms in cells, with a critical difference being in the Hyper-Variable Regions (HVRs) that link their lipidated C-terminus to their globular GTPase G-domain [49, 80-81]. In particular, we investigated HRas, an isoform with a neutral HVR, and KRas-4B (or simply "KRas"), which has a unique polylysine region in its HVR [49]. There is evidence that both the G-domain and HVR of KRas interact with anionic lipids, notably PIP2 [82-86]. I was able to corroborate this evidence using Single Particle Tracking (SPT) to measure Ras diffusion on SLBs with varied PIP2 content. KRas, but not HRas, diffusion decreased in line with the increase in PIP2, suggesting a specific interaction of KRas with the anionic headgroup. Furthermore, by tracking a labeled Ras Binding Domain (RBD) of a downstream Ras effector, we determined the diffusive state of Ras has potential functional consequences for its signaling. This work represents a simple but effective strategy for the measurement of meaningful Ras dynamics at the membrane.

In all, my work herein is a collection of foundational methodology and experimental observations that advance our knowledge of vital building blocks of early T Cell signaling. I validated the use of supported membranes and fluorescence imaging for the purpose of studying both membrane protein organization and enzyme catalysis, made meaningful progress in increasing the reproducibility of these experiments, and contributed to the understanding of PLCγ1 and Ras signaling. These efforts enable clear next steps, such as the study of how PLCγ1 diverges in different signaling pathways.

Chapter 2

Novel modes and increased reproducibility of *in vitro* LAT condensation

Copyright Notice

Data in Figure 2.4 were adapted with permission from "A two-component protein condensate of the EGFR cytoplasmic tail and Grb2 regulates Ras activation by SOS at the membrane" Chun-Wei Lin, Laura M. Nocka, Brittany L. Stinger, Joseph B. DeGrandchamp, L. J. Nugent Lew, Steven Alvarez, Henry T. Phan, Yasushi Kondo, John Kuriyan, and Jay T. Groves. *Proceedings of the National Academy of Sciences* **119**, e2122531119 (2022). Copyright 2022 National Academy of Science.

2.1 Abstract

Biomolecular condensates of membrane proteins have risen as a potential regulatory mechanism for cell signaling, and T Cells have recently been demonstrated to rely on the condensation of the membrane scaffold LAT for signal integration. The LAT condensation constitutes a signaling hub of adapter proteins, such as Grb2, and T Cell activating enzymes, such as the Ras-activator Sos1 and Calcium-gatekeeper PLCγ1. Due to this central role, increased understanding of LAT condensation mechanisms and its consequences are of great interest, and insights are continuously coming to light about novel modes of condensation and downstream interactions. To facilitate these investigations, *in vitro* reconstitution of the LAT condensation is of critical importance, as it allows for more exact determination of molecular events versus attempting to deconvolve complex and crowded intracellular pathways. Herein, I detail a platform we have developed over many years for observing LAT condensation and subsequential signaling events on supported bilayers, and I present new contributions that allow for more consistent reproducibility in these experiments. Then, I summarize recent discoveries utilizing this platform including condensation of LAT via Grb2 dimers and via the SH array of PLCγ1. I particularly expound on the complicating details of these developments in the hope of empowering future exploration of this vital system.

2.2 Introduction

In groundbreaking recent developments, our lab and others have identified the LAT signaling assembly as a fully-fledged phase-transitioned framework [27-30], part of an emerging class of signaling-competent biomolecular condensates [87-90], rather than a simple cluster. Besides being a physically interesting phenomenon, these condensates have demonstrated unique and far-reaching functional consequences. In particular, the condensation of pLAT via Grb2 interactions has a considerable enhancing effect on Sos1 activation by increasing the time it interacts with the membrane, giving a boost to the membrane-dependent restructuring of its autoinhibitory domains [28-29]. In addition, the nature of condensation as an all-or-nothing occurrence makes it an attractive suspect as a digital converter of analog signals, which would be incredibly useful to a T Cell requiring both high specificity and sensitivity. Our lab has, in fact, recently revealed such a role for LAT condensates in T Cell signaling, demonstrating their apparent contribution to the integration of TCR binding events and role in antigen discrimination [12, 31]. The mechanism by which the LAT condensate achieves this is not well understood, however, and so the study of proximal signaling events, and of the condensate itself, is a fundamental imperative.

Perhaps because its importance is being realized, what we know about how the pLAT condensation occurs in cells seems to be evolving at increasing speeds. It has been established for some time now that Grb2 and Sos1 can crosslink pLAT through pY:SH2 and SH3:PR interactions working in tandem [25]. This was long thought to be the major driving force behind pLAT condensation, though it was an open question how Sos1 could contribute meaningfully given its low copy number [91]. But it has come to light that Grb2 dimers can phase transition pLAT (and other similar pY scaffolds) without the need for Sos1 [57]. Grb2 alone stands to be a large contributor to pLAT condensation then, due to its high expression and relative abundance. The Grb2 dimer itself is also regulated by a tyrosine residue, that will break the dimer when phosphorylated [57, 92]. This represents a novel dimension for the control of pLAT condensation, with the phosphorylation of Grb2 potentially placing a self-limiting constraint on the size or lifetime of pLAT condensates which are otherwise only encouraged by increased kinase activity.

In a similar vein of novel discovery, PLCγ1, in addition to its enzymatic role, has been suggested as a potential nucleator of pLAT condensates. It has been demonstrated that the slow phosphorylation of LAT-Y132 is complimentary to proofreading by the TCR [93], and our lab has shown how a mutation that slows this step even further has a negative downstream effect on the time it takes to form pLAT condensates [31]. Preliminary results go further and demonstrate the overexpression of PLCγ1 results in faster condensate formation, and this effect is dependent on an array of SH domains of PLCγ1 [75]. This has been corroborated by a study exhibiting the ability of this isolated array to condense pLAT *in vitro* in a cooperative manner with Grb2:Sos1 [58].

For the study of these novel modes of LAT condensation as well as downstream events, I

present herein foundational experimental methodology for using *in vitro* LAT-functionalized supported bilayers. I first demonstrate the basic preparation of pLAT bilayer that is primed for condensation experiments and cover efforts to design a better LAT construct for increased reproducibility. Similarly, I detail easy-to-miss but critical steps in the purification of dimeric Grb2. Lastly, I recount experiments with PLCγ1 truncations that both corroborate and expound on recent findings.

2.3 Standardizing *in vitro* LAT condensation experiments

The basics of LAT condensation on supported bilayers

Our lab and others have been performing membrane-protein phase condensate experiments on supported lipid bilayers (SLBs) for the better part of the last decade [27-28, 88]. In our lab, we form these SLBs in simple 6-channel lateral flow cells (ibidi μ-Slide chambers) with glass bottoms that serve as bilayer supports and are compatible with fluorescence microscopy methods. This gives us an easy platform for adding components to the SLB and performing washes using just our standard pipets or a laboratory vacuum line. The typical strategy is to functionalize the SLB with the membrane scaffold of interest using the chelation of histag tails to Ni-NTA lipids in the bilayer [48]. Our lab utilizes a histagged LAT construct consisting of the LAT intracellular domain with the four membrane-distal tyrosines intact (Fig 2.1A). These tyrosines (Y132, Y171, Y191, and Y226 in the human LAT sequence), once phosphorylated, serve as critical binding sites for cytosolic adapters. We purify LAT in an unphosphorylated form So, in order to generate pLAT and allow for adapter binding, we take advantage of an easily purified promiscuous Src-family kinase, Hck [28, 94-95]. We express Hck with an N-terminal histag as well, linking both LAT and Hck to the bilayer (Fig 2.1B). With the addition of ATP to the flow channel, Hck phosphorylates LAT (pLAT) and, furthermore, keeps it phosphorylated during experiments, protecting pLAT from spontaneous dephosphorylation and the activity of wayward phosphatases. This forms the basis of a "pLAT functionalized" bilayer to which we add a variety of crosslinkers and analytes for study.

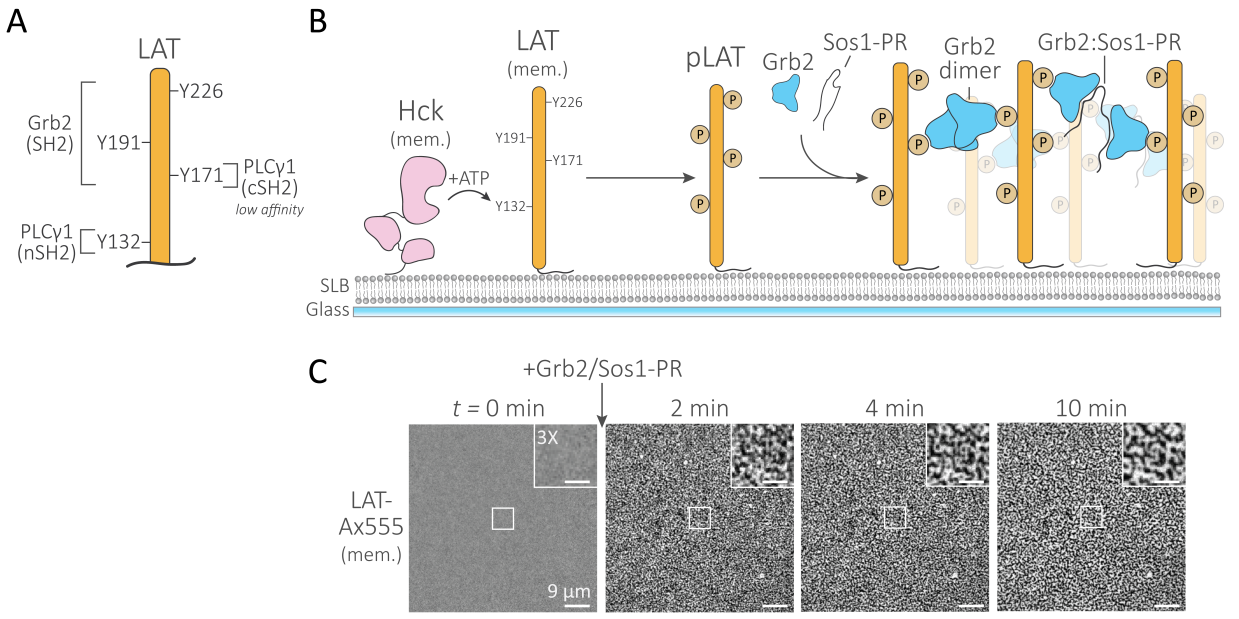


Figure 2.1: LAT condensation can be induced and visualized *in vitro* on supported lipid bilayers.

A. A schematic of LAT detailing its major tyrosine binding sites and binding partners. **B.** A schematic depicting a typical *in vitro* LAT condensation experiment. LAT and Hck are functionalized to an SLB by histidine-Ni chelation. Hck phosphorylates LAT, and adapters such as Grb2 and Sos1-PR can be flowed in to condense LAT. Grb2 can crosslink LAT both on its own (as a dimer) and through SH3-PR interactions. **C.** Field-corrected TIRF images of fluorescent LAT-Ax555 (at a density of ~1500 μm^{-2}, lipid composition (mol%): 96:4 DOPC:Ni-DGS). before and after injection of 6 μM Grb2 and 2 μM Sos1-PR. The large FOV is 60 μm x 60 μm with an inset showing a 3X magnification of the central 10 μm x 10 μm region. The scale bar is 9 μm for the lower magnification and 3 μm for the inset.

With the bilayer established, we turn to the classical crosslinkers of cellular LAT—Grb2 and Sos1 (in this case the PR domain) [25, 28]. Fluorescently labeled pLAT is initially a single, fast-moving and homogenous species, appearing as an indistinct white/grey across the entire Field of View (FOV) in TIRF images (Fig 2.1C). With the addition of Grb2 and Sos1-PR (commonly at a molar ratio of 1:3), pLAT condenses into dense "protein islands" with disperse LAT and free membrane in between. TIRF images of the phenomenon become beautiful collages of bright and dark phases (Fig 2.1C). LAT slows down considerably, leading it to appear brighter and more spatially defined due to a decrease in motion blur (photons being spread across multiple pixels during the exposure time of the camera because of molecular movement). Importantly, LAT is not immobilized in these condensates. LAT can interchange (slowly) between these domains, as determined by fluorescence recovery experiments [28]. Adapters can also exchange freely, though their kinetics are affected by increased avidity [28-29]. This platform provides both a materially interesting and functionally important condensate for study in an accessible format. However, we have noticed inconsistencies across different iterations of these LAT condensation experiments.

A new LAT construct for more consistent experiments

Due in part to the nature of academic research (a wide range of researchers have made their mark in this field over many years), the protein constructs used for forming *in vitro* LAT condensates have varied, even within our lab. We have utilized His6-LAT (purified in-house or by UC Berkeley collaborators) [28] as well as His8-LAT (purified by collaborators at UT Southwest) [96]. The number of histidines will affect both the strength of LAT chelation to the bilayer and its diffusion [48]. We have also utilized LAT labeled via maleimide-conjugated fluorophores to C117 [28-29] as well as C27 (close to the membrane) [30]. The labeling site could affect how LAT monomers interact with each other or with the membrane [97-98], and a number of these constructs contain a, now archaic, cleavage site (recognized by TEV protease) between the histag and LAT. This site enables LAT cleavage and release from the membrane by any TEV contamination present in other analyte/crosslinker purifications, and given the prevalence of TEV in purifications, this is a concerning feature. Some of these differences might explain why the timescale of condensation can vary quite dramatically, from as short as seconds (Fig 2.1C and [57]) to as long as 30-40 minutes before large domains form [28], even for similar densities of LAT. In an endeavor to mitigate these inconsistencies and establish a standard, we cloned and purified a new construct of LAT.

The construct most recently used in published results from our lab, His6-LAT1C(27-233) (Fig 2.2A), has a 6X-histidine tag and the mutation C117S in order to leave C27 as the only possible labeling site for maleimide-conjugation [30]. It also has a random linker (7 amino acids, including a tyrosine), a TEV cleavage site (7 amino acids), and six membrane-proximal tyrosines that are not known to be phosphorylated *in vivo* [21-24]. For our new construct, His10-LAT5Y(30-233) (Fig 2.2B), we instead built in a 10X-histidine tail and replaced the linker/TEV sequence with a well-studied unstructured linker (10 amino acids in length) [99]. We hoped to decrease the chance of LAT desorption from the bilayer and remove any interference from the linker. Amino acids 27-29 were removed so the only possible labeling site was C117, distant from the membrane. We determined this labeling site was less likely to affect results, especially at low labeled fractions, and this is the site most commonly used by other researchers as well [27, 54]. Y36, 45, 64, 70, and 110 were also mutated to F to reduce any potential artifacts from non-physiological phosphotyrosines (that might be phosphorylated by the strong kinase, Hck). We retained Y132, 171, 191, and 226 due to their established importance *in vivo* [21-24]. And even though its function is not known, Y127 was left unchanged, as it is phosphorylated after T Cell activation and is a highly conserved residue [21, 93, 100]. Next, we sought to show His10-LAT5Y was meaningfully more consistent while maintaining the ability to form a condensate.

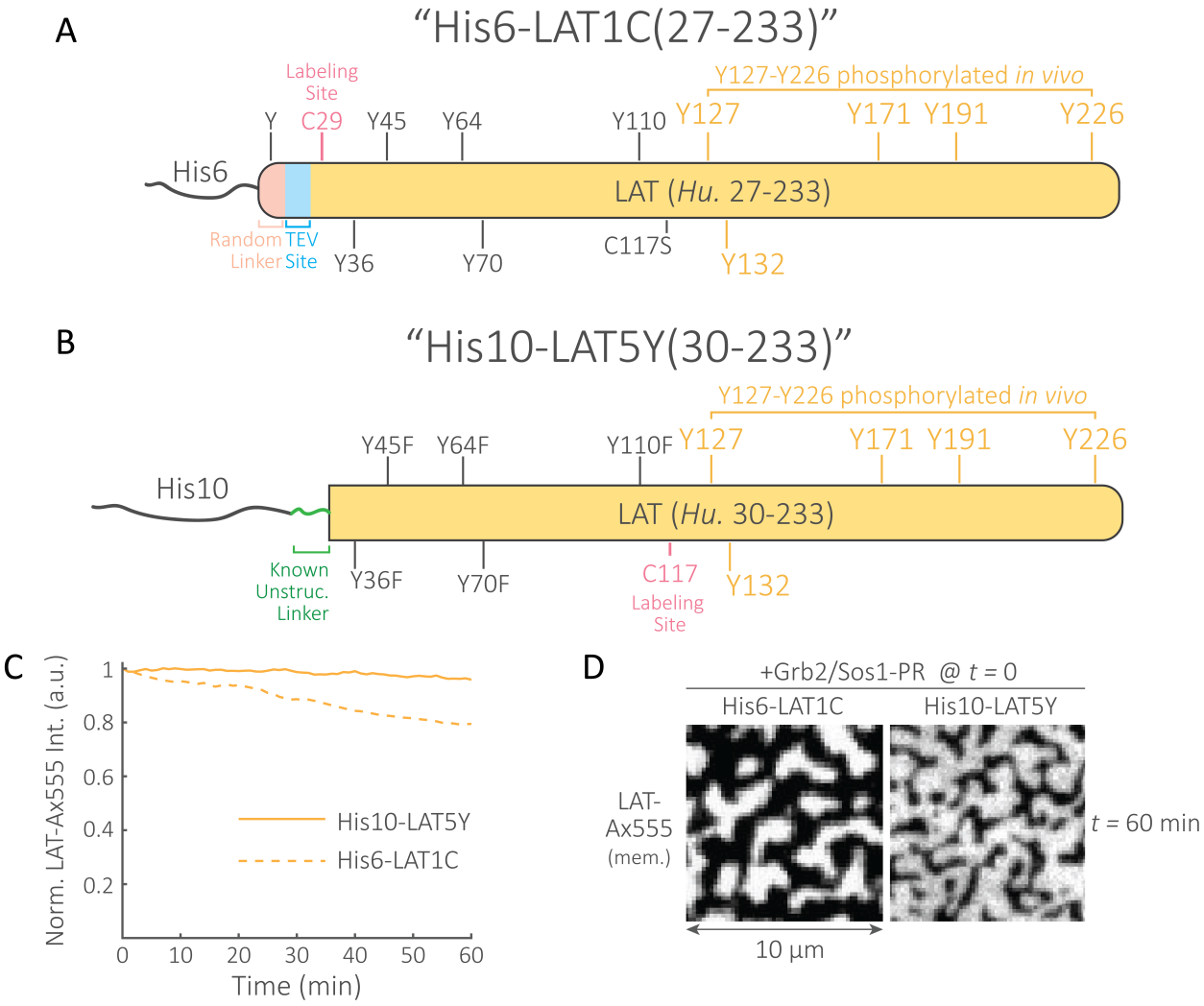


Figure 2.2: His10-LAT shows increased stability on the bilayer over His6-LAT.
A-B. Schematics of LAT constructs used for *in vitro* experiments. Residues are labeled according to their position in the native LAT sequence. His6-LAT1C(27-233) (**A**) has a 6X-histidine (grey tail) and the mutation C117S. It also has a random linker (light pink, 7 amino acids), a TEV cleavage site (light blue, 7 amino acids), and six membrane-proximal tyrosines that are not known to be phosphorylated *in vivo [21-24]*. His10-LAT5Y(30-233) (**B**) has a 10X-histidine (grey tail) and the linker/TEV sequence was replaced with a well-studied unstructured linker (green, 10 amino acids). Y36,45,64,70,110 were mutated to F. The only possible labeling site is C117. Both constructs (**A-B**) were created using human sequences and have Y127,132,171,191,226 due to their importance *in vivo* (gold). **C.** Normalized fluorescence traces over 60 min for His10-LAT5Y (solid gold) and His6-LAT1C (dashed gold) functionalized to SLBs, showing desorption from the bilayer over time. Lipid composition (mol%): 96:4 DOPC:Ni-DGS. Initial LAT densities: ~1500 μm^{-2}. **D.** TIRF images (10 µm x 10 µm) of Alexa555-labeled His6-LAT1C (left) and His10-LAT5Y (right) after a 60 min incubation with Grb2:Sos1-PR (6 µM:2 µM). Lipid compositions and densities are equivalent to those in (**C**).

One foreseeable effect of the level of LAT chelation to the bilayer is differences in the rate of desorption, and thus changes in densities over time. If desorption is considerable, bilayers that are sometimes left for 1-2 hours after LAT chelation while other channels are imaged may have quite different LAT densities. One could control this by investing in careful timing of experiments such that the time allowed for desorption is kept constant, but this is often an untenable concept for complex, day-long experiments. To see if a larger histag might decrease desorption and allow for greater consistency, we took TIRF time-lapses of bilayers functionalized with Alexa 555 labeled His6-LAT1C and His10-LAT5Y (Fig 2.2C). Our standard strategy is to incubate LAT (20-45 min) and wash the channel to remove excess LAT. We then wait at least 20 minutes for weakly chelated proteins to desorb (during this time, we sometimes simultaneously phosphorylate LAT with the addition of ATP) before giving the bilayer a final wash [48]. We started our time-lapses after the final wash and tracked the normalized average image fluorescence over 60 minutes, where decreasing signal correlates to desorption (Fig 2.2C). In agreement with previous results from our lab on His10 desorption kinetics [48], His10-LAT5Y signal is stable over 60 minutes, dropping <5%. Meanwhile, His6-LAT1C signal drops close to 20%, indicating a clear disadvantage compared to His10-LAT5Y. Furthermore, His10-LAT5Y retains the capability to condense strongly with the addition of crosslinkers (Fig 2.2D) and appears to have larger condensed domains than His6-LAT1C despite similar starting densities. One concern might be the change in diffusion for the different constructs. However, fluorescence recovery after photobleaching (FRAP) for the two constructs was similar, and diffusion coefficients measured by fluorescence correlation spectroscopy were only moderately slower for His10-LAT5Y ($D_{\text{His6-LAT1C}} = \sim 1\ \mu m^2 s^{-1}$, $D_{\text{His10-LAT5Y}} = \sim 0.8\ \mu m^2 s^{-1}$, results not shown) [28]. It still may be of interest to determine whether His8 is a better middle ground between decreasing desorption and lowering diffusion, as His8-LAT has also been used widely in the field [27, 54].

In all, we hope His10-LAT5Y becomes a unified standard that enables more reproducibility and higher precision experiments. The additional His-linkage successfully reduced LAT desorption and will allow for more consistent LAT densities (Fig 2.2C). Furthermore, His10-LAT5Y maintains the ability to form phase-transitioned condensates (Fig 2.2D) and should act as a more stable backbone for experiments involving condensation.

2.4 Intricacies in the Grb2 dimer mediated condensation of LAT

As mentioned above, we have been using Grb2 and Sos1-PR to condense LAT for many years [28-30], but it was not until the last few years that we determined Grb2 self-dimerization contributes significantly to the crosslinking of LAT (rather than crosslinking through only Grb2-SH3:Sos1-PR interactions) [57]. Certainly, this is in part due to the fact that Grb2 dimerization itself is not fully understood. There is an incredible amount of disagreement

and contradiction in the field. For example, some researchers suggest Grb2 dimerization abrogates the binding of Grb2 to PR domains [92], while others claim dimerization enhances that same interaction [101]. There is even an unclear picture of what constitutes the "Grb2 dimer" in the first place and inconsistencies in its purification.

Separating a metastable, artifactual Grb2 dimer by size exclusion chromatography

To begin with, Grb2 is an adapter protein that can be broken down into three main domains: an SH2 phosphotyrosine-binding domain sandwiched between an N-terminal SH3 PR-binding domain (nSH3) and C-terminal SH3 domain (cSH3) (Fig 2.3A). Grb2 has been viewed as a potential dimer for decades, as the first full-length crystal structure of Grb2 was solved as an asymmetric dimer [56]. In this dimer, the SH2 domain nestles against the cSH3 domain of the partner Grb2 (Fig 2.3B), and all domains are thought to maintain their ability to bind their partner peptides [92]. This is the dimer researchers most often reference in their studies, and there is good evidence showing it exists in a classic monomer:dimer equilibrium with concentration dependence and has physiological relevance [92, 102]. Alternatively, there exists what has been referred to as a "domain-swap dimer" of Grb2 [103-106]. Structures for this type of Grb2 dimerization have only been fully solved for the truncated SH2 domain, though there is a theoretical model for a postulated full-length domain-swap (Fig 2.3C) [103]. In the structures for truncated SH2, an alpha helix appears to be traded between the SH2 monomers, yet they are still able to bind pY peptides [106]. This configuration has been shown to be metastable, without a concentration dependence, but the interaction can be broken by increasing temperature (40-50 °C) or by physical perturbation [106]. The theorized full-length domain swap dimer is modeled as what could be referred to as a "twist-tie" structure (Fig 2.3C). While the full-length version of the domain-swap dimer has not been experimentally characterized, it is interesting to consider its existence, and there is sufficient reason to believe it is present in full-length Grb2 purifications. While some have tried to claim a functional importance for the domain-swap dimer [106], it is widely viewed simply as an artifact of purification done in *E. Coli*, perhaps brought about by misfolding from the lack of human cofactors. Regardless, it should be of the utmost importance for researchers to separate these two dimer configurations in their studies, especially if they are thermodynamically distinct.

In that vein, we noted some peculiarities among different batches of Grb2 purification in our lab (Fig 2.3E-F). When all is said and done, the purification of Grb2 in *E. Coli* seems to be an uncomplicated affair (especially in comparison to Sos1-PR, a notorious troublemaker). It is easy to separate from contaminants and is stable against proteolysis and aggregation. However, results from experiments done with Grb2 purified at different times or by different people could be quite different. In some cases, Grb2 alone could condense LAT, and at other times the same concentrations and conditions could not. In an attempt to characterize these anomalies, we performed sequential size exclusion chromatography (SEC) experiments on

different batches of purified Grb2 and from different isolated SEC peaks. Then, we subjected the isolated peaks to heat treatment and observed their changes in SEC results.



Figure 2.3: Purified Grb2 has a metastable dimer dependent on temperature that may be due to misfolding.

A-C. Graphics depicting possible states of Grb2. Grb2 has N-terminal SH3 (nSH3), SH2, and C-terminal SH3 (cSH3) domains (**A**). Grb2 has been structurally examined via X-Ray crystallography (PDB: 1GRI) where it appears as a dimer (**B**). This dimer is proposed as dynamic and concentration-dependent. Full-length Grb2 has been modeled in a "domain-swap" configuration (**C**). The domain-swap dimer appears to be metastable, with concentration having no effect on the monomer:dimer ratio. **D.** SEC chromatograms of repeat injections of Grb2 from different purifications (Batch 1 – blue, or Batch 2 – orange and gold) and/or isolated peaks (Batch 2 monomer – orange dashed, or Batch 2 dimer – gold dotted) from previous SEC runs. SEC was done at 4 °C on a Superdex 75 Increase column (24 mL bed

volume) with signal tracked via UV absorbance at 280. Maximums of each chromatogram were aligned to the maximum of Batch 1. **E.** The ratio of monomer:dimer (peak maximum / peak maximum) for the SEC chromatograms in (**D**). Concentrations of each batch (determined via A280 before injection on the column) are overlayed on the corresponding bar in white text. **F**. The ratio of monomer:dimer (peak maximum / peak maximum) for SEC runs (not shown) of Batch 2 under different conditions. For heating treatments, aliquots were heated in a thermocycler for the time indicated.

In our Grb2 purifications, Grb2 is heavily expressed and often oversaturates even our largest SEC columns. It generally appears as a large, broad primary peak that elutes at volumes equivalent to roughly 50% of the column volume (CV) and is characteristic of monomeric Grb2, with a smaller but not insignificant shoulder (unresolved) corresponding to dimeric Grb2. It is not always clear among distinct purifications what fractions are pooled and labeled "purified Grb2." There may be more or less of the dimer shoulder pooled together with the monomer peak. That is evident after performing SEC on two different batches of Grb2 (Fig 2.3D-E). These batches were both purified by the same person (on different occasions), yet display quite significantly different monomer:dimer ratios. In Batch 2, additional care was taken to isolate the monomer peak and dimer shoulder, and the dimer was pooled and collected (separately) for analysis. It should be noted both the monomer fraction and dimer fraction appear as a single, clean band at the molecular weight of Grb2 in SDS-PAGE results (not shown). In contrast to research claiming otherwise [92, 102], these peaks did not reequilibrate and seemed to largely maintain their monomer:dimer ratio irrespective of concentration (Fig 2.3E). Even at 1/5 of the concentration of the Batch 2 monomer peak, the Batch 2 dimer fraction had a much smaller monomer:dimer ratio, which was the exact opposite of what would be expected of a concentration-dependent equilibrium. Furthermore, any treatment of Batch 2 (either monomer or dimer pools) at room temperature or higher resulted in a shift towards the monomer (Fig 2.3F).

Notably, the SEC step was carried out at 4 °C (all steps in our purifications are carried out at 4 °C, as a standard operating practice), and after heat treatment, the samples were centrifuged at 4 °C to remove any aggregates. This did not nominally change the concentrations measured by absorbance at 280, but there was observable cloudiness of Grb2 solutions under certain conditions. It is possible some configurations of Grb2 are less soluble at 4 °C, which might explain why other studies observed (via SEC at 25 °C) the dimeric form of Grb2 as the preferred form (while we saw the opposite) [92]. Perhaps, the dimeric peak observed at 4 °C is then, in actuality, the domain-swap dimer (Fig 2.3C), which would explain its metastability (Fig 2.3E). This implies the best course of action would be to carefully separate this peak in our 4 °C purifications and only pool fractions from the monomeric peak. By doing so, do we see more consistent results in condensation experiments using Grb2 as a crosslinker?

Formation of condensation-competent Grb2 dimers by gentle heat treatment

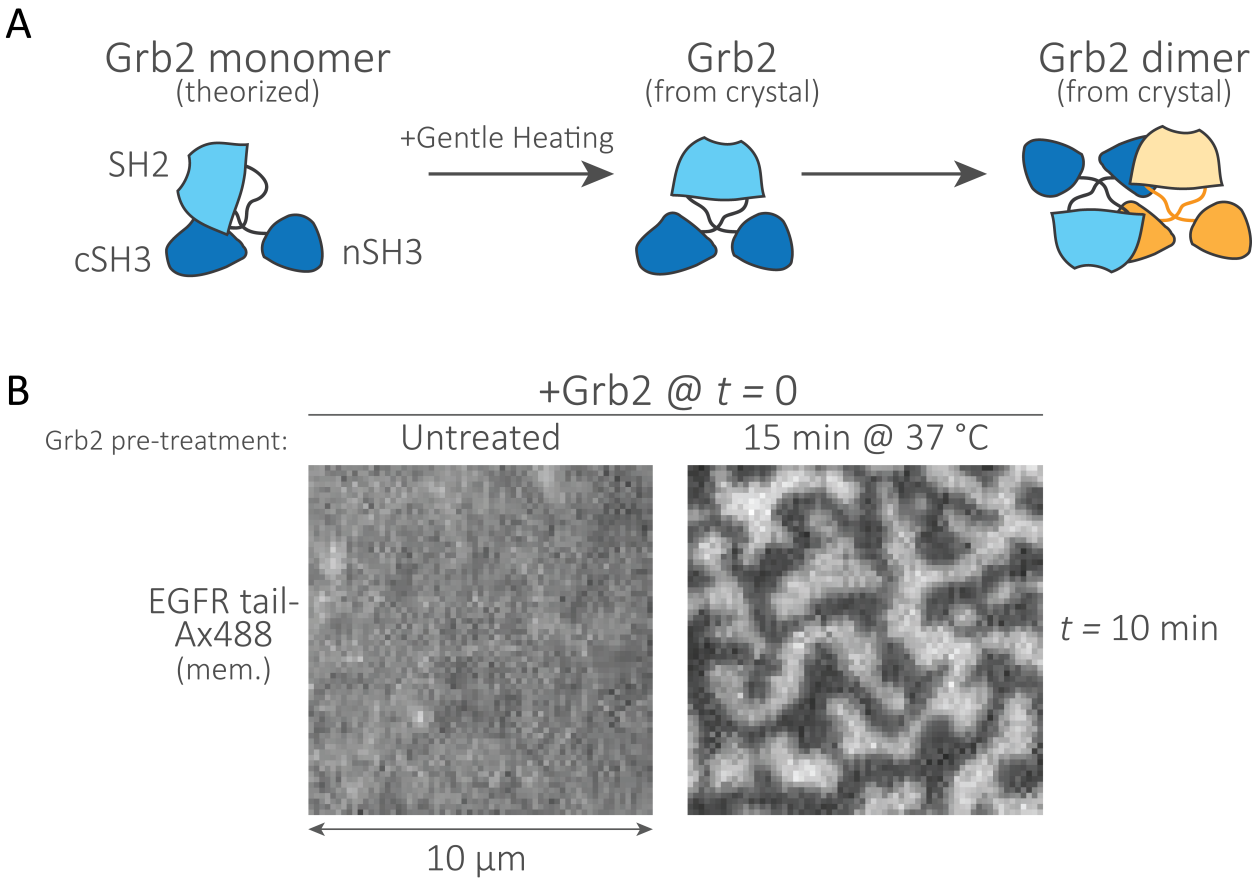


Figure 2.4: Grb2 (without Sos1-PR) only induces phase transition after incubation at low heat. **A.** A graphic depicting a model where Grb2 exists as a structurally unique monomer (left) which undergoes rearrangement at physiological temperatures (middle) allowing for dimer interactions (right). **B.** TIRF images (10 µm x 10 µm) of Alexa488-labeled EGFR tail after 10 min incubation with untreated Grb2 (left) or Grb2 that was gently heated for 15 min at 37 °C in a thermocycler (right). Imaging was done at room temperature. EGFR tail is an unstructured phosphotyrosine scaffold similar to LAT [57]. EGFR density: ~1500 μm^{-2}. Grb2 concentration: 6 µM. Lipid composition (mol%): 92:4:2:2 DOPC:Ni-DGS:PIP2:MCC-DOPE.

In fact, careful treatment of Grb2 in this way results in reliably seeing *little to no* condensation at typical timescales, as evidenced by experiments with phosphorylated EGFR tail (a phosphotyrosine scaffold analogous to pLAT) (Fig 2.4B, left image) [57]. We were confident in the removal of any potential domain-swap artifacts, so at first glance, it may appear the domain-swap dimer was the primary crosslinker in previous experiments showing Grb2-mediated condensation. However, after much trial and error, we observed

how a gentle heat treatment (at a physiologically relevant temperature, 37 °C) of Grb2 before its addition to pEGFR tail resulted in very dependable condensation on the bilayer (Fig 2.4B, right image). This treatment should have the effect of destabilizing any domain-swap formation (Fig 2.3F), so it is unlikely to be due to domain-swap dimer formed after the fact. Notably, this condensation can be dissolved by the phosphorylation of Grb2, which is characteristic of the asymmetric dimer [56, 92]. How does one make sense of this?

It has been proposed that Grb2 cannot simply exist in the monomeric form seen in the dimeric structure [102]. It is more likely that, in the absence of a cSH3 from a separate Grb2 unit, the SH2 domain would fold over and form an interface with its own corresponding cSH3 (Fig 2.4A). The strength of this interaction has not been characterized, but we can hypothesize that increased temperatures will affect this structure and allow Grb2 to sample more configurations, including dimer formation. If this form is less soluble at low temperatures, it explains why we see very little dimeric population in our purifications where expression is typically carried out at 18 °C and purification at 4 °C (and insoluble components of cell lysate are pelleted by high-speed centrifugation). Interestingly, Grb2 that has been heated at 37 °C retains the ability to condense pLAT/pEGFR tail even after flash-freezing and storage at -80 °C (and successive thawing), suggesting some stability of the dimer against temperature changes.

Our working theory is then: domain-swap dimers of Grb2 are likely to exist in purifications due to artificial expression in *E*. *Coli* but can be successfully separated (Fig 2.3), and subsequent heat treatment of the isolated monomer encourages formation of the "true" asymmetric Grb2 dimer (Fig 2.4). This relatively complex scheme explains the considerable differences between results among not just our lab but also others in the field. The material properties of the domain-swap dimer in comparison to the asymmetric dimer might be of additional interest, but it is of questionable importance for the purposes of our studies of pLAT condensation. If Grb2 purification and treatment are done accordingly, we can be confident we are observing crosslinking induced by the physiologically relevant dimerization of Grb2.

2.5 Novel modes of pLAT condensation by PLCγ1 SHarray

In the previous sections, we utilized purified Grb2 as the primary condensing agent of pLAT, through either Grb2:Sos1 interactions or Grb2:Grb2 dimers, but the pLAT condensate contains many more protein components in vivo, including the T Cell activation mediator PLCγ1 [24]. PLCγ1 is the primary gatekeeper for the Calcium pathway in T Cells, which controls downstream cytokine production and is used as a marker for T Cell activation [26]. PLCγ1 is recruited to pLAT, most importantly through the binding of PLCγ1-nSH2 to pY132—a pY site on LAT expressly reserved for PLCγ1 (Fig 2.5A). PLCγ1 also has a cSH2 domain and SH3 domain in sequence with the nSH2 domain, and the three domains

collectively form what we call the "SHarray" (Fig 3.5B) [75].

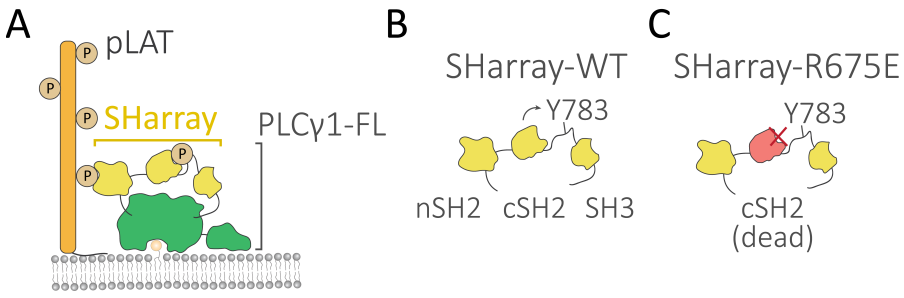


Figure 2.5: PLCγ1 recruitment to pLAT is mediated by its SHarray.
A-C. Graphic depictions of PLCγ1 binding to pLAT through its nSH2 domain (**A**) and the domain structure of the SHarray-WT (**B**) and SHarray-R675E (**C**) truncation constructs. R675 is a critical residue for the binding of pY-peptides by cSH2, and the R675E mutation abolishes cSH2 binding to pLAT or intramolecularly to pY783.

Every domain of the SHarray is critical to PLCγ1, either through recruitment or activation. As stated, PLCγ1-nSH2 is the major mediator of its recruitment to pLAT. PLCγ1-cSH2, on the other hand, is canonically involved in the release of PLCγ1 autoinhibition by binding intramolecularly to PLCγ1-Y783 upon phosphorylation and inducing a whole-protein structural rearrangement [59-65], though it has also been observed recently to bind with considerable affinity to LAT-pY171 [58]. PLCγ1-SH3, like the Grb2 SH3 domain, binds PR domains, with its demonstrated *in vivo* binding partner being SLP76 [24]. SLP76 then, additionally, binds multivalently to the Grb2-like Gads, which recognizes pY171 and pY191 on LAT, resulting in a quaternary pLAT:Gads:SLP76:PLCγ1 complex [71-74]. These multivalent interactions of the PLCγ1-SHarray with pLAT suggest there could be pLAT crosslinking mediated by PLCγ1, and thus an effect on pLAT condensation. Indeed, newly published and preliminary live T Cell results from our lab indicate PLCγ1 has a role in the nucleation of *in vivo* LAT condensates [31, 75]. When mutations are introduced into LAT that slow the phosphorylation of LAT-Y132, the amount of time required to form a LAT condensate downstream of a TCR-antigen binding event is significantly increased. This is evidence that PLCγ1, the only protein with meaningful affinity for LAT-pY132 [24], must be involved either in crosslinking LAT or otherwise in protecting pLAT from dephosphorylation. In support of the former hypothesis, novel results from Zeng et al. [58] convincingly established, via *in vitro* imaging experiments on SLBs analogous to ours, that the SHarray can crosslink pLAT via both SH2 interactions and SH3-PR interactions. We sought to confirm their observations and to examine the contribution of the cSH2 domain more closely in the crosslinking of pLAT. Thus, we purified a construct of the SHarray-WT (Fig 2.5B) as well as a mutant "cSH2-dead" construct, SHarray-R675E (Fig 2.5C), with a mutation to the critical arginine of the cSH2 domain that abolishes binding to pY-peptides. We utilized these truncations and Sos1-PR (an accessible stand-in for SLP76/Gads) in pLAT condensation experiments on SLBs to characterize their crosslinking properties.

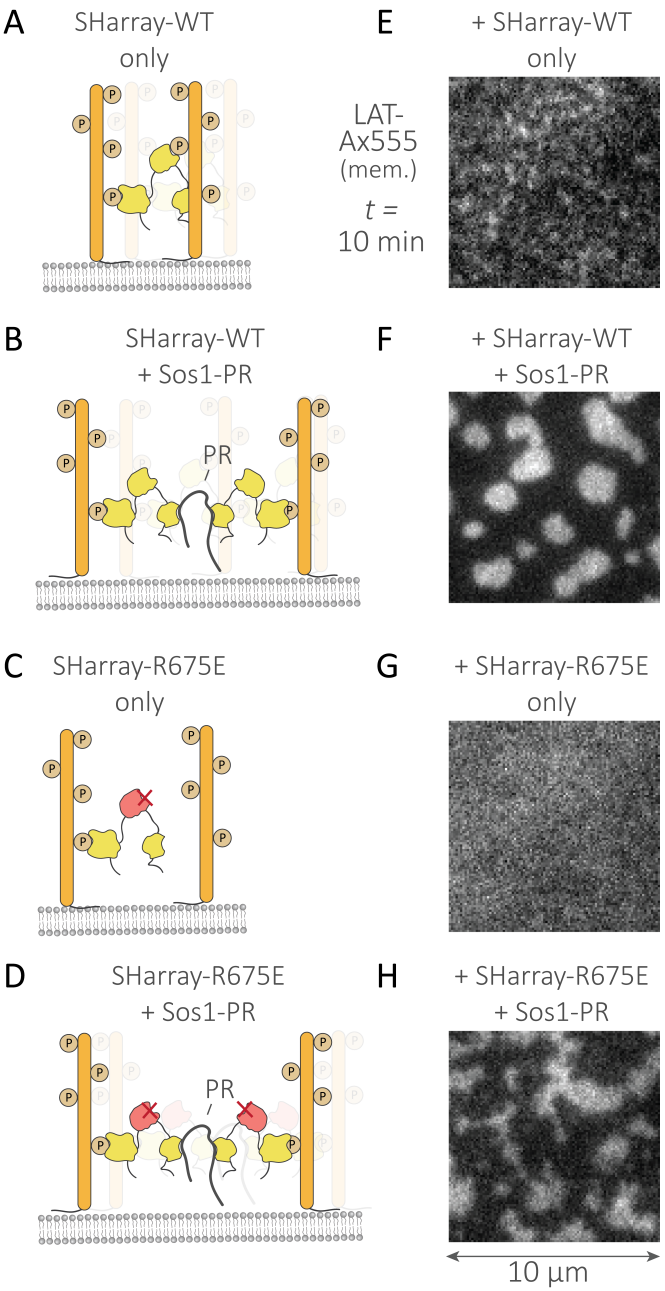


Figure 2.6: PLCγ1 SHarray can induce LAT condensation through SH2 and SH3 dependent interactions. **A-D**. Graphics depicting the binding and crosslinking dynamics of the PLCγ1 SHarray truncations to pLAT, corresponding to the experimental results to the right. **E-H**. TIRF images (10 µm x 10 µm) of Alexa555-labeled His10-LAT5Y (~1500 µm^{-2}, 15% labeled) after 10 min incubations with SHarray-WT alone (**E**), SHarray-WT and Sos1-PR (**F**), SHarray-R675E alone (**G**), or SHarray-R675E and Sos1-PR (**H**). Concentrations: 5 µM SHarray-WT/R675E, 2 µM Sos1-PR. Lipid composition (mol%): 98:2 DOPC:Ni-DGS.

Our results largely agreed with the previous study by Zeng et al. [58] (Fig 2.6). SHarray-WT visibly condensed pLAT on its own (Fig 2.6A,E), but the strength of the condensation was increased greatly by the Sos1-PR with much larger apparent domains (Fig 2.6B,F). In contrast, SHarray-R675E could not condense pLAT at all, with LAT remaining a homogeneous fast-diffusing species (Fig 2.6 C,G). Meanwhile, Sos1-PR was able to largely rescue the condensation capability of SHarray-R675E (Fig 2.6 D,H). Altogether, this suggests the SHarray can crosslink LAT through either nSH2:cSH2 mediated interactions or nSH2:SH3:PR mediated interactions with pLAT. In a perhaps negligible contradiction to

previous results, the SH3:PR interaction, in combination with nSH2 binding, seems to be the strongest of the possible configurations (Fig 2.6 B,F,D,H). With a cSH2-deletion construct (nSH2-SH3), Zeng et al. observed no condensation of LAT, though they did note a marked decrease in condensation with an nSH2-cSH2 construct compared to the full SHarray [58]. The differences may have been in the concentrations/densities of proteins used. Zeng et al. claimed their LAT densities were roughly 300 μm^{-2} and utilized PLCγ1 truncations at 50 nM with 300 nM of Sos1-PR. We used LAT at ~1500 μm^{-2} on the bilayer in order to more clearly visualize macroscopic condensation, and our SHarray and Sos1-PR concentrations were correspondingly larger at 5 μM and 2 μM respectively. It is not immediately clear how these concentrations would correlate to physiological conditions; LAT and its adapters are most likely at lower intracellular concentrations but do not exist in isolation and would be affected by significant molecular crowding [28]. Regardless, we argue this model system demonstrates the power of the SH3-PR interaction in contributing to pLAT condensation in cooperation with the SH2 domains. This is supported by preliminary results from our lab utilizing similar truncations *in vivo*, where the SHarray is capable of nucleating LAT condensates with either a cSH2 or SH3 deletion (but not with the deletion of both) [75].

It is interesting to consider how these interactions might play out in the physiological pathway. The evidence that PLCγ1 has a nucleating effect *in vivo* is convincing [31, 58, 75], but how might the cSH2 and SH3 mediated interactions differ from what we see here? The cSH2 domain has a critical role in activating PLCγ1 by the intramolecular high-affinity binding of PLCγ1-pY783 [59]. Will the phosphorylation and activation of PLCγ1 then affect its crosslinking ability through cSH2 interactions by introducing a competitive binding site? The *in vivo* SH3-PR interactions likely diverge from our model system as well, since the PLCγ1-SH3 binds preferentially to the PR of SLP76 [66-74]. There is an unclear picture of how LAT crosslinking may proceed through SLP76. The aforementioned PLCγ1:SLP76:Gads:pLAT quaternary structure has been well-documented [72, 74], but primarily in the context of monomeric LAT (binding in cis). Furthermore, "SLP76-clusters" have been observed that contain PLCγ1 but are spatially separated from LAT [73]. Perhaps, then, the picture of this complex system evolves over time—PLCγ1 may nucleate the pLAT condensate through SHarray-mediated crosslinking, become phosphorylated, then break away from LAT condensates due to decreased interactions of PLCγ1-cSH2 with pLAT. Bolstering this hypothesis, PLCγ1 activation has been observed to be timed according to LAT-pY132, but active PLCγ1 has been observed in populations spatially distinct from LAT clusters [107]. Future experiments in our lab could center around determining the contribution of PLCγ1-pY783 to SHarray-mediated pLAT condensation and studying the spatial organization of active PLCγ1.

2.6 Experimental Methods

Protein purifications and DNA cloning

All purified constructs utilized pET28a (Novagen-Cat. # 69864-3) or pETM (similar to Addgene #108943) backbones under the T7 promoter for expression in E. Coli. Expression vectors were transformed into BL21-CodonPlus competent E. Coli (Agilent) and cultured in TB. T7 expression was induced using 2 mM IPTG (final concentration) (Gold Biotechnology) overnight (18-20 hrs) at 18 °C with shaking. Pelleted cells were resuspended in bacterial lysis buffer typically containing 75 mM NaH2PO4 pH 8.0, 300-700 mM NaCl, 2 mM beta-mercaptoethanol (Sigma Aldrich), DNAse (Sigma Aldrich), 5-10 mM imidazole (Fisher Scientific), and 1-2 tablets of EDTA-free Pierce Protease Inhibitor Cocktail (A32965, ThermoFisher Scientific). All subsequent steps were done at 4 °C. Bacteria were lysed using an EmulsiFlex-C3 high-pressure homogenizer (Avestin). Subsequent steps are described for each protein below, with proteins generally stored at -80 °C in 20 mM Tris-HCl (pH 8 at 4 °C), 200 mM NaCl, 1 mM TCEP (Sigma Aldrich), and 10% glycerol (MCB grade, Fisher Scientific) after a final SEC polishing step (Superdex 75 or 200 column, 120 mL bed volume, Cytiva) and flash-freezing in liquid N2.

Full-length Grb2 (human) was expressed with a cleavable (TEV) N-terminal His6-tag and purified as described previously [57]. Grb2 was cleaved with TEV to remove the His6-tag before use. Where noted, Grb2 was incubated at 37 °C for 15 min in a thermocycler to allow dimerization.

His6-LAT1C (27-233 aa, human) was expressed with a cleavable (TEV) His6-tag (N-terminal) and with the mutation C117F. His6-LAT1C was otherwise purified as described previously [18]. The His6-tag was left intact for membrane tethering.

His10-LAT5Y (30-233 aa, human) was cloned from the His6-LAT1C plasmid using successive site-directed mutagenesis with the Q5 SDM kit (E0554S, New England Biolabs). His10-LAT5Y has an uncleavable N-terminal His10-tag with a SAGGSASAGGSA linker and contains the mutations: Y36F, Y45F, Y64F, Y70F, and Y110F. LAT was otherwise purified as described previously [18].

Hck (83-526 aa, human) was expressed with a cleavable (TEV) His6-tag and purified as described previously for Src-family kinases [95]. The His6-tag was left intact for membrane tethering. Of special note, the purification strategy utilized calls for co-expression of YopH phosphatase in the E. Coli host, which is essential to separate out for pLAT experiments. YopH seems to bind stubbornly to Hck (while running at a similar molecular weight in SDS-PAGE) and should be removed by high salt washes and careful ion exchange chromatography.

Sos1-PR (1,051–1,333 aa, human) was expressed with a cleavable (TEV) N-terminal His6-MBP-fusion tag and purified as described previously [28]. Of special note, it is essential this construct be purified by an ion exchange step (MonoS column, 1 mL bed volume, Cytiva) with high amounts of reducing agent (>10 mM BME for example). Sos1-PR seems to form strong adducts with MBP and bacterial contaminants which can strongly affect results downstream, but these adducts can be disrupted by ionic differences and reducing agents. Sos1-PR was cleaved with TEV to remove the His6-MBP-tag before use.

PLCγ1-SHarray-WT (550-851 aa, murine) was expressed with a cleavable (TEV) N-terminal His6-MBP-fusion tag and otherwise purified matching the protocol for Grb2. PLCγ1-SHarray-WT was cleaved with TEV to remove the His6-MBP-tag before use.

PLCγ1-SHarray-R675E (550-851 aa, murine) was cloned by SDM of the PLCγ1-SHarray-WT plasmid to introduce the R675E mutation (Q5 SDM kit). PLCγ1-SHarray-R675E was expressed with a cleavable (TEV) N-terminal His6-MBP-fusion tag and otherwise purified matching the protocol for Grb2. PLCγ1-SHarray-WT was cleaved with TEV to remove the His6-MBP-tag before use.

Fluorescent labeling of proteins

His6-LAT1C was labeled at residue C29 and His10-LAT5Y was labeled at C117, both using Alexa 555 C2 maleimide (Invitrogen) according to the manufacturer protocol. Briefly, LAT was diluted to 100 μM with 5 mM TCEP, then allowed to react with the maleimide dye for 2 hrs at room temperature before quenching with 10 mM BME. Excess Ax555 dye was initially removed by gravity desalting columns (PD10, Cytiva) and further by SEC via FPLC (Superdex 75 increase, 24 mL bed volume, Cytiva). Of special note, we have observed LAT to appear as multiple SEC peaks (up to 3 or more), but these do not seem to be distinct populations for our purposes (if isolated, they all behave nominally the same on SLBs). We suggest simply pooling all SEC peaks of LAT (given they are sufficiently pure). Labeled fraction was determined by comparison of absorption at the dye's λ_{max} to the protein's UV absorption at 280 nm (after correction for the dye's contribution at 280 nm [108]).

SUV and SLB preparation

Small unilamellar vesicles (SUVs) were made using 1,2-dioleoyl-sn-glycero-3-phosphocholine (DOPC), 1,2-dioleoyl-sn-glycero-3-[(N-carboxypentyl)iminidiacetic acid)succinyl] (nickel salt) (Ni2+-NTA-DGS), and L-α-phosphatidylinositol-4,5-bisphosphate (Brain, Porcine) (ammonium salt) (Brain PIP2) (Avanti Polar Lipids). Lipids were purchased, stored (-20 °C), and mixed solubilized in chloroform. Lipids were mixed in an etched round bottom flask to yield 2 mg total lipid mass at a ratio of 94:4:2 (mol%) DOPC:Ni-DGS:PIP2. After mixing well, lipids were dried by rotovap in a 37 °C water bath, kept under vacuum to dry an additional 10 min at room temperature, then dried under continuous N_2 gas flow for >30 min. Lipid films were solubilized with 2 mL milli-Q water (to yield 1 mg/mL lipid concentration) and vigorously vortexed to ensure film liftoff. The cloudy aqueous lipid mixture was added to a 5 mL polypropylene tube and treated by 3 mm stepped tip sonication

(Sonics VCX750 – 33% amplitude, 20 s sonication, 50 s rest, 5 cycles) while submerged in ice. The clarified SUV solution was then centrifuged at 20,000 g for 20 min to remove tip debris and any remaining large vesicles. The supernatant was stored at 4 °C in a sealed tube for use in experiments up to ~1 week.

Precision Schott D 263 M glass coverslips (#1.5H, 75 x 25 mm, custom ordered from ThorLabs, similar to Part# CG15CH) were first cleaned with warm 2% Hellmanex III (Fisher Scientific) solution with bath sonication at 45 °C for 30 min, then 50% IPA:mill-Q with sonication for >15 min, then milli-Q with sonication for >15 min. Substrates were then etched using a 1:3 ratio of concentrated H_2SO_4 to 30% H_2O_2 (piranha etch) for 3 min (while still warm). Substrates were rinsed excessively with milli-Q water between each cleaning step and after etching. Substrates were stored in milli-Q at room temperature for use in experiments up to ~1 week. To build chambers for experiments, etched substrates were blow-dried under N_2 and attached to simple 6-channel flow cells (sticky-Slide VI 0.4, ibidi). Chambers were cured at 37 °C for >10 min while pressed under a heavy weight. After curing, chambers were allowed to cool to room temperature for >10 min.

Supported lipid bilayers were formed via vesicle rupture. The 1 mg/mL SUV solution was diluted to 0.25 mg/mL in degassed 1X TBS. 100 µL of 0.25 mg/mL SUV (0.75X TBS) was added per chamber channel and incubated for >30 min at room temperature. Channels were washed via 1 mL degassed 1X TBS. SLBs were then blocked with 1 mg/mL casein solution (Blocker Casein, Thermo Scientific) diluted in 1X TBS for 10 min. Channels were exchanged to an incubation buffer (1X TBS, 2 mM $MgCl_2$, 1 mM TCEP). His-tagged membrane proteins were thawed, diluted in incubation buffer, then centrifuged at 20,000 g at 4 °C to remove aggregates before use. 100 nM His10-LAT5Y or 175 nM His6-LAT1C and 10 nM His6-Hck in incubation buffer (with 0.1 mg/mL casein) were added to bilayers (100 µL per channel) and incubated for 20 min (yields ~1500 μm^{-2} total LAT density). After an initial wash, channels were incubated in 1 mM ATP, 1 mM sodium orthovanadate, and 0.1 mg/mL casein in incubation buffer for 20 min to both phosphorylate LAT via Hck and to allow weakly chelated proteins to dissociate. After a secondary wash, channels were ready for experiments (used within ~1-4 hrs).

Imaging Hardware and Acquisition

TIRF imaging experiments were performed on an inverted Nikon Eclipse Ti microscope using a 100X Nikon oil-immersion TIRF objective (1.49 NA). We used a 1.5X lens tube (Nikon) before the camera for a total 150X magnification. Micro-positioning was done using a motor-controlled stage (MS-2000, ASI). Images were acquired with an iXon Ultra 897 EMCCD camera (Andor Technology). Fluorescent LAT-Ax555 was excited (~0.25 mW at the objective) with a 561 nm diode laser (OBIS laser diode; Coherent) controlled with a custom laser driver (Solamere Technology) using TTL signals from the camera. The laser was collimated with the objective position at the approximate sample z-focus before every experiment. A single quad-band dichroic cube was used for all acquisitions (ZT405/488/561/ 640rpcv2, Chroma). Fluorescence emission was additionally filtered by

an ET600/50M filter (Semrock). Microscope and accessory hardware were controlled using Micro-Manager, version 4.0 [109]. Experiments were conducted at 21-23 °C. Images were acquired with a 20 ms camera exposure and 500 EM gain, with 5-10 s delays between time points for time-lapse measurements. Background images (20-30) were collected before the addition of condensing agents to be used for field illumination ("shade") correction (to remove aberrations and uneven TIRF illumination). Corrections and quantitative image analyses were done in MATLAB.

Condensation experiments

All condensation experiments were performed in imaging buffer containing 1X TBS, 2 mM $MgCl_2$, 1 mM TCEP, 1 mM ATP, 1 mM sodium orthovanadate, 2 mM Trolox (UV treated), 10 mM BME, 0.1 mg/mL casein (final concentrations after addition of analytes/sensors). Trolox (Sigma Aldrich) was prepared as previously described [110]. Protein components were combined at stated concentrations and added as a single injection (100 µL). Background measurements were taken for 30 s before carefully injecting condensing agent solutions mid-acquisition (such that the objective focus was unaffected). Images were collected at 5-10 s intervals for as long as 1.5 hrs.

Small-batch SEC of Grb2

An aliquot of Grb2 Batch 1 was thawed on ice after storage at -80 °C. Aliquots of Grb2 "Batch 2 monomer" and "Batch 2 dimer" were from a purification completed the same day as these experiments and were never frozen. All steps were handled at 4 °C unless otherwise stated. 100 µL aliquots of Grb2 Batch 2 were heat treated as stated in a thermocycler. Heat-treated aliquots were cooled back to 4 °C. All aliquots were then centrifuged at 20,000 g for 10 min. The concentration was then measured via absorbance at 280 nm (ε: 37.93 $mM^{-1}cm^{-1}$) using a NanoDrop instrument (Thermo Scientific). A Superdex 75 Increase SEC column (24 mL bed volume, Cytiva) was equilibrated in 2 column volumes (CVs) of degassed SEC buffer containing 20 mM Tris-HCl (pH 8 at 4 °C), 200 mM NaCl, 1 mM TCEP, 5% glycerol using an AKTA Explorer FPLC system (GE HealthCare, now Cytiva) located in a laboratory cold room. All SEC steps were run at a flow rate of 1 mL per min. UV absorbance was tracked at 280 nm and 215 nm (not shown). Approximately 75 µL of each sample was loaded onto a 100 µL sample loop for injection onto the column. The sample loop was washed 3X with SEC buffer between samples. For each sample SEC run, at least 1.5 CV was eluted (starting from the volume of injection) before the injection of the next sample. Chromatograms were imported into and analyzed using MATLAB.

Chapter 3

Activity of PLCγ1 from lysate is diminished in LAT:Grb2 condensates

Joseph B. DeGrandchamp[1], Sameer Rajesh[2], Jay T. Groves[1]

[1] Department of Chemistry, University of California, Berkeley, Berkeley, United States
[2] Department of Molecular and Cellular Biology, University of California, Berkeley, Berkeley, United States

3.1 Abstract

Early T cell activation after antigen recognition proceeds through the release of calcium into the cytoplasm, a tightly regulated process directly downstream of the activation of the phospholipase C-γ1 (PLCγ1). PLCγ1, heavily autoinhibited in the cytosol and activated at the membrane, hydrolyzes its substrate PIP2 to the membrane molecule DAG and cytosolic second messenger IP3. Importantly, activation of PLCγ1 relies on phosphotyrosine-mediated recruitment to the membrane-bound scaffold LAT. LAT is also known to bind multivalently to cytosolic adapters, such as Grb2, to form extended protein phase transition condensates. This assembly has been shown to have a drastic regulatory effect on the activity of Sos1, an enzyme critical to the MAPK pathway, and recent research has demonstrated a potential structural role for PLCγ1 in the nucleation of the LAT condensate. However, it was still largely unknown what the role of PLCγ1 is in the assembly or if the assembly has signaling consequences for PLCγ1 activity. Due to the critical role of PLCγ1 in T cells, it is imperative to obtain a more complete understanding of this interaction. We utilized purified protein constructs and dilute mammalian cell lysate flowed over LAT-functionalized supported lipid bilayers to reconstitute these interactions in a controlled system. We determined the binding dynamics of PLCγ1 to phase condensed and uncondensed LAT via fluorescence imaging and measured PLCγ1 activity via fluorescent biosensors. We found PLCγ1 recruits heavily to the LAT:Grb2 condensate but its activity was surprisingly decreased, most likely due to the reduced ability of PLCγ1 to reach its substrate.

3.2 Introduction

Adaptive immunity is largely governed by the antigen discrimination power of T Cells. T Cells must be able to determine whether their T Cell Receptor (TCR) is binding to a true foreign antigen, lest they miss invasive pathogens or, alternatively, target the body's own cells. This power to distinguish binding events originates from events proximal to the TCR, such as the multistep recruitment and activation of the kinase Zap70 or its phosphorylation of the membrane scaffold LAT [5-6, 93]. More recently, the condensation of phosphorylated LAT (pLAT) via the multivalent binding of cytosolic adapters, including Grb2 and Sos1, has been realized as a key step in antigen discrimination [31]. The phospholipase PLCγ1, critical to the activation of T Cells through gating the release of intracellular calcium, recruits to and is activated at pLAT clusters and has demonstrated an ability to crosslink pLAT as well [58]. This immediately calls into question the effect of the pLAT condensate on PLCγ1 activation and enzymatic turnover—and thus T Cell activation itself.

LAT has four key pY residues that are phosphorylated by Zap70: Y132, Y171, Y191, and Y226 [23]. The pY132 is reserved exclusively for the recruitment of PLCγ1, while pY171, pY191, and pY226 allow for the multivalent binding of the cytosolic adaptor Grb2 [23-25]. pY171 and pY191 also compete for the Grb2-like adaptor Gads. Through self-dimerization and multivalent interactions with the Ras-activator Sos1, Grb2 can crosslink LAT monomers, which leads to extended assemblies characterized as phase-transitioned protein condensates [27-29, 57]. This condensation has demonstrated the ability to concentrate proteins at the membrane, and our lab recently showed how it enhances the activation of Sos1 [29].

Meanwhile, PLCγ1 is a large multi-domain enzyme that hydrolyzes phosphatidylinositol-4,5-bisphosphate (PIP2) at the cell membrane to the second messengers diacylglycerol (DAG) and inisotol-triphosphate (IP3) [59]. IP3 signals for the release of calcium stores and ultimately T Cell activation, while DAG feeds into the MAPK pathway and cell proliferation [9]. Due to its outsized role, PLCγ1 is kept under strict regulation by an autoinhibitory loop that obstructs its active site and membrane binding domains [59]. This loop contains an nSH2 domain, a cSH2 domain, and an SH3 domain (in sequence, as listed). The nSH2 binds to pY132 on LAT with high affinity and specificity, while the cSH2 binds intramolecularly upon phosphorylation of PLCγ1 at Y783 resulting in release of autoinhibition [59]. The SH3 domain additionally links PLCγ1 to LAT through the binding of the cytosolic scaffold SLP76. SLP76 binds to the SH3 domain of the Grb2-like adaptor Gads, which in turn binds back to LAT via pY171 and pY191 (competing with Grb2). Ultimately, this results in a multi-protein complex (PLCγ1:SLP76:Gads:LAT) facilitating the interaction of PLCγ1 with LAT and the membrane, where it can be phosphorylated and activated by the kinase ITK (also recruited to SLP76) [9, 59, 72, 74, 111].

The fates of PLCγ1 and LAT are clearly and inextricably linked, and thus it would be obvious to assume the condensation of pLAT through Grb2 is linked to PLCγ1 in some way as well.

The study of PLCγ1 activation in the condensation is, consequently, of great interest. However, PLCγ1, being large and difficult to purify, can be unwieldy to work with. And while its activation has been studied using purified constructs and solution assays [59, 74], there has never been the ability to get real-time information on its recruitment to pLAT and downstream activity simultaneously. We have previously developed a methodology for the study of active full-length Sos1 from mammalian cell lysate on Ras-functionalized supported lipid bilayers (SLBs) [39]. Herein, we apply a similar strategy to PLCγ1 using PLCγ1-mNG fusion constructs from lysate flowed over pLAT bilayers, tracking activity through the use of a labeled DAG binding domain. Using TIRF imaging for this assay, we are able to determine the spatial organization of our analytes at the membrane, concurrently observing PLCγ1 activity and pLAT condensation state. Through this analysis, we show that PLCγ1 activity is unexpectedly *weakened* by pLAT:Grb2 condensation.

3.3 Results

A quantitative activity assay for PLCγ1 direct from cell lysates

To facilitate the study of PLCγ1 activation, PLCγ1-mNG was first transfected into HEK293T cells. Lysate from the cells (generated by minimal sonication) was clarified by benchtop centrifugation, diluted in an imaging buffer (with phosphatase inhibitors), and flowed over pLAT-functionalized supported lipids bilayers (SLBs) with 2 mol% PIP2 content (Fig 3.1A). PLCγ1-mNG recruitment to LAT was successfully measured via TIRF imaging of surface mNG signal (Fig 3.1C). To determine whether PLCγ1-mNG actively hydrolyzed PIP2 to DAG, a DAG sensor was developed based on the C1b (DAG binding) domain of PKCθ fused with an N-terminal SNAP-tag (647 labeled) (Fig 3.1A). A similar construct has been utilized in live cells, and labeled binding domains have been well-characterized for use in reactions on SLBs [7, 29]. Surface fluorescence of the DAG sensor was tracked in sequence with PLCγ1-mNG (Fig 3.1C), with a low background signal giving way to a marked increase in intensity in line with PLCγ1-mNG fluorescence.

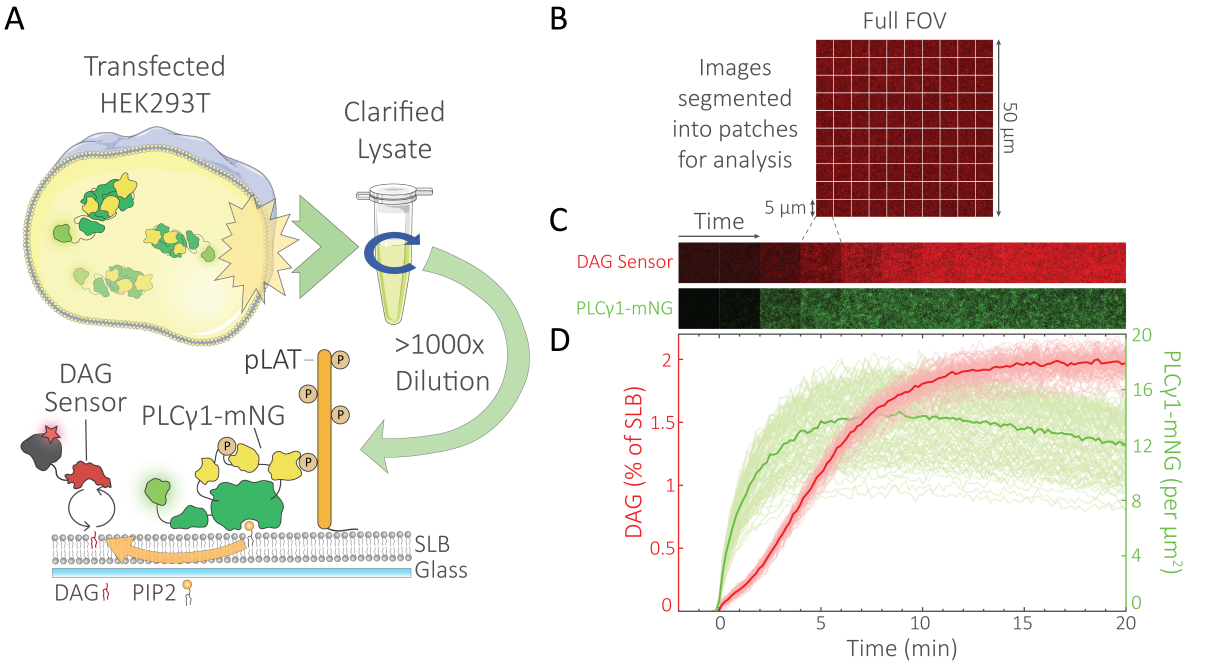


Figure 3.1: PLCγ1 activity and recruitment can be measured directly from lysate by TIRF imaging of supported lipid bilayers.

A. A schematic summarizing the lysate assay protocol. PLCγ1-mNG was generated in HEK293T cells, then flowed directly as dilute lysate over pLAT bilayers containing PIP2. Active PLCγ1-mNG hydrolyzed PIP2 to DAG, which was detected using a labeled DAG sensor (PKCθ-C1b-SNAP647). Parts of the figure were drawn using images from Servier Medical Art Commons Attribution 3.0 Unported License (http://smart.servier.com (accessed on 21 March 2022)). **B.** An example TIRF image of the DAG sensor demonstrating the segmentation of 50 x 50 μm images for analysis. TIRF images in a time series were sectioned into 5 x 5 μm patches and analyzed as separate instances. **C.** Images of a single 5 x 5 μm patch in the DAG sensor channel (Top) and PLCγ1-mNG channel (Bottom) through time, corresponding to the time axis for the curves below. **D.** Curves obtained from processing the raw median fluorescence from membrane patches, representing the amount of DAG in the bilayer (red, left axis, foreground curves) and density of PLCγ1-mNG recruited (green, right axis, background curves) over 20 minutes. PLCγ1-mNG lysate (~1:1000 dilution) with DAG sensor was injected at t = 0 min. To attain quantitative curves, raw fluorescence was first normalized to the time of injection. DAG was calibrated using the assumption that the average normalized maximum for multiple experiments must be 2% (given 2% PIP2 bilayers). PLCγ1-mNG was calibrated by matching single-molecule counts (at high laser power) to bulk fluorescence (at low laser power). The two solid, darkly colored curves represent the median of all patches analyzed. Lightly colored curves in the background represent the results from each single patch (n = 100). Lipid composition (mol%): 94:4:2 DOPC:Ni-DGS:PIP2. LAT density: ~1500 μm^{-2}.

The use of membrane corrals for the analysis of signaling reactions has been well-established [29]. Herein, we utilized a similar but distinct strategy by software segmentation of bilayers that are physically unpartitioned. TIRF images with a full Field of View (FOV) of 2500 μm^2 were separated into 25 μm^2 patches and analyzed as separate experiments (Fig 3.1B). This serves both to correct for differences across the image due to uneven illumination and aberrations and to reduce the effects of spurious outliers (such as rare aggregates or proteins

crashing onto membrane defects) which are often uncharacteristically intense. Median fluorescence across each patch was computed at each timepoint to yield raw fluorescence curves (of arbitrary units). To obtain quantitative results, a few reasonable assumptions were applied. Curves were first normalized to the point of injection. With the maximum mol% of DAG in the SLB fixed at 2% (capped by the amount of PIP2 in the bilayer), it can be assumed the eventual plateau of normalized DAG fluorescence signal corresponds to 2 mol% of DAG. The relative increase and plateau of normalized DAG signal were verified to be consistent over several experiments and over multiple days, allowing for the calculation of an average "intensity to DAG" coefficient to be applied across varied conditions (described in detail in the *Experimental Methods*). PLCγ1-mNG signal was similarly normalized and converted to PLCγ1-mNG densities at the bilayer by correlating bulk images (at low laser power) to images of countable PLCγ1-mNG (at high laser power) for varying PLCγ1-mNG concentrations. The resulting quantitative curves for a typical PLCγ1-mNG lysate assay on a pLAT bilayer show an increase in DAG following shortly after PLCγ1-mNG recruitment and an eventual total conversion of PIP2 after roughly 20 minutes (Fig 3.1D). There is good agreement across all patches analyzed (shown as lightly colored curves in the background). PLCγ1-mNG signal starts to decrease after roughly 90% of PIP2 has been hydrolyzed, potentially due to decreased membrane binding in the absence of substrate (in experiments with labeled LAT, there was no appreciable desorption of LAT detected over the experiment timeframe). The DAG production curves appear potentially sigmoidal, with a differential rate noticeable in the initial few minutes. However, in the assay's current form, this is hard to separate from solution perturbation introduced by the injection of the lysate/sensor mixture into the channel. If the curve were truly sigmoidal, it would indicate more is occurring than simple recruitment of active PLCγ1 [112]; perhaps an activation step at the bilayer? In fact, it was not immediately clear in our assays how PLCγ1-mNG was being activated, as the requirement for phosphorylation of PLCγ1-Y783 and subsequent intramolecular reorganization for activation has long been substantiated [59]. In that regard, additional characterizations of the lysate and the assay were conducted.

PLCγ1 activity requires both a kinase and pLAT

A western blot of control cell lysates and lysates containing PLCγ1-mNG probed for total PLCγ1 content indicated the presence of endogenous PLCγ1 (a near-ubiquitous protein) (Fig 3.2A). However, exogenously expressed PLCγ1-mNG was roughly six times more abundant relative to the endogenous species (Fig 3.2B), in line with the ratio found for past results for Sos1-EGFP from lysate [39]. In addition, PLCγ1-mNG showed good stability over 60 minutes at room temperature, with limited changes in lower molecular weight bands indicative of proteolysis (Fig 3.2A).

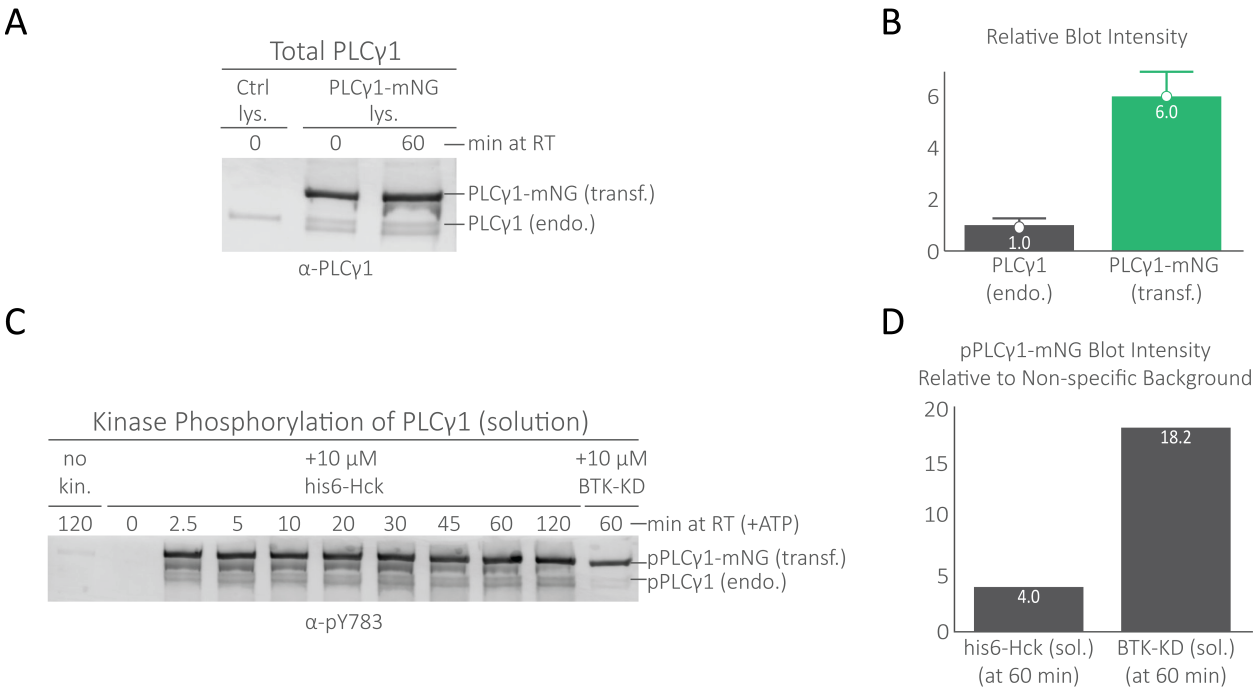


Figure 3.2: PLCγ1-mNG transfected in HEK293T is several times more abundant than endogenous species and can be activated by *in vitro* phosphorylation.

A. Western blot probed for total PLCγ1 content. Cells for control lysate were transfected with transfection reagents alone (left lane). Cells for PLCγ1-mNG lysate received exogenous expression vectors (middle and rightmost lanes). PLCγ1-mNG lysates were loaded after either 0 min (middle) or 60 min (right) at RT to determine the stability of PLCγ1-mNG against degradation. Each lane was loaded with 1 μL of lysate. **B.** Relative blot intensities (background corrected) for endogenous PLCγ1 (left, grey) versus transfected PLCγ1-mNG (right, green) normalized to endogenous levels (n=2). **C.** Western blot probed for pY783 with a series of time points and different kinase conditions. Phosphorylation reactions were conducted in 10 μL volumes containing 1 μL of PLCγ1-mNG lysate each, ATP, phosphatase inhibitor, and kinase in buffer. Reactions were kept at RT for the designated time, then quenched with SDS-PAGE loading buffer. Either no kinase, His6-Hck, or BTK-KD (Kinase Domain) was used. **D.** Blot intensities (background corrected) of pPLCγ1-mNG normalized to non-specific pY bands.

While there is a visible band (below endogenous PLCγ1) that may correspond to the absence of mNG (due to cleavage or misfolding), the majority of PLCγ1-mNG remained intact. The small difference in the lower band may be due to species differences. PLCγ1-mNG was constructed using the murine sequence due to availability, while the endogenous species in HEK293T cells would have the human sequence. Importantly, the two sequences have 97% residue similarity and a difference of only 12 residues in length (~1 kDa), and the differences are not expected to affect results strongly as evidenced by the frequent use of rat PLCγ1 in other studies [59, 74].

With regards to the activation of PLCγ1 by phosphorylation, a pY783 specific antibody reveals PLCγ1 can be strongly phosphorylated *in vitro* (Fig 3.2C). There is essentially zero phosphorylation of PLCγ1 at an initial time point (aliquots were thawed after being flash-

frozen immediately following lysis). After two hours, there remained minimal detectable pPLCγ1, indicating a negligible contribution from endogenous kinases. Meanwhile, Hck, a commonly employed and abundant promiscuous kinase, phosphorylated PLCγ1 fully within a few minutes (Fig 3.2C) [28-29]. A dark band corresponding to PLCγ1-mNG appeared quickly with Hck incubation and did not get more intense in subsequent time points, indicating maximal phosphorylation. The His6-Hck construct in this assay is also utilized on our SLBs to phosphorylate LAT (Fig 3.3A) and is thus a prime suspect in the mystery of PLCγ1 activation in our assays. In addition, the kinase domain of BTK (BTK-KD) was able to phosphorylate PLCγ1 to a similar level in solution (Fig 3.2C). BTK activates PLCγ2 in B-Cells and is a close family member of ITK, the PLCγ1 activator in T-Cells. BTK exhibited remarkable selectivity for the phosphorylation of PLCγ1 compared to Hck (Fig 3.2D, Supplementary Fig 1). In future iterations of this assay, BTK (or ITK) might serve as better activators at the membrane.

To further characterize the current assay and the requirements for PLCγ1 activation, a careful series of control conditions and PLCγ1 mutations were examined (Fig 3.3B). To facilitate comparisons between conditions, an observed enzymatic velocity (v_{obs}) was extracted from the linear portion of each DAG production curve. For example, the slope of the previously discussed DAG curves was calculated between 2.5 and 5 minutes (Fig 3.1D). To simplify comparisons of PLCγ1-mNG density, the maximum value for each patch was considered. v_{obs} and PLCγ1-mNG density values were tabulated for each membrane patch and each condition, then normalized relative to the median of the PLCγ1-mNG-WT condition and visualized using dual-axes half-violin plots (Fig 3.3B). In the absence of pLAT (no Hck on the membrane), PLCγ1 recruitment and activity were both abolished. Control lysate showed a similar lack of activity, with a median v_{obs} (m_v) corresponding to only 4% of the m_v for PLCγ1-mNG-WT lysate (and no PLCγ1-mNG, as would be expected).

To assess the importance of Y783 to activation, phenylalanine mutants were generated to abrogate PLCγ1 phosphorylation. We introduced the Y783F mutation as well as a triple mutation referred to as "3F" that included Y771F and Y775F (adjacent PLCγ1 tyrosines also implicated in *in vivo* activation) in addition to Y783F [113]. Lysate from cells transfected with these constructs showed robust recruitment of PLCγ1-mNG to pLAT but had corresponding v_{obs} equivalent to control lysate (Fig 3.3B). Our results show the Y783F mutation was sufficient to fully inhibit PLCγ1. Differences in observed PLCγ1-mNG density between the WT and mutants were most likely due to expression levels of the constructs in the HEK293T cells rather than anything mechanistic. While transfection efficiencies were roughly 80% for all constructs and the numbers of cells lysed were similar, cell-to-cell or cell cycle variation in expression was not accounted for. PLCγ1-mNG-WT also showed similar batch-to-batch differences (a single batch of cell lysate was used for all experiments in this study). Closer examination would be required to fully decipher any differences in recruitment between the constructs.

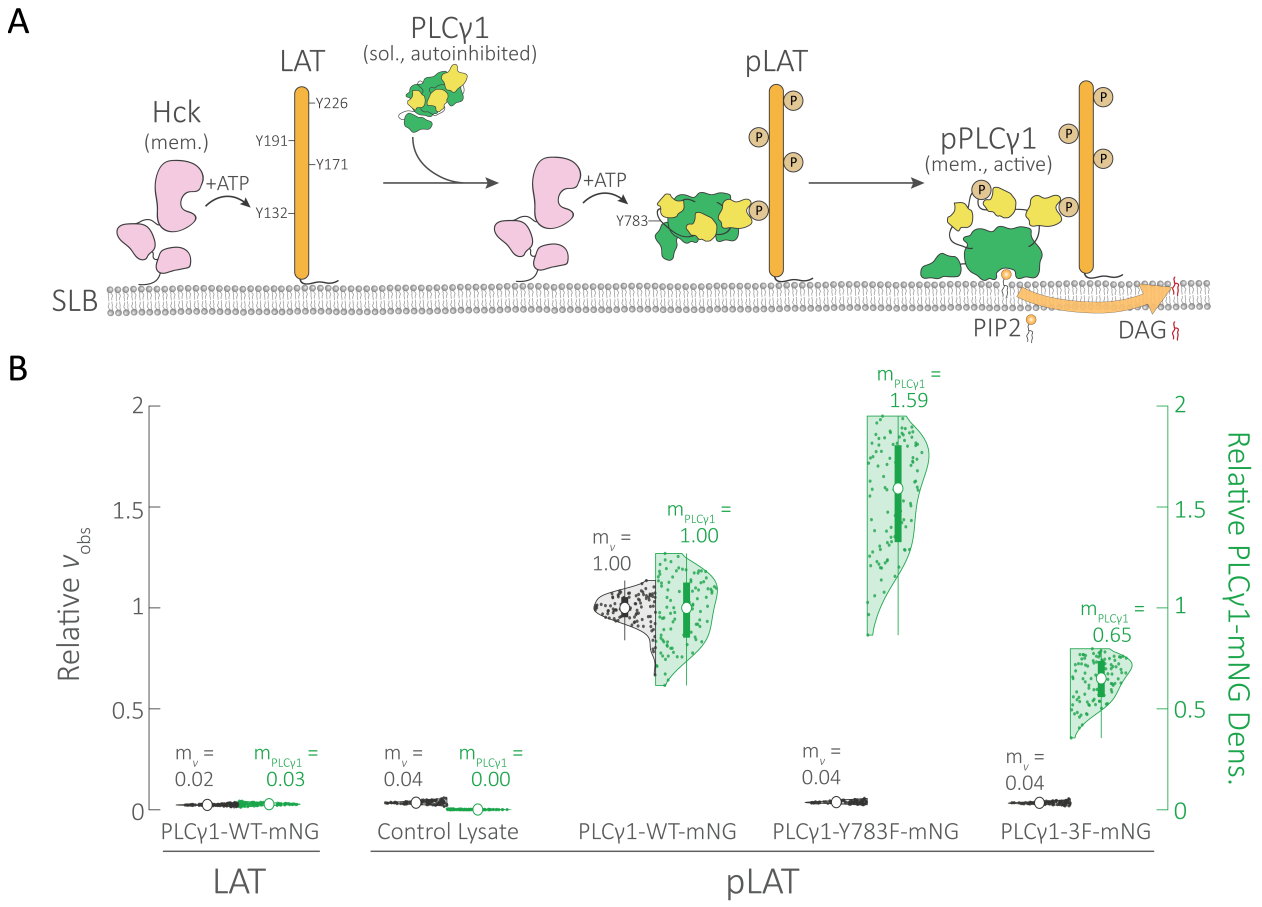


Figure 3.3: PLCγ1 requires pLAT and phosphorylation at Y783 to activate on the membrane.
A. A schematic showing greater detail of the lysate experiment at the membrane. Hck and LAT are functionalized to the SLB via Ni-histidine chelation. Hck phosphorylates LAT allowing for the recruitment of PLCγ1-mNG. PLCγ1-mNG is then subsequently phosphorylated by Hck at Y783 and is active at the membrane after structural rearrangement. **B.** Relative observed enzymatic velocities (v_{obs}) (black, left axis, defined as the enzymatic rate for the linear portion of the reaction trace) and PLCγ1-mNG densities (green, right axis, defined as maximum density over 20 min time trace) for various assay conditions, normalized to the median value for PLCγ1-WT-mNG lysate on a pLAT bilayer. Distributions of 100 membrane patches are shown as half-violin plots, with single observations shown as points and distributions represented by a shaded area. Compact box plots are overlayed over the distributions to represent the median (white circles), quartile regions (box), and extremes with outliers excluded (whiskers). Median values for v_{obs} (m_v) and PLCγ1-mNG density ($m_{PLCγ1}$) are expressly denoted for clarity. Lipid composition (mol%): 94:4:2 DOPC:Ni-DGS:PIP2. LAT densities: ~1500 μm^{-2}.

These results are in agreement with previous studies claiming PLCγ1 requires both a phosphorylated receptor and phosphorylation of pY783 for full activation at the membrane [59, 74]. Notably, even pPLCγ1-mNG (pre-phosphorylated in solution by BTK-KD) does not recruit to or hydrolyze PIP2 in membranes devoid of LAT (Supplementary Fig 2B). The full mechanism of our *in vitro* lysate assay is then most likely to be as depicted in Fig 3.3A. Hck first phosphorylates LAT on the bilayer, PLCγ1 from lysate is introduced and recruits to

pLAT, PLCγ1-Y783 is also phosphorylated by Hck, and ultimately PLCγ1 actively hydrolyzes PIP2 to DAG. With the basics of the assay established, additional components from the *in vivo* signaling system were added to illuminate further PLCγ1 interactions.

PLCγ1 localizes strongly to pLAT:Grb2 condensates but displays diminished activity

Recent studies of PLCγ1 in a condensate-forming growth-receptor pathway suggest condensation plays a role in increasing the observed activity of PLCγ1 [79]. pLAT has been shown to form condensates primarily via crosslinking by Grb2 and Sos1 in cells and *in vitro*, and PLCγ1 was recently seen to participate in these condensates [58]. Therefore, it seemed likely pLAT:Grb2 condensation would have an effect on PLCγ1 activity. To elucidate any possible effect, we utilized purified forms of Grb2 and Sos1-PR to condense LAT while performing our PLCγ1 lysate assay. With the addition of these adaptors, labeled LAT partitioned into strongly condensed phases as expected, with no visible effect from the presence of lysate (Fig 3.4A). PLCγ1-mNG also localized into these condensed phases, as seen in TIRF images where shapes formed by PLCγ1-mNG are similar to those of LAT-Ax555 (Fig 3.4A-B). The DAG sensor meanwhile seemed unaffected at the imaging time utilized, remaining visibly homogeneous (Fig 3.4C).

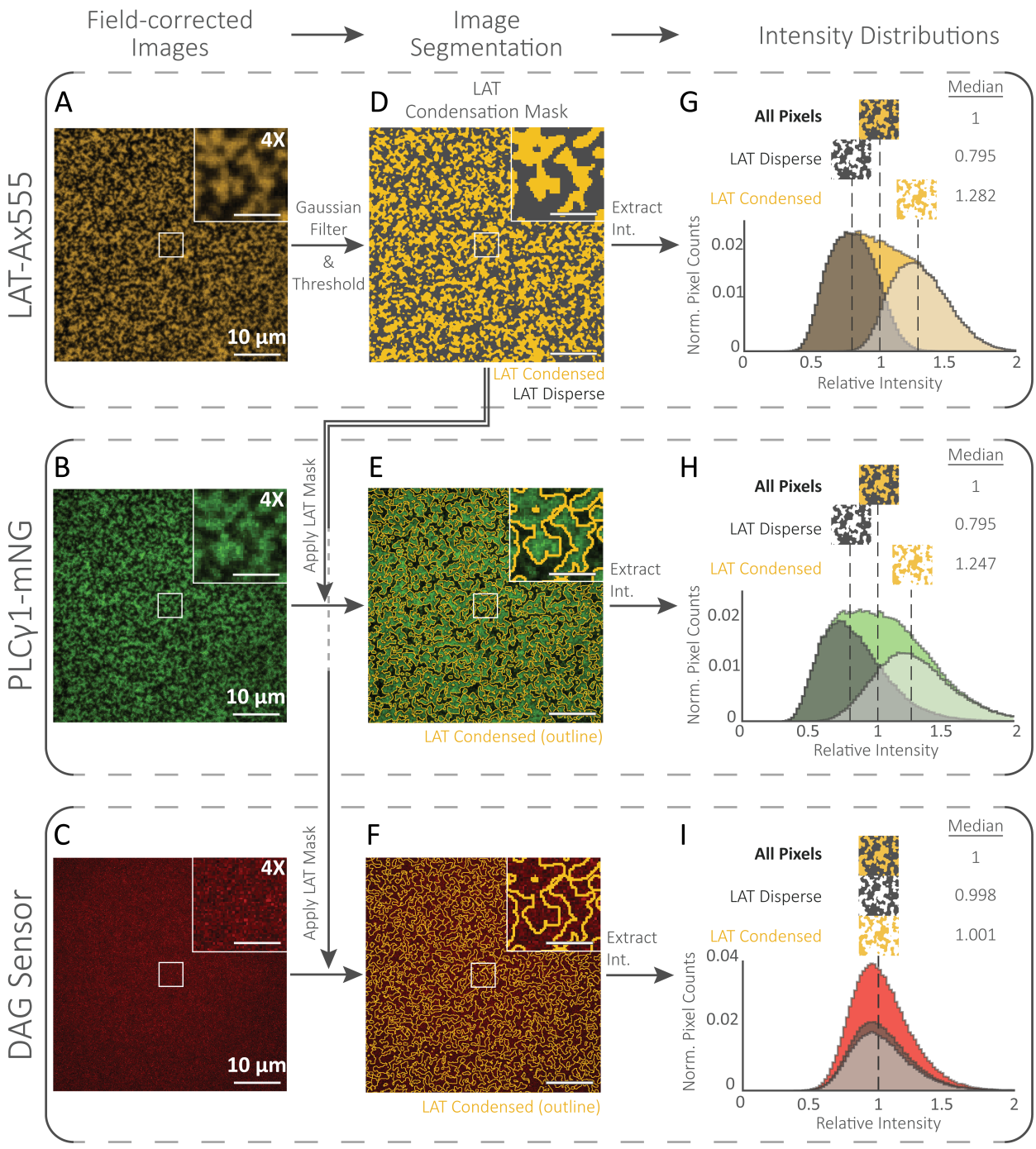


Figure 3.4: PLCγ1 localizes to the LAT:Grb2:Sos1 condensate, but DAG sensor is not affected at relevant timescales.

A-C. Field-corrected images of LAT-Ax555 (gold, top), PLCγ1-mNG (green, middle), and DAG sensor (red, bottom) with 5 µM Grb2 and 2 µM Sos1-PR in solution. The entire FOV is 50 x 50 µm (scale bar = 10 µm) with an inset showing a 4X expansion of the center 5 x 5 µm patch (scale bar = 2.5 µm). **D.** A binary image mask for LAT segmented into condensed (gold) and disperse (grey) areas obtained

from Gaussian filtration (σ=1) and thresholding of the LAT-Ax555 image in (**A**). Inset and scale bars are equivalent to those in (**A**). **E-F**. Images showing the effect of applying the binary LAT mask to PLCγ1-mNG (green) and DAG sensor (red) channels. Only the outline of the applied mask is shown for visibility. Insets and scale bars are equivalent to those in (**B-C**). **G-I.** Histograms of relative pixel intensities for LAT-Ax555 (gold, top), PLCγ1-mNG (green, middle), and DAG sensor (red, bottom). Pixel intensities were normalized to the median value for all pixels. Values greater than 1 indicate an increase in brightness from the overall median, while values less than 1 indicate a decrease. Histograms for all pixels are displayed in full color in the background. Histograms for pixels that are in areas of condensed LAT are shown in translucent white in the foreground. Pixel histograms for disperse LAT areas are shown in translucent grey. Dotted lines denoting the median of each histogram are decorated with an icon corresponding to the LAT mask for all pixels (gold and grey), LAT condensed (gold only), or LAT disperse (grey only). Median fold change values for each histogram are displayed in the top right for clarity. Lipid compositions for all experiments (mol%): 94:4:2 DOPC:Ni-DGS:PIP2. LAT density: ~1500 μm^{-2} (10% labeled).

To quantitatively characterize the localization of PLCγ1-mNG and determine any possible effects of the condensate on our assay, we employed an image analysis technique comprised of image segmentation and pixel mapping. We created a binary "LAT condensation mask" (0 for pixels outside condensed areas, 1 for pixels in condensed areas) by putting an image of LAT-Ax555 through a gaussian filter, then applying an appropriate threshold (Fig 3.4D). We then applied this mask to pixels from the original LAT image as well as images from the PLCγ1-mNG and DAG sensor channels (Fig 3.4E-F). The outline of the applied mask in Fig 3.4E contains most of the visible PLCγ1-mNG, while in Fig 3.4F there appears to be no difference in DAG sensor intensity inside and outside the masked area. Pixel intensities were normalized to the median of the entire image and then visualized in histograms (Fig 3.4G-I). Histograms for pixels across the entire image (unsegmented) for LAT and PLCγ1 show characteristics of multiple underlying (but unresolved) gaussian distributions (Fig 3.4G-H). However, by mapping pixels by the condensed/disperse state of LAT, the underlying distributions were successfully resolved. Pixels in LAT-condensed areas for both LAT-Ax555 and PLCγ1-mNG images had a median intensity 1.2-1.3 times brighter than the whole image (and ~1.6 times brighter than disperse areas) (Fig 3.4G-H). Pixels in the corresponding DAG image were homogenously distributed, regardless of the mapped state of LAT, with differences in relative median intensity of less than 0.002 (Fig 3.4I). This substantiates the claim that PLCγ1 is detectably recruited to pLAT:Grb2 condensates, and that our DAG sensor is not affected by the dense matrix (at relevant timescales). The DAG sensor also eventually reaches the same saturation (of 2 mol%) as uncondensed conditions (Supplementary Fig 3A). With this established, we could move on to analyzing the activity of PLCγ1 within condensates.

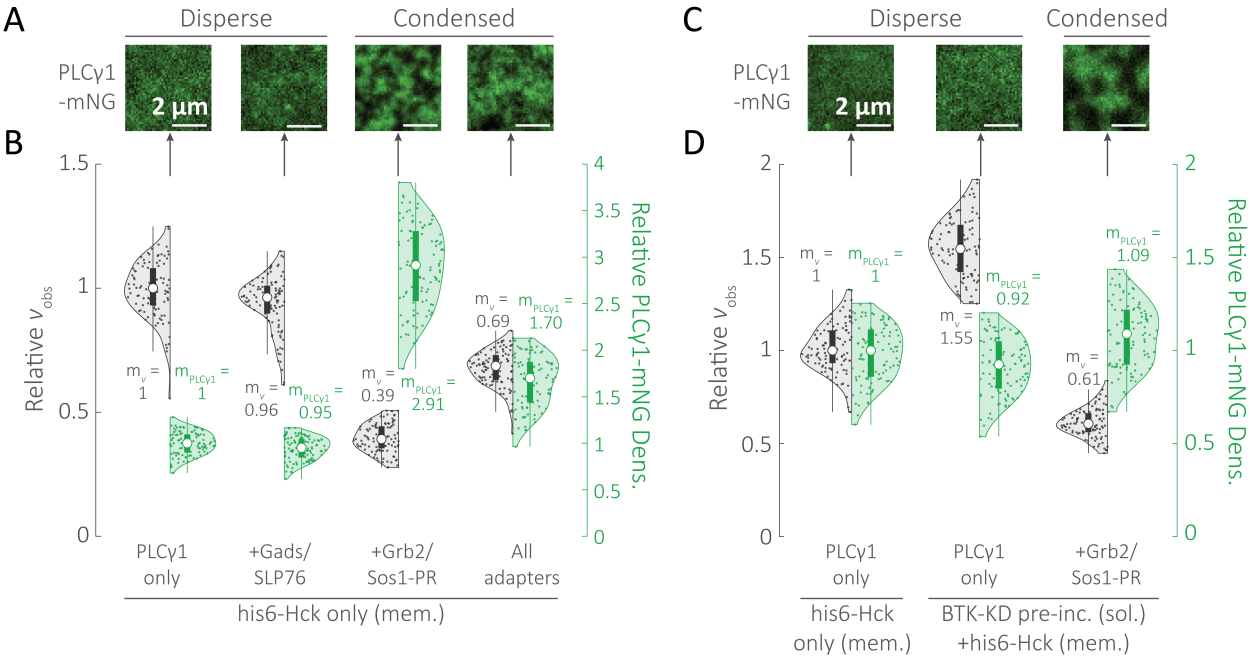


Figure 3.5: PLCγ1 activity is markedly reduced in LAT:Grb2 condensates, regardless of phosphorylation state.

A. TIRF images (5 x 5 μm, scale bars = 2 μm) of PLCγ1-mNG in different conditions corresponding to the distributions below. From left to right: PLCγ1-mNG only (with 2 μL control lysate), PLCγ1-mNG + Gads/SLP76 (from lysate, 1 μL each), PLCγ1-mNG + Grb2/Sos1-PR (purified, 6 μM:2 μM respectively), and PLCγ1-mNG + all previously described adapters. LAT-Ax555 (10% labeled) was used in this experiment but was determined to have negligible contribution in the PLCγ1-mNG channel. **B.** Half-violin plots showing distributions of relative v_{obs} (grey, left axis) and relative PLCγ1-mNG density (green, right axis), normalized to PLCγ1 only conditions. Compact box plots overlay the distributions to convey statistics. Median values for v_{obs} (m_v) and PLCγ1-mNG density ($m_{PLCγ1}$) are expressly denoted for clarity. **C.** TIRF images (5 x 5 μm, scale bars = 2 μm) of PLCγ1-mNG in different conditions corresponding to the distributions below. From left to right: PLCγ1-mNG only (no control lysate), PLCγ1-mNG pre-phosphorylated by 1 μM BTK-KD in solution for 1 hr, and similarly pre-phosphorylated PLCγ1-mNG + Grb2/Sos1-PR (purified, 6 μM:2 μM respectively). Hck was on the membrane for all experiments. Unlabeled LAT was used in this experiment. **D.** Half-violin plots showing distributions of relative v_{obs} (grey, left axis) and relative PLCγ1-mNG density (green, right axis), normalized to PLCγ1 only conditions (no pre-phosphorylation). Compact box plots overlay the distributions to convey statistics. Median values for v_{obs} (m_v) and PLCγ1-mNG density ($m_{PLCγ1}$) are expressly denoted for clarity. Lipid compositions for all experiments (mol%): 94:4:2 DOPC:Ni-DGS:PIP2. LAT densities: ~1500 μm^{-2}.

Interestingly, it is immediately apparent from measurements of v_{obs} in condensing conditions (with Grb2 and Sos1-PR) that the activity of PLCγ1 is *decreased* in LAT:Grb2 condensates, even with an increase in overall PLCγ1-mNG density (Fig 3.5B). The median value for v_{obs} (m_v) for the Grb2/Sos1-PR condition is only 40% of the uncondensed condition, despite a nearly threefold increase in PLCγ1-mNG (maximum over 20 minutes). But while Grb2 and Sos1 are thought to be the main mediators of pLAT condensation and are capable of interacting with PLCγ1, Gads and SLP76 are the canonical partners of PLCγ1 in this system

[72, 74, 111]. To determine potential differences in these adapters, Gads and SLP76 were expressed in HEK293T cells to generate lysate with full-length versions of these proteins (which have been shown to be troublesome in purified form) (Supplementary Fig 3B) [72]. To make fair comparisons, control lysate was added to the other conditions to provide roughly equivalent amounts of endogenous protein among all trials. Activity due to endogenous PLCγ1 was higher than previous experiments but still reasonably low compared to PLCγ1-mNG conditions (Supplementary Fig 3C). When Gads/SLP76 were added to PLCγ1 alone, they had little effect on recruitment or activity (within error) and did not lead to condensate formation (Fig 3.5A-B). However, when added in addition to Grb2/Sos1-PR in condensing conditions, m_v nearly doubled and peak PLCγ1-mNG density returned closer to uncondensed levels. The structure of the condensation also appeared changed (Fig 3.5A).

LAT condensates have the potential to exclude membrane proteins [27]. With membrane-tethered Hck as the primary source of PLCγ1 phosphorylation, there was a possibility pLAT condensation was excluding Hck, leading to slower PLCγ1 phosphorylation and decreases in v_{obs} in condensates. To see if that was the case, we pre-phosphorylated PLCγ1 using BTK-KD in solution before addition to pLAT bilayers. Observed rates for pPLCγ1 were significantly higher than PLCγ1 phosphorylated by Hck alone, but the rate still dropped after introducing Grb2/Sos1-PR (Fig 3.5C-D). If the m_v for condensed pPLCγ1 were computed relative to uncondensed pPLCγ1 (rather than PLCγ1), it would be 0.39, equivalent to the relative rate for the experiment with no pre-phosphorylation (Fig 3.5B). Of note, the experiments in Fig 3.5A-B had labeled LAT-Ax555 (not shown) and had control lysate or Gads/SLP-76 lysate in addition to PLCγ1-mNG. The experiments in Fig 3.5C-D were done with unlabeled LAT and with only PLCγ1-mNG lysate, indicating little effect from these variables on the result.

3.4 Discussion

Studies on PLCγ1 activation have been done for many years and in many formats [59, 74, 115] but this constitutes the first assay that quantitatively measured PLCγ1 recruitment and activity together in real-time. In addition, proteins in our assay interacted in a physiologically relevant geometry, and their spatial organization on the membrane was tracked. The use of unprocessed cell lysates also allowed for incorporation of proteins that are difficult to purify and for the introduction of mutants with relatively low effort and short turnaround times. As demonstrated previously, this remains a powerful strategy for the study of signaling reactions at the membrane [39].

Our data agree well with studies on the mechanisms of PLCγ1 activation in T Cells, showing pLAT and pY783 are required for full activation (Fig 3.3B, Fig 3.6A) [9]. What was previously unknown: how is PLCγ1 activity affected by the condensation of pLAT by Grb2? *In vivo* research on membrane proximal DAG signaling in T Cells has suggested essential elements of antigen discrimination occur between the recruitment of Zap70 and the recruitment of DAG effectors [7]. This painted a clear target on pLAT and PLCγ1 as major players in kinetic proofreading. Recent results from our lab further revealed LAT condensation is an essential piece of the puzzle, seemingly integrating signals from binding events across the cell [31]. PLCγ1 has already demonstrated the ability to partition into LAT:Grb2 condensates (and enhance their formation) [58]. Additionally, PLCγ1 in a parallel growth-receptor pathway condensation displayed a relative increase in activity [79]. Taken together, it would appear as if the incorporation of PLCγ1 into the LAT:Grb2 condensation would increase its activity, which would be a clear indicator of how LAT condensation could gatekeep T Cell activation.

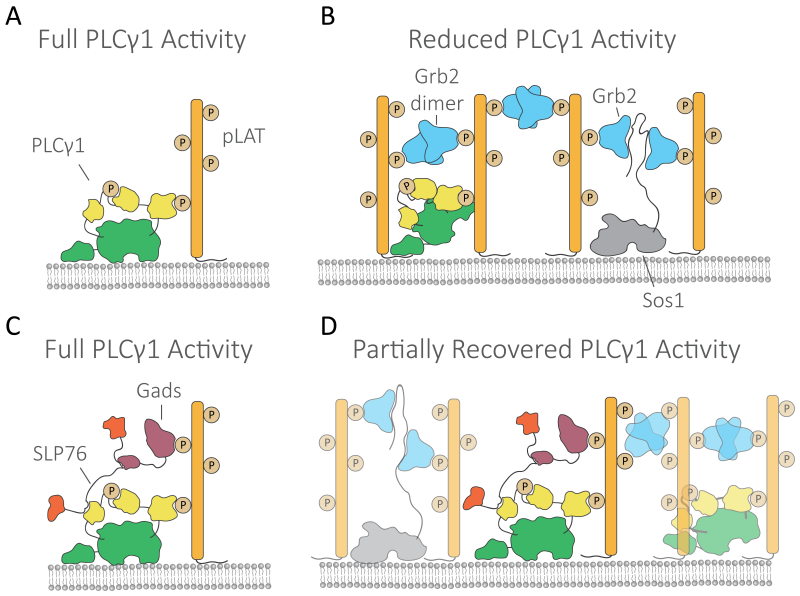


Figure 3.6: States of PLCγ1 activity in and out of the LAT:Grb2 condensate.
A. Graphic of PLCγ1 binding to pLAT and fully engaging the membrane, where full PLCγ1 activity is observed in experimental results. **B.** A graphic of PLCγ1 in the LAT:Grb2 condensate, where PLCγ1 activity is reduced in experiments. Both Grb2 dimers and Grb2:Sos1-PR interactions can crosslink LAT. **C.** Graphic showing PLCγ1 interactions with Gads/SLP76 in the absence of a larger condensate. PLCγ1 is fully active in experiments with this configuration. **D.** Graphic of PLCγ1/Gads/SLP76 interactions in the LAT:Grb2 condensate, where PLCγ1 activity is partially recovered compared to Grb2-only conditions.

Remarkably, our study shows pLAT:Grb2 condensation has a *negative* effect on PLCγ1 activity (Fig 3.5B). While this may not be the full picture given the number of components involved in *in vivo* LAT condensates not included here, this is strong evidence not all condensates are the same and simply enhancing enzyme concentrations or dwell time is not always the effect of condensation. But why is PLCγ1 activity affected negatively? And if

uncondensed pLAT is clearly capable of providing a scaffold for fully engaged PLCγ1 (Fig 3.3B, Fig 3.6A), then what is the purpose of having pLAT condense at all in cells?

The mechanism of PLCγ1 inhibition in pLAT:Grb2 condensates cannot be fully deduced from this study, but it is worth noting a few possibilities. pLAT can be crosslinked via Grb2/Sos1 both through Grb2 alone (through dimerization) and through Grb2 SH3 to Sos1 PR interactions [27-30, 57]. While it has not been studied extensively, the condensation of pLAT through Grb2 dimers would likely be very densely packed. A dense condensation has the potential to obstruct or otherwise affect the structure of PLCγ1 and thus affect its activity (Fig 3.6B). Grb2 alone does indeed have a negative effect on PLCγ1 activity (Supplementary Fig 3D). Sos1, which has demonstrated enhanced activation by pLAT condensation [29], may be less obstructed due to its extended PR domain and differential binding via Grb2 (Fig 3.6B). The addition of Gads/SLP76, meanwhile, may affect the packing around PLCγ1, since they preferentially bind each other (and Gads competes with Grb2 for pLAT binding) (Fig 3.6C-D). Truncated forms of Gads/SLP76 also had difficulty in condensing pLAT on their own and so might have the effect of somewhat dispersing pLAT, as seems to be the case in our experimental images (Fig 3.5A) [58].

It is also worth considering Grb2 itself could bind PLCγ1 in an inhibitory way, as Grb2 has been shown to have rather unexpected effects on seemingly unrelated enzymes [114]. Mutants of Grb2 that do not dimerize could be studied with PLCγ1 to separate this effect (if any) from condensation [57]. There is evidence as well that Gads and SLP76 have an activating effect on PLCγ1 additive to its activation by Y783 phosphorylation [74]. While PLCγ1 activity does not seem increased by the simple addition of Gads and SLP76 in our study (Fig 3.5B), the previous study used truncated adaptors and concentrations several times that of PLCγ1. The full-length adaptors in our study were used in roughly equimolar amounts with PLCγ1. Addition of increasing adaptor concentrations could show interesting results in our system as well.

Then, why have pLAT condensates? Notably, our system is missing the canonical activator of PLCγ1 in T Cells, ITK [9]. ITK is purportedly recruited to phosphorylated residues on SLP76, and thus pLAT condensation may bring the kinase in close proximity to its substrate, PLCγ1. Then, PLCγ1 might require the pLAT condensation to be phosphorylated but might leave the condensate to become fully active. There is evidence for PLCγ1 activity at the membrane away from LAT and for SLP76-containing assemblies breaking off of pLAT condensates due to cytoskeletal interactions [73, 107]. Alternatively, LAT condensation might play a role in protecting phosphorylated populations of LAT from phosphatases, having shown the potential to exclude CD45 [27]. LAT condensation could be required for there to be any pLAT at all for PLCγ1 to recruit to in the first place.

The validation of our assay here makes possible a vast number of PLCγ1 studies. PLCγ1 is ubiquitously expressed and an important part in growth receptor signaling. How does PLCγ1 get activated in the EGFR pathway in non-lymphocytes, for example, where condensation is also possible but Gads/SLP-76 are not expressed [57]? The degree of processivity of PLCγ1

is not well understood, and single molecule evaluations using our assay could elucidate this. PLCγ1 is, of course, also a well-known oncogene with several mutations that have gone unstudied or have had difficult-to-understand mechanisms [59]. The use of PLCγ1 from lysate makes mutational studies much more accessible.

3.5 Experimental Methods

Mammalian expression plasmids and constructs

Full-length PLCγ1 with a C-terminal mNG fusion protein (mus musculus), Gads (human), and SLP-76 (human) were cloned into a pCI backbone under the CMV promoter for expression in HEK293T cells (U47119.2). The PLCγ1 sequence was a gift from M. O'Dair (UC Berkeley). Gads and SLP-76 were cloned from MGC cDNA purchased from Dharmacon Inc. (now Horizon Discovery) (Gads: BC025692.1, SLP-76: BC016618.1).

Cell transfection and lysate preparation

HEK293T cells were transfected similarly to previously published methods [39]. HEK293T cells (UCB Cell Culture Facility) were seeded in clear bottom 6-well plates (Eppendorf) at a target confluency of 90% after allowing for adhesion overnight. Cells were cultured in DMEM medium, high glucose media (DMEM, Gibco) supplemented with 10% fetal bovine serum (heat shocked), minimal essential medium (MEM) non-essential amino acid and 100 μg ml−1 penicillin and streptomycin, and media was not changed before or after transfection. Cells were transiently transfected with exogenous vectors using Lipofectamine 3000 (Invitrogen) according to the manufacturer protocol for 6-well plates and with 3.75 μL volumes of the reagent. After allowing for >48 hrs of expression (no media change), transfection efficiency was evaluated using epifluorescence (for PLCγ1-mNG) and bright field microscopy. Typical efficiency (based on mNG fluorescence) was >80%. After verifying high transfection efficiency, media was aspirated, and cells were collected in sterile 1X TBS. Cells were pelleted (1 well resulted in a ~50 μL pellet) by gentle centrifugation and resuspended in 450 μL lysis buffer containing 20 mM Tris-HCl pH 7.4, 150 mM NaCl, 1% protease inhibitor cocktail (P8340, Sigma Aldrich), and 0.5% each of phosphatase inhibitor cocktails 2 (P0044, Sigma) and 3 (P5726, Sigma Aldrich).

Cells were lysed by 3 mm tapered tip sonication (Sonics VCX750 – 20% amplitude, 2 s sonication, 6 s rest, 20 cycles) in a 5 mL polypropylene tube immersed in an ice bath. Lysate was centrifuged at 20,000 g for 30 min at 4 °C. The supernatant was collected (leaving ~50 μL in the tube), aliquoted, flash-frozen in liquid N_2, and stored at -80 °C (used in experiments for up to ~1 yr). Proteins seemed to maintain good stability (as demonstrated by PLCγ1 activity) without the use of glycerol, but 5-10% glycerol might be considered to increase stability.

Western blots

For western blotting, 1 μL of lysate per lane was thawed, treated as stated, and run on SurePAGE 4-12% Bis-Tris SDS–PAGE gels (GenScript) in 1X MES SDS-PAGE buffer and transferred to nitrocellulose membranes (Invitrogen) in 1X NuPAGE Transfer Buffer (Invitrogen). Approximate molecular weights were visualized using Precision Plus Protein Dual Xtra standards (Bio-Rad), which effectively transfer to membranes as well. Membranes were washed with 1X TBST and blocked with 5% BSA in TBST. The membranes were incubated with either PLCγ1 (D9H10) XP rabbit mAb (Cell Signaling Technology, 1:1000 dilution), phospho-PLCγ1 (Tyr783) (D6M9S) rabbit mAb (Cell Signaling Technology, 1:1000 dilution), SLP-76 (D1R1A) rabbit mAb (Cell Signaling Technology, 1:1000 dilution), or Gads (UW40) mouse mAb conjugated with Alexa 647 (Santa Cruz Biotechnology, 1:200 dilution) overnight at 4 °C with agitation. Membranes were then incubated with Goat anti-Rabbit IgG (H+L) conjugated to Alexa 647 (A-21244, Invitrogen, 1:20,000 dilution) at room temperature for 1 hr with agitation. Bands were visualized by fluorescence at 640 nm using a Typhoon FLA 9500 laser scanner (Cytiva). Band intensities and backgrounds were quantified using the Fiji software package.

Solution kinase reactions

1 μL of lysate per reaction was thawed then diluted in reaction buffer containing 20 mM Tris-HCl pH 7.4, 150 mM NaCl, 20 mM $MgCl_2$, 1 mM ATP (Sigma Aldrich), 1 mM activated sodium orthovanadate (508605, Calbiochem). Either Milli-Q water, 10 μM His6-Hck, or 10 μM BTK-KD was added for a final volume of 12 μL. After the stated time, reactions were quenched with 3 μL of 5X SDS-PAGE loading buffer. The entire 15 μL volume was loaded for SDS-PAGE, and results were visualized by western blot as above.

Protein purifications

All purified constructs (save for BTK-KD, see below) utilized pET28a (Novagen-Cat. # 69864-3) or pETM (similar to Addgene #108943) backbones under the T7 promoter for expression in *E. Coli*. Expression vectors were transformed into BL21-CodonPlus competent *E. Coli* (Agilent) and cultured in TB. T7 expression was induced using 2 mM IPTG (final concentration) (Gold Biotechnology) overnight (18-20 hrs) at 18 °C with shaking. Pelleted cells were resuspended in bacterial lysis buffer typically containing 75 mM NaH_2PO_4 pH 8.0, 300-700 mM NaCl, 2 mM beta-mercaptoethanol (Sigma Aldrich), DNAse (Sigma Aldrich), 5-10 mM imidazole (Fisher Scientific), and 1-2 tablets of EDTA-free Pierce Protease Inhibitor Cocktail (A32965, ThermoFisher Scientific). All subsequent steps were done at 4 °C. Bacteria were lysed using an EmulsiFlex-C3 high-pressure homogenizer (Avestin). Subsequent steps are described for each protein below, with proteins generally stored at -80 °C in 20 mM Tris-HCl (pH 8 at 4 °C), 200 mM NaCl, 1 mM TCEP (Sigma Aldrich), and 10% glycerol (MCB grade, Fisher Scientific) after a final SEC polishing step (Superdex 75 or 200 column, 120 mL bed volume, Cytiva) and flash-freezing in liquid N_2.

Full-length Grb2 (human) was expressed with a cleavable (TEV) N-terminal His6-tag and purified as described previously [57]. Grb2 was cleaved with TEV to remove the His6-tag. Of special note, Grb2 was incubated at 37 °C for 15 min in a thermocycler to allow dimerization before using it in experiments [57].

PKCθ-C1b domain (232-282 aa, mus musculus) ("DAG Sensor") was expressed with a C-terminal SNAPtag fusion protein (SAGGSASAGGSA linker) and purified equivalently to Grb2 using an N-terminal His6-tag. Of special note, growth media for C1b expression was supplemented with 0.01 mM $ZnSO_4$ (final concentration) [115]. PKCθ-C1b-SNAP was cleaved with TEV to remove the His6-tag. The C1b sequence was a gift from D. Tischer (UCSF).

LAT (30-233 aa, human) was expressed with an uncleavable His10-tag with a SAGGSASAGGSA linker and with the mutations: Y36F, Y45F, Y64F, Y70F, and Y110F. LAT was otherwise purified as described previously [116].

Hck (83-526 aa, human) was expressed with a cleavable (TEV) His6-tag and purified as described previously for Src-family kinases [95]. The His6-tag was left intact for membrane tethering. Of special note, the purification strategy utilized calls for co-expression of YopH phosphatase in the *E. Coli* host, which is essential to separate out for pLAT experiments. YopH seems to bind stubbornly to Hck (while running at a similar molecular weight in SDS-PAGE) and should be removed by high salt washes and careful ion exchange chromatography.

Sos1-PR domain (1,051–1,333 aa, human) was expressed with a cleavable (TEV) N-terminal His6-MBP-fusion tag and purified as described previously [28]. Of special note, it is essential that this construct be purified by an ion exchange step (MonoS column, 1 mL bed volume, Cytiva) with high amounts of reducing agent (>10 mM BME for example). Sos1-PR seems to form strong adducts with MBP and bacterial contaminants which can strongly affect results downstream, but these adducts can be disrupted by ionic differences and reducing agents. Sos1-PR was cleaved with TEV to remove the His6-MBP-tag before use.

BTK kinase domain (402-659 aa, human) was purified and gifted by L. Nocka (UC Berkeley). The purification was done in insect cells as described previously for other kinase domains [116].

PLCδ pleckstrin homology domain (11-140 aa, human) ("PIP2 Sensor") was purified and gifted by A.Y. Lee (UC Berkeley). Purification and labeling were as previously described [110].

Fluorescent labeling of proteins

PKCθ-C1b-SNAP (DAG sensor) was labeled with SNAP-Surface Alexa 647 (S9136S, New England Biolabs) according to the manufacturer protocol. LAT was labeled at residue C117 using Alexa 555 C2 maleimide (Invitrogen) according to the manufacturer protocol. Briefly, LAT was diluted to 100 μM with 5 mM TCEP, then allowed to react with the maleimide dye for 2 hrs at room temperature before quenching with 10 mM BME. Excess SNAP647 or Ax555 dye was initially removed by gravity desalting columns (PD10, Cytiva) and further by SEC via FPLC (Superdex 75 increase, 24 mL bed volume, Cytiva). Of special note, we have observed LAT to appear as multiple SEC peaks (up to 3 or more), but these do not seem to be distinct populations for our purposes (if isolated, they all behave nominally the same on SLBs). We suggest simply pooling all SEC peaks of LAT (given they are sufficiently pure). Labeled fraction was determined by comparison of absorption at the dye's λ_{max} to the protein's UV absorption at 280 nm (after correction for the dye's contribution at 280 nm [108]).

SUV and SLB preparation

Small unilamellar vesicles (SUVs) were made using 1,2-dioleoyl-sn-glycero-3-phosphocholine (DOPC), 1,2-dioleoyl-sn-glycero-3-[(N-carboxypentyl)iminidiacetic acid)succinyl] (nickel salt) (Ni2+-NTA-DGS), and L-α-phosphatidylinositol-4,5-bisphosphate (Brain, Porcine) (ammonium salt) (Brain PIP2) (Avanti Polar Lipids). Lipids were purchased, stored (-20 °C), and mixed solubilized in chloroform. Lipids were mixed in an etched round bottom flask to yield 2 mg total lipid mass at a ratio of 94:4:2 (mol%) DOPC:Ni-DGS:PIP2. After mixing well, lipids were dried by rotovap in a 37 °C water bath, kept under vacuum to dry an additional 10 min at room temperature, then dried under continuous N_2 gas flow for >30 min. Lipid films were solubilized with 2 mL milli-Q water (to yield 1 mg/mL lipid concentration) and vigorously vortexed to ensure film liftoff. The cloudy aqueous lipid mixture was added to a 5 mL polypropylene tube and treated by 3 mm stepped tip sonication (Sonics VCX750 – 33% amplitude, 20 s sonication, 50 s rest, 5 cycles) while submerged in ice. The clarified SUV solution was then centrifuged at 20,000 g for 20 min to remove tip debris and any remaining large vesicles. The supernatant was stored at 4 °C in a sealed tube for use in experiments up to ~1 week.

Precision Schott D 263 M glass coverslips (#1.5H, 75 x 25 mm, custom ordered from ThorLabs, similar to Part# CG15CH) were first cleaned with warm 2% Hellmanex III (Fisher Scientific) solution with bath sonication at 45 °C for 30 min, then 50% IPA:mill-Q with sonication for >15 min, then milli-Q with sonication for >15 min. Substrates were then etched using a 1:3 ratio of concentrated H_2SO_4 to 30% H_2O_2 (piranha etch) for 3 min (while still warm). Substrates were rinsed excessively with milli-Q water between each cleaning step and after etching. Substrates were stored in milli-Q at room temperature for use in experiments up to ~1 week. To build chambers for experiments, etched substrates were blow-dried under N_2 and attached to simple 6-channel flow cells (sticky-Slide VI 0.4, ibidi). Chambers were cured at 37 °C for >10 min while pressed under a heavy weight. After curing,

chambers were allowed to cool to room temperature for >10 min.

Supported lipid bilayers were formed via vesicle rupture. The 1 mg/mL SUV solution was diluted to 0.25 mg/mL in degassed 1X TBS. 100 μL of 0.25 mg/mL SUV (0.75X TBS) was added per chamber channel and incubated for >30 min at room temperature. Channels were washed via 1 mL degassed 1X TBS. SLBs were then blocked with 1 mg/mL casein solution (Blocker Casein, Thermo Scientific) diluted in 1X TBS for 10 min. Channels were exchanged to an incubation buffer (1X TBS, 2 mM $MgCl_2$, 1 mM TCEP). His10-LAT and His6-Hck were thawed, diluted in incubation buffer, then centrifuged at 20,000 g at 4 °C to remove aggregates before use. 100 nM His10-LAT and 10 nM His6-Hck in incubation buffer (with 0.1 mg/mL casein) were added to bilayers (100 μL per channel) and incubated for 20 min (yields ~1500 μm^{-2} LAT density). After an initial wash, channels were incubated in 1 mM ATP, 1 mM sodium orthovanadate, and 0.1 mg/mL casein in incubation buffer for 20 min to both phosphorylate LAT via Hck and to allow weakly chelated proteins to dissociate. After a secondary wash, channels were ready for experiments (used within ~1-4 hrs).

Imaging Hardware and Acquisition

TIRF imaging experiments were performed on an inverted Nikon Eclipse Ti microscope using a 100X Nikon oil-immersion TIRF objective (1.49 NA). We used a 1.5X lens tube (Nikon) before the camera for a total 150X magnification. Micro-positioning was done using a motor-controlled stage (MS-2000, ASI). Images were acquired with an iXon Ultra 897 EMCCD camera (Andor Technology). Fluorescently labeled proteins were excited with either a 488-, 561-, or 637-nm diode laser (OBIS laser diode; Coherent) controlled with a custom laser driver (Solamere Technology) using TTL signals from the camera. Lasers were collimated with the objective position at the approximate sample z-focus before every experiment. A single quad-band dichroic cube was used for all acquisitions (ZT405/488/561/640rpcv2, Chroma). Fluorescence emission was additionally filtered by: ET525/50M (488 excitation), ET600/50M (561 excitation), or ET700/75M (637 excitation) (Semrock). Microscope and accessory hardware were controlled using Micro-Manager, version 4.0 [109]. Experiments were conducted at 21-23 °C. Excitation conditions for each channel during background collection and kinetic measurements were as follows: PLCγ1-mNG was excited at 488 nm (~0.45 mW at the objective), LAT-Ax555 was excited at 561 nm (~0.25 mW at the objective), and DAG sensor was excited at 637 nm (~0.2 mW at the objective). All channels were acquired with a 20 ms camera exposure and 500 EM gain, with 5-10 s delays between time points for time-lapse measurements. Images for kinetic traces were taken with the objective focused on the center of the channel of interest. Background images (20-30) were collected before and after kinetic measurement to be used for field illumination ("shade") correction (to remove aberrations and uneven TIRF illumination). Corrections and quantitative image analyses were done in MATLAB.

Lysate assay kinetic acquisitions

All kinetic measurements were performed using imaging buffer containing 1X TBS, 2 mM $MgCl_2$, 1 mM TCEP, 1 mM ATP, 1 mM sodium orthovanadate, 2 mM Trolox (UV treated), 10 mM BME, 0.1 mg/mL casein (final concentrations after addition of analytes/sensors). Trolox (Sigma Aldrich) was prepared as previously described [110]. 1 µL of lysate and 200 nM DAG sensor were used unless otherwise stated. When adaptors were included (Grb2/Sos1/Gads/SLP-76), components were combined at stated concentrations and added as a single injection. DAG sensor was first incubated in channels for >10 min in imaging buffer to collect background images, allow nonspecific equilibration of the sensor at the membrane, and aid in finding the objective z-focus. Background measurements were taken for 30 s before carefully injecting lysate/DAG sensor solutions mid-acquisition (such that the objective focus was unaffected). Images were collected at 5-10 s intervals for as long as 1.5 hrs.

Image Analysis and Segmentation

Quick visualizations and quality checks of TIRF images were done using FIJI [117]. For quantitation, images were imported into MATLAB using custom scripts. MATLAB was then used for cropping, field correction, patch segmentation, and subsequent trace analyses. For kinetic traces, the raw value for each timepoint is the median pixel intensity of the corresponding patch. Traces were then normalized to the time of injection (for each patch, separately). Calibrations were then applied as described below. For the creation of the LAT condensation mask (Fig 3.4D), the built-in MATLAB function imgaussfilt was used ($\sigma = 1$) and an empirically-determined threshold equivalent to the median (filtered) intensity was applied. All plotting was also done using MATLAB.

Quantitative calibrations

LAT-Ax555 density was calibrated as previously described [28]. Briefly, a series of SLBs with increasing LAT density were prepared. TIRF images were taken of each channel, followed immediately by Fluorescence Correlation Spectroscopy (FCS) measurements. Densities calculated from FCS fits were correlated with median TIRF intensities to create a calibration curve.

For the conversion of raw fluorescence to DAG (in mol%), normalized DAG sensor traces were first cataloged for several experiments (with 1 µL PLCγ1-mNG lysate) of over multiple days (n = 10). Given that all experiments had approximately 2 mol% PIP2 in the bilayer (with some random error due to imperfect mixing, etc.), it was assumed the DAG sensor trace should plateau at 2 mol% DAG after full conversion of PIP2 (which was typically close to 20 min of reaction time for this condition). The median for all cataloged traces ($I_{norm.\ med.}$) was computed, and an "intensity to DAG" coefficient, ε_{DAG}, was defined and computed such that $\%\ DAG = I_{norm.\ med.} \times \varepsilon_{DAG}$. The empirical value for ε_{DAG} was calculated to be 0.880±0.08 (mol% DAG) / (norm. intensity) (1σ, n = 10), indicating an acceptable consistency in the

measurement.

For PLCγ1-mNG density (in μm^{-2}), TIRF images of PLCγ1-mNG were taken at varying concentrations that allowed for single molecule counting (at high laser powers). Images at the low laser power used for kinetic measurements (~0.45 mW at the objective) and images at high laser power (~10 mW at the objective) were taken in quick succession. The high-power images were analyzed using the TrackMate plugin of FIJI in order to count the number of PLCγ1-mNG present [118]. The single molecule counts were then correlated with the low-power images to calculate the approximate density of PLCγ1-mNG from their TIRF fluorescence intensity (background corrected).

v_{obs} measurements

Given that PLCγ1 activation is likely a multistep process, the true enzymatic rate cannot be measured by bulk measurements (the measured PLCγ1-mNG density is not necessarily the active density). Instead, we defined an observed velocity, v_{obs}, to be the linear steady-state rate of DAG production apparent in our data and utilized this for comparison of varied experimental configurations. To calculate v_{obs}, the linear portion for every DAG curve (patch by patch) was determined by finding the best linear fit (highest r^2) for a moving time-axis window. In detail: for every curve, in MATLAB, we performed a scan from $t_{0.1}$ (time to reach 10% of the maximum) to $t_{0.9}$ (time to reach 90% of the maximum). Through linear regression, we calculated the slope and r^2 correlation coefficient using a moving fixed-size time window across this section. The slope corresponding to the highest r^2 was stored as the v_{obs} for the curve in question.

3.6 Supplementary Figures

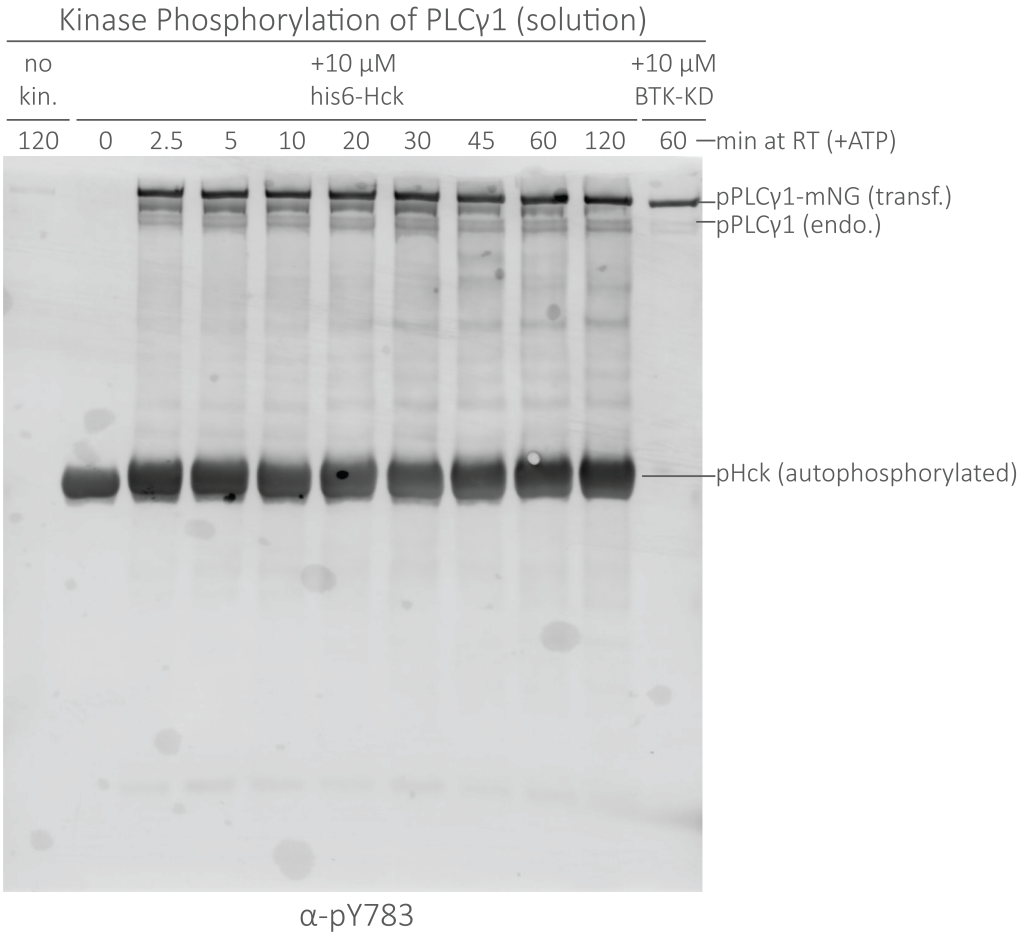


Figure 3.7: Supplementary Figure 1. Full Western Blot of *in vitro* PLCγ1 phosphorylation.
The full Western Blot from **Figure 3.2C**. Western blot probed for pY783 with a series of time points and different kinase conditions. Phosphorylation reactions were conducted in 10 μL volumes containing 1 μL of PLCγ1-mNG lysate each, kept at RT for the designated time, then quenched with SDS-PAGE loading buffer. Either no kinase, His6-Hck (FL), or BTK-KD (Kinase Domain) was used. While α-PLCγ1-pY783 antibody was used, other phosphoproteins were also detected in the background. pHck appears prevalently as a large band in lanes where it was included. Hck lanes also demonstrate a much higher general background, with many proteins in the lysate presumably being phosphorylated. In contrast, BTK-KD shows relatively specific activity for PLCγ1-Y783.

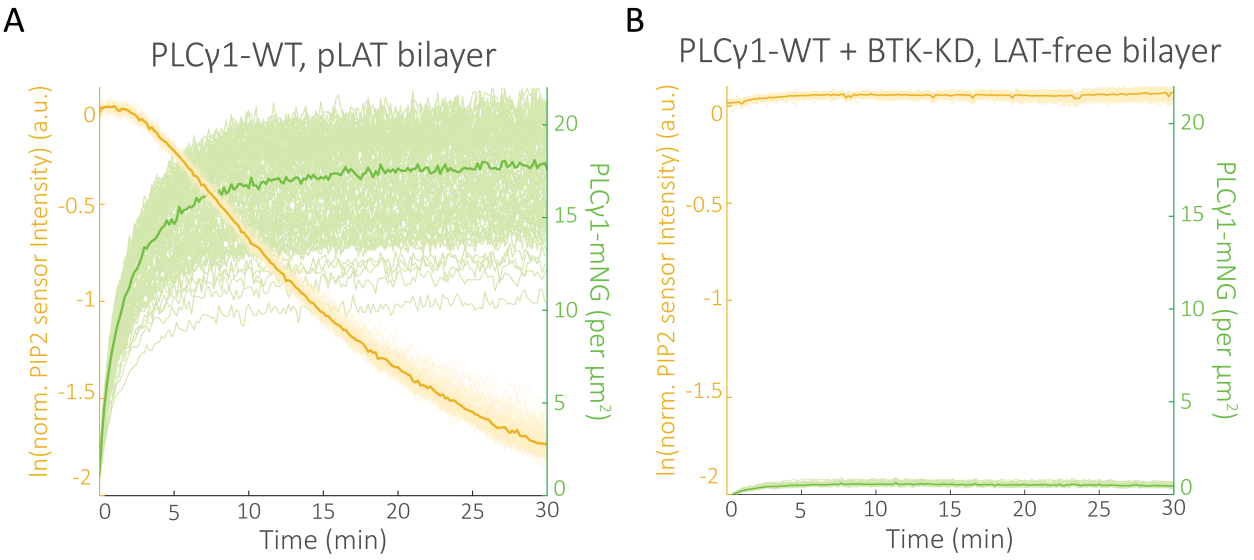


Figure 3.8: Supplementary Figure 2. Lysate assay with PIP2 sensor and pPLCγ1-mNG on a LAT-free bilayer.

A-B. Curves obtained from processing the raw median fluorescence from membrane patches, representing the amount of PIP2 in the bilayer (gold, left axes, top curves) and density of PLCγ1-mNG recruited (green, right axes, bottom curves) over 30 minutes for either a pLAT functionalized bilayer (**A**) or a LAT-free bilayer with pre-phosphorylated pPLCγ1-mNG (**B**). pPLCγ1-mNG was generated by incubating PLCγ1-mNG with 1 μM BTK-KD for 1 hr prior to injection. PLCγ1-mNG lysate (~1:1000 dilution) with PIP2 sensor (Cy3-PLCδ-PH) was injected at t = 0 min. A decay in PIP2 sensor intensity correlates to hydrolysis by PLCγ1-mNG. PLCγ1-mNG density curves were attained using calibrations after normalization to the time of injection. Solid, darkly colored curves represent the median of all membrane patches analyzed. Lightly colored curves in the background represent the results from each single patch (n = 100).

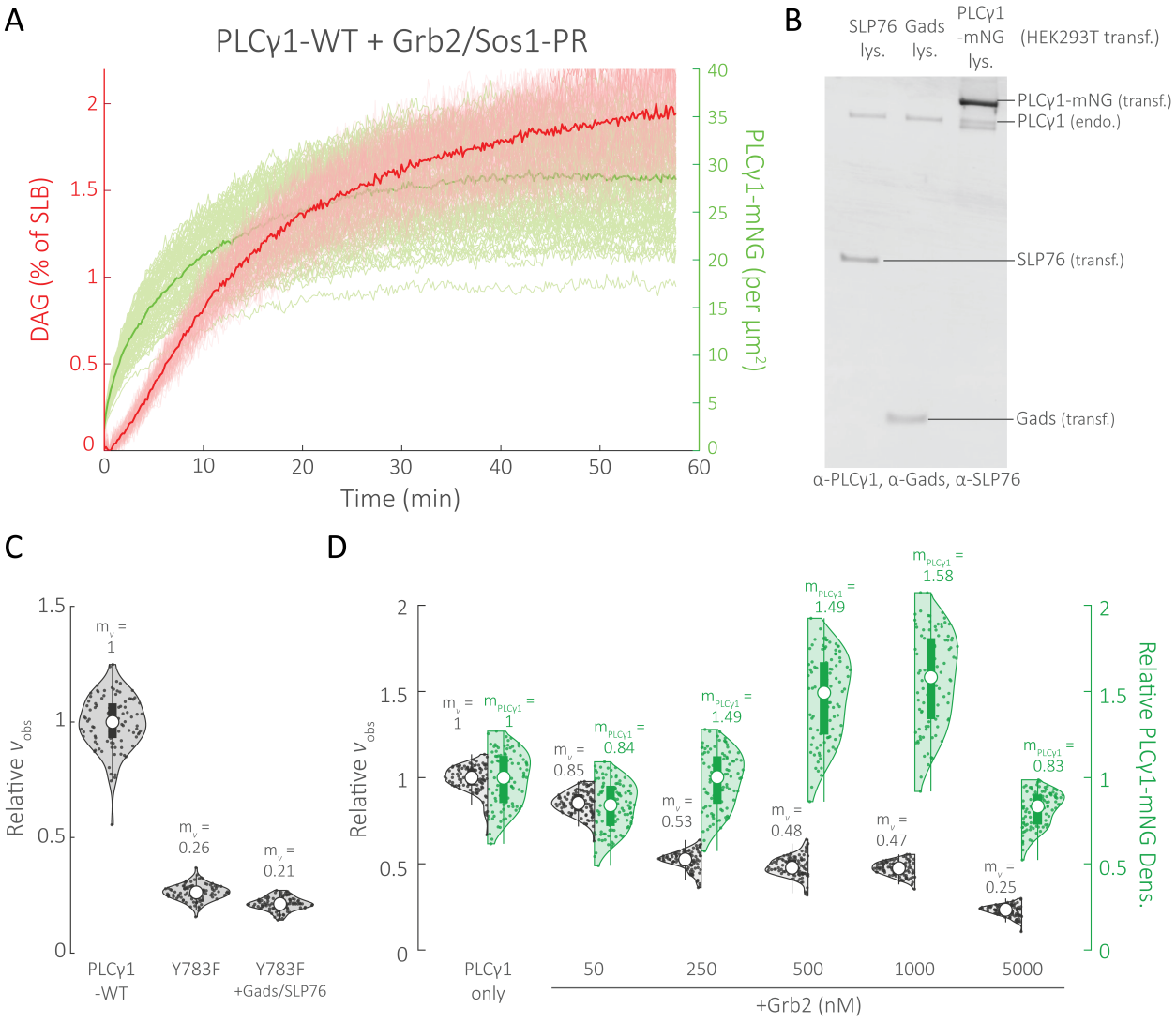


Figure 3.9: Supplementary Figure 3. Validation of the lysate assay with the addition of the LAT:Grb2 condensate.

A. Curves obtained from processing the raw median fluorescence from membrane patches, representing the amount of DAG in the bilayer (red, left axis, top curves) and density of PLCγ1-mNG recruited (green, right axis, bottom curves) over 60 minutes. The production of DAG slows considerably but eventually reaches the maximum possible 2% of the SLB. **B.** Western blot demonstrating the expression of Gads-FL and SLP76-FL in HEK293T cells. Gads and SLP76 containing lysates were used for (**C**) and **Figure 3.5A-B**. **C.** Relative v_{obs} for PLCγ1-WT (with 2 µL of control lysate), for PLCγ1-Y783F mutant (with 2 µL of control lysate), and PLCγ1-Y783F mutant + Gads/SLP76 (1 µL lysate each). Data were normalized to the median value of PLCγ1-WT. There is not a demonstrative difference between the lysate batches, nor does the addition of Gads/SLP76 result in a strong activation of Y783F mutant. **D.** Relative v_{obs} and relative PLCγ1-mNG densities for various conditions, with an increasing amount of purified Grb2. Data were normalized to the median value of the PLCγ1-only condition. Grb2 has been shown to have the ability to crosslink LAT on its own due to dimerization.

Chapter 4

Differential KRas4B diffusion and binding of RBD as a function of PIP2

Joseph B. DeGrandchamp[1], Young Kwang Lee[1], Jay T. Groves[1]

[1]Department of Chemistry, University of California, Berkeley, Berkeley, United States

4.1 Abstract

The activation of Ras, a small membrane-associated GTPase, is an essential step in cellular proliferation pathways, including in T Cells. Ras binds to guanine nucleotides and is activated by enzymes that encourage the exchange of GDP for GTP in the Ras active site. RasGTP then binds to downstream effectors such as Raf1, via its Ras Binding Domain (RBD). This pathway eventually leads to growth signals sent to the cell nucleus. Importantly, Ras exists as several isoforms that are simultaneously expressed but are trafficked and activated in different configurations. A key divergence is in the Hyper-Variable Region (HVR) of Ras linking the lipidated C-terminus to the globular active domain. In particular, the HRas isoform has a neutral HVR, and KRas has a polybasic HVR. The functional consequences of the identity of the HVR are not entirely understood, but there is a high likelihood it affects interactions with the membrane. With Ras signaling being a central paradigm, it is critical to understand novel mechanisms in its configurations and binding to effectors such as Raf1. Therefore, we performed *in vitro* Single Particle Tracking (SPT) experiments to study the diffusion of HRas and KRas on supported bilayers of varying anionic lipid content. Expanding on recent results from the field, we saw that KRas diffusion, but not HRas diffusion, decreased as a function of increasing PIP2 in the bilayer. Furthermore, by tracking the binding dynamics of RBD, we revealed a modest difference in Ras effector binding according to the diffusive state of Ras. This could present an innovative strategy for therapies targeting constitutively active mutants of KRas.

4.2 Introduction

Early MAPK proliferation signals originate at the cell membrane, with a key mediator being the small GTPase Ras [80]. Ras is an incredibly influential small molecule, with mutations resulting in cancer at high occurrences. The intracellular globular G-domain of Ras is loaded with a guanine nucleotide that acts as a molecular switch, with GDP enforcing an inactive state and GTP facilitating a reconfiguration to an active state. RasGTP binds to downstream effectors such as Raf1 kinase, via its Ras Binding Domain (RBD), leading to a cascade of signals ultimately reaching the cell nucleus and resulting in cell growth. This makes constitutively active mutations of Ras particularly dangerous, as they will lead to continuous and malignant growth. The study of Ras configurations and their consequences for effector binding is thus of critical therapeutic interest.

Ras is expressed as an array of isoforms with similar sequences but different functional roles [80-81]. Not all the mechanistic details are known in how these isoforms diverge, but an obvious suspect for the functional discrepancies is the Hyper-Variable Region (HVR) of Ras that connects the lipidated C-terminus of Ras to the G-domain. Two isoforms of interest, HRas and KRas-4B (henceforth, referred to as KRas), are both localized to the plasma membrane. However, the HVR of HRas is largely neutrally charged while that of KRas contains a polylysine region (six directly adjacent lysine residues). This clear variation in these two isoforms leads us to consider the effects of anionic lipids on the interaction of KRas with the membrane, which may contrast with what occurs for HRas. In addition, the KRas G-domain has been suggested to interact directly with PIP2, a lipid with a strong negative charge due to its multi-phosphate headgroup [84]. Perhaps, KRas is either enriched in, excluded from, or exhibits functional differences in certain lipid domains of varying lipid content, in comparison to HRas which may be agnostic to anionic lipids [82-84].

Indeed, a volley of recent research has revealed the dramatic impact of lipid composition on KRas diffusion, through *in vivo* investigation [119], *in vitro* reconstitution of KRas on supported lipid bilayers (SLBs) with complex compositions [86], and through *in silico* modeling [85]. These studies suggested an interaction of KRas with different lipid domains, and we expound on these findings through the use of Single Particle Tracking (SPT) of KRas on SLBs, with a focus on the PIP2 content in the bilayer. We detail the imaging requirements for tracking a quickly diffusing species such as Ras and warn of the dangers of artifacts. After removing imaging anomalies, we found KRas diffusion, but not HRas diffusion, decreased as a function of increasing PIP2 in the bilayer, indicating PIP2 content may play a role in KRas diffusion in various lipid domains. Furthermore, by tracking the binding dynamics of RBD, we revealed a modest difference in Ras effector binding according to the diffusive state of Ras. This could present an innovative strategy for therapies targeting constitutively active mutants of KRas.

4.3 Results and Discussion

After correcting for imaging anomalies, SPT reveals KRas diffusion slows down as a function of PIP2

While not an exact equivalent to the physiological system, functionalizing SLBs with Ras via maleimide coupling is an effective way to study the intracellular domain and its interaction with a fluid bilayer of definite composition. We generated minimally truncated HRas (Fig 4.1A) and KRas (Fig 4.1B) isoforms, maintaining the HVR, and linked them to SLBs with variable anionic content (ie. PIP2). Ras could diffuse laterally in this format, and we loaded it with dilute amounts of the nonhydrolyzable GTP-analog GppNP with a fluorescent label (GppNP-Ax647) allowing us to track Ras via TIRF imaging of the bilayer (Fig 4.1C). We could image a single Ras for seconds at a time, and by programmatically imaging thousands of molecules at different membrane positions, build distributions in order to extract diffusive states. Then, by varying the PIP2 content in the lipid bilayer, we could determine the effect of anionic lipids on HRas and KRas, expecting the polylysine region of KRas to change the resulting observations. However, first, we had to verify the experimental parameters used for tracking and correct for any artifacts.

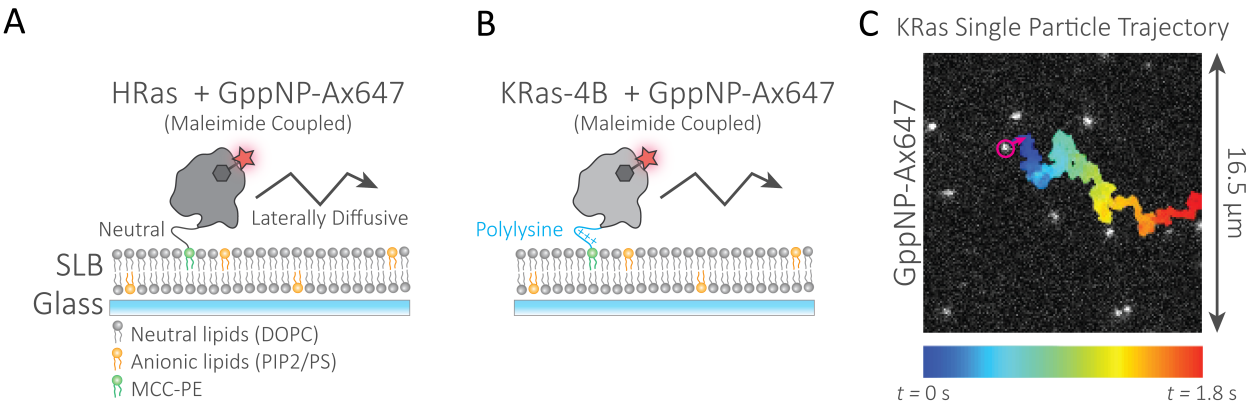


Figure 4.1: HRas and KRas diffusion dynamics can be measured using Single Particle Tracking on Supported Lipid Bilayers of varying composition.

A-B. Schematics summarizing the experimental measurement of Ras diffusion on supported lipid bilayers. HRas (1-C181) (**A**) and KRas-4B (1-C185) (**B**) were coupled to bilayers of varied composition using maleimide coupling to MCC-PE. Laterally diffusive Ras was tracked via TIRF imaging of dilute Ras loaded with GppNP-Alexa647. **C.** A demonstration of a single particle trajectory for KRas (GppNP-Ax647). A single TIRF image (16.5 µm x 16.5 µm) is shown with an overlay denoting the particle starting position (pink circle), direction of motion (pink arrow), and trajectory over 1.8 s (multicolor line). The time of the trajectory is mapped to the colorbar below. All particles in this image were tracked, but only a single trajectory is shown for clarity. Lipid composition (in mol%): 95:4:1 DOPC:PIP2:MCC-DOPE. Total KRas surface density: ~200 μm^{-2}. Exposure time: 7 ms.

We previously validated SPT analysis of Ras on SLBs and determined Ras remained monomeric across numerous bilayer conditions [49]. We were surprised to find that, at the conditions initially used for this study, HRas and KRas both appeared to have two species diffusion after fitting their step-size distributions (Fig 4.2A-B). At first look, we attributed this to different modes of Ras interaction with the bilayer resulting in anomalous diffusion. The calculated population of the fast and slow state (α) also changed when varying the PIP2 content of the bilayer, and there appeared to be differences in how this affected HRas and KRas. We spent a good deal of time trying to characterize these species and their change with lipid composition. But after much deliberation and many careful controls, we eventually concluded this observed two-species diffusion was, in fact, artifactual.

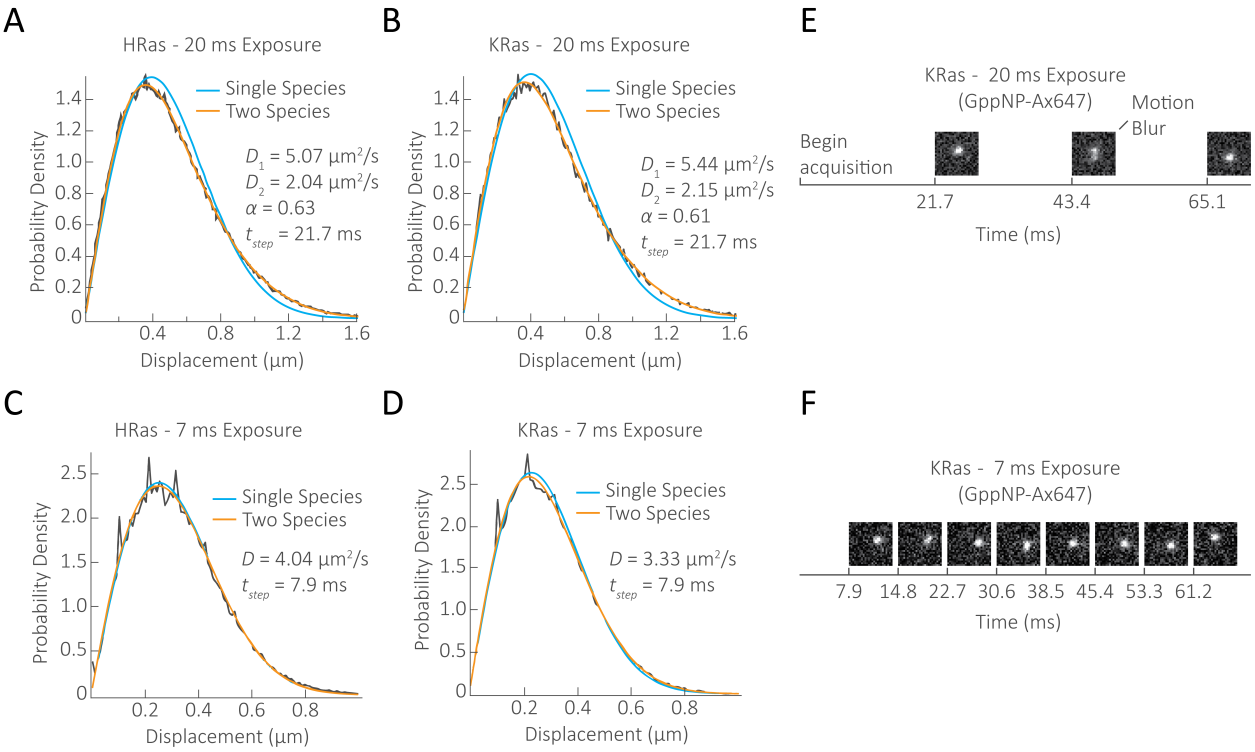


Figure 4.2: Ras diffusion remains single species after correcting for observed erron-eous two-species dynamics from motion blur artifacts.

A-B. Step-size distributions for HRas (**A**) and KRas (**B**) from SPT of GppNP-Ax647 on a 0.5% PIP2 bilayer with a 20 ms exposure time for measurement by an EMCCD camera. The true distribution is shown as a grey line in the background. Fits to single-species and two-species models of diffusion are shown overlayed (light blue and gold lines respectively). Coefficients resulting from the two species fitting are shown (D_1, D_2 – diffusion coefficients of the fast and slow species, respectively, α - fraction of the fast species). The step size (t_{step}) was 21.7 ms, 1.7 ms longer than the exposure time due to the read time of the camera. Lipid composition (in mol%): 98.5:0.5:1 DOPC:PIP2:MCC-DOPE. Total Ras surface density: ~200 μm^{-2}. Total tracks acquired: >10,000 for each condition. **C-D.** Step-size distributions for HRas (**C**) and KRas (**D**) from SPT of GppNP-Ax647 with a 7 ms exposure time. The display of distributions/fits, lipid composition, and Ras density are the same as those in (**A,B**). Coefficients resulting from the single species fitting are shown (D – diffusion coefficient). The step size (t_{step}) was 7.9 ms, 0.9 ms longer than the exposure time due to the read time of the camera. **E-F.**

TIRF images (2.5 μm x 2.5 μm) of single particles (KRas GppNP-Ax647) are showing at subsequent time points for 20 ms (**E**) or 7 ms (**F**) exposures. The left side of the time axis (below the images) denotes the true start of the acquisition. The ticks of the time axis denote the true time the corresponding image (to the right) was fully acquired and stored. The time axes in (**E**) and (**F**) are equivalent. The third frame of (**E**) is denoted as being indicative of motion blur.

Our initial methodology utilized the full field of view (FOV) of our EMCCD of 512 x 512 pixels, which due to the nature of CCD technology, limited our effective exposure time to a minimum of ~20 ms. This may sound like an appropriately short timestep and does indeed suffice for many more slowly-diffusing molecules [120]. Ras in our experiments, however, could (conditionally) diffuse as fast as MCC-DOPE (ie. a single lipid species) at speeds up to ~4 $\mu m^2/s$ (Fig 4.2C) [121]. At these speeds, Ras can stochastically diffuse large enough distances in 20 ms (>1 μm) that it introduces motion blur into the image, smearing the particle across multiple pixels (Fig 4.2E). We found this was sufficient to cause systematic errors in our tracking algorithms. Motion blurring artifacts have been well-described in the last few years using computationally-generated SPT experiments [122]. A blurring coefficient (δ_{blur}) was mathematically defined as a function of the particle's diffusion (D), exposure time (t_E), emission wavelength (λ), and the objective's numerical aperture (NA) such that

$$\delta_{blur} \approx \sqrt{\frac{Dt_E}{3}\left(\frac{NA}{0.21\lambda}\right)^2} \qquad (1).$$

In our system, δ_{blur} at 20 ms exposure is ~1.66 (0.5 was described as "weak blur" and was a desirable target [121]). To achieve shorter exposure times and thus smaller δ_{blur}, we employed a "cropping mode" feature on our EMCCD to reduce our effective FOV to 150 x 150 pixels. The smaller FOV lead to shorter read times for the camera and shortened the lowest possible exposure time to ~7 ms. Imaging at this shorter exposure time, while not achieving "weak blur", would reduce δ_{blur} by close to 60% to ~0.98. We found this reduction in exposure time resulted in our observed Ras step-size distributions collapsing to single species fits (Fig 4.2C-D) and to the abrogation of visible blurring in images (Fig 4.2F). While it reduced the trackable number of particles per image, experiments were simply lengthened appropriately to achieve similar numbers of tracked particles. Future studies could perhaps utilize the recent advances in "stroboscopic" illumination, where the on-time of the excitation laser is shortened instead of modulating the exposure time of the camera [123-125]. However, for the purposes of this analysis, shortened exposure times were sufficient, and with this realization behind us, we moved onward to the measurement of Ras diffusion as a function of bilayer composition.

On a 0.5% PIP2 bilayer, we already see differences in KRas and HRas diffusion, with KRas being 20% (~0.7 $\mu m^2/s$) slower (Fig 4.3A-C). At increasing PIP2, this difference becomes more pronounced, with KRas diffusion slowing down to 2.55 $\mu m^2/s$ while HRas remains (within error) at its initial diffusion of ~4 $\mu m^2/s$ (Fig 4.3 C). This suggests the polylysine region of KRas near the membrane (Fig 4.1B)—the existence of which is the major difference between HRas and KRas—plays a role in modulating KRas diffusion. But is where the story ends? This difference in diffusion suggests varying engagement of KRas with the bilayer

which would likely affect downstream effectors, and with that in mind, we developed a platform for SPT of a repurposed Ras-activity sensor.

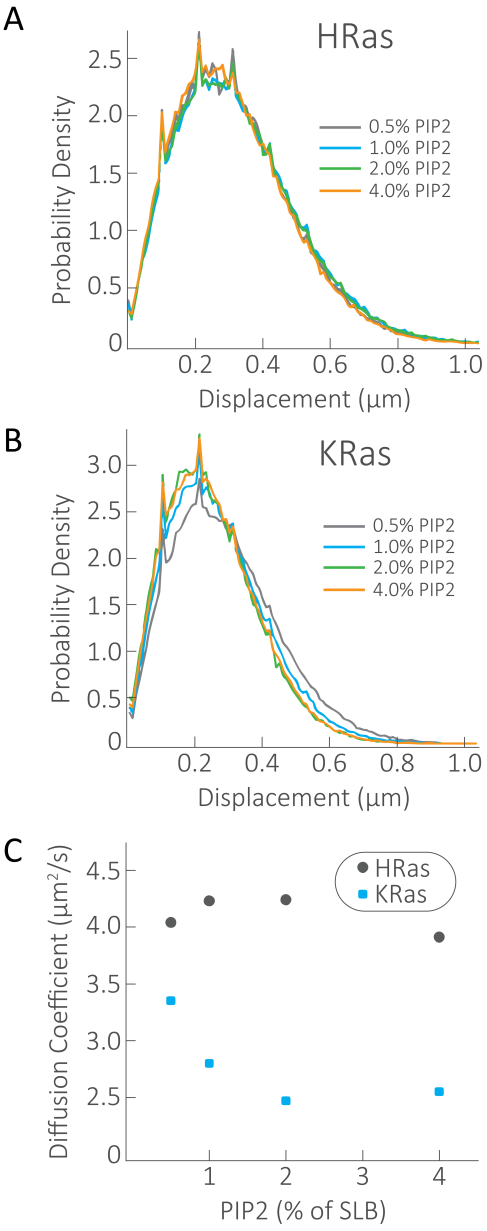


Figure 4.3: KRas, but not HRas, diffusion becomes slower as a function of PIP2 in the bilayer.

A-B. Step-size distributions for HRas (**A**) and KRas (**B**) from SPT of GppNP-Ax647 on bilayers with varying PIP2 content. Distributions at 0.5 mol%, 1.0 mol%, 2.0 mol%, and 4.0 mol% of PIP2 are shown (grey, blue, green, and gold respectively). Step size: 7.9 ms. Lipid composition (in mol%): 95-98.5:0.5-4:1 DOPC:PIP2:MCC-DOPE. Total Ras surface density: ~200 μm^{-2}. Exposure time: 7 ms. Total tracks acquired: >10,000 for each condition. **B.** A scatter plot summarizing diffusion coefficients extracted from fittings of a single species model to distributions in (**A,B**). Coefficients are shown as function of mol% of PIP2 in the bilayer with HRas denoted as grey circles and KRas as light blue squares.

Tracking of bound RBD reveals differences in binding kinetics depending on diffusive state of Ras

To study the effect of Ras diffusion on its downstream binding partners, we utilized a well-characterized construct in our lab, the Ras Binding Domain (RBD) of Raf1 [29, 57]. RBD preferentially binds the active (GTP-bound) state of Ras, and we have used it successfully as a readout for Ras nucleotide exchange activity by Sos1. Herein, we instead track the binding and diffusion kinetics of RBD itself (via a SNAPtag proxy labeled with Alexa 647) to determine whether the differential diffusion of KRas versus HRas has measurable functional consequences (Fig 4.4A). RBD binds transiently to active Ras, and we were successful in measuring both rare, longer events (Fig 4.4B, pink circle) and short events (Fig 4.4B, pink square), allowing us to measure the full range of RBD kinetics.

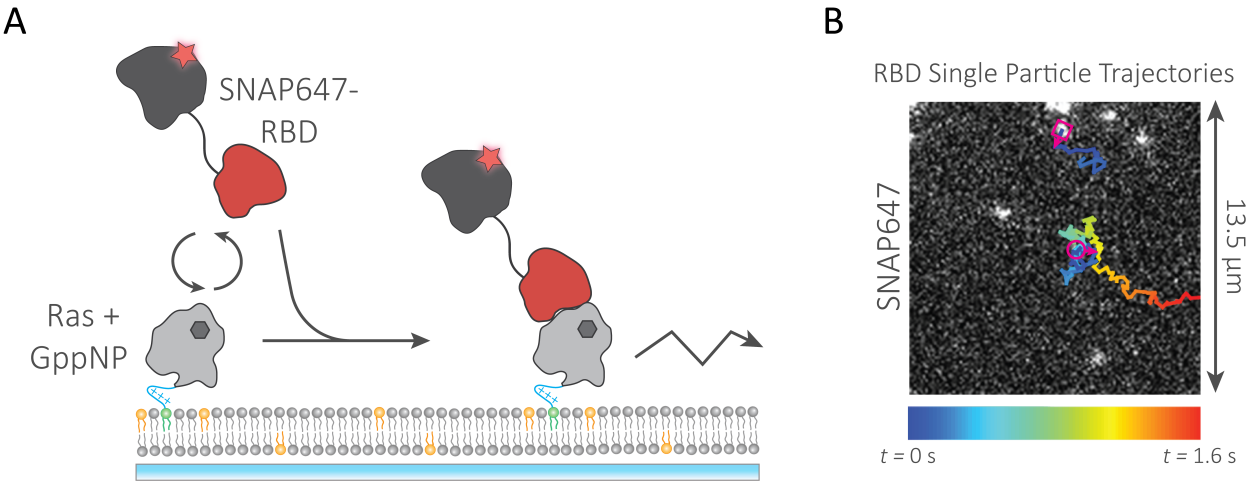


Figure 4.4: RBD can be tracked after binding to GppNP-loaded Ras via SNAP647 imaging.
A. Schematic summarizing the experimental measurement of RBD diffusion after binding to Ras-GppNP on supported lipid bilayers. Dilute concentrations of SNAP647-RBD(K65E) were flowed over Ras functionalized bilayers loaded with GppNP (dark). RBD binds reversibly to Ras but in a time frame long enough to capture using TIRF imaging. RBD diffuses along with Ras at approximately the same rate. **B.** A demonstration of a single particle trajectory for RBD (SNAP647) bound to KRas-GppNP. A single TIRF image (13.5 μm x 13.5 μm) is shown with two overlays denoting particle starting positions for a short binding event (pink square) and a long binding event (circle). The direction of motion (pink arrows), and trajectories over 1.6 s (multicolor lines) are also shown. The time of the trajectories is mapped to the colorbar below. All particles in this image were tracked, but only a single short trajectory and a single long trajectory are shown for clarity. Lipid composition (in mol%): 95:4:1 DOPC:PIP2:MCC-DOPE. Total KRas surface density: ~200 μm^{-2}. Exposure time: ~10 ms. SNAP647-RBD concentration: ~200 pM (11.5% labeled).

Since our SPT of Ras and partner RBD both shared the same imaging channel, we did not measure their diffusion simultaneously. Through sequential back-to-back measurements of neighboring fluidic channels, we were able to show RBD diffusion tracked closely with that of both isoforms of Ras and across PIP2 concentrations (Fig 4.5A-B). The biggest difference is between RBD and KRas on a 0.5% PIP2 bilayer (Fig 4.5B), with RBD appearing to be close to 10% slower (in this experiment: $D_{\text{RBD, 0.5\%PIP2}}$ = 2.82 μm²/s, $D_{\text{KRas, 0.5\%PIP2}}$ = 3.02 μm²/s). This is likely due to minute differences in initial bilayer mobility between the channels of our chamber, rather than anything mechanistic. Regardless, RBD and KRas diffusion both slow down to ~1.7 μm²/s (Fig 4.5B). We were, therefore, confident we were measuring RBD bound to Ras (rather than non-specific events).

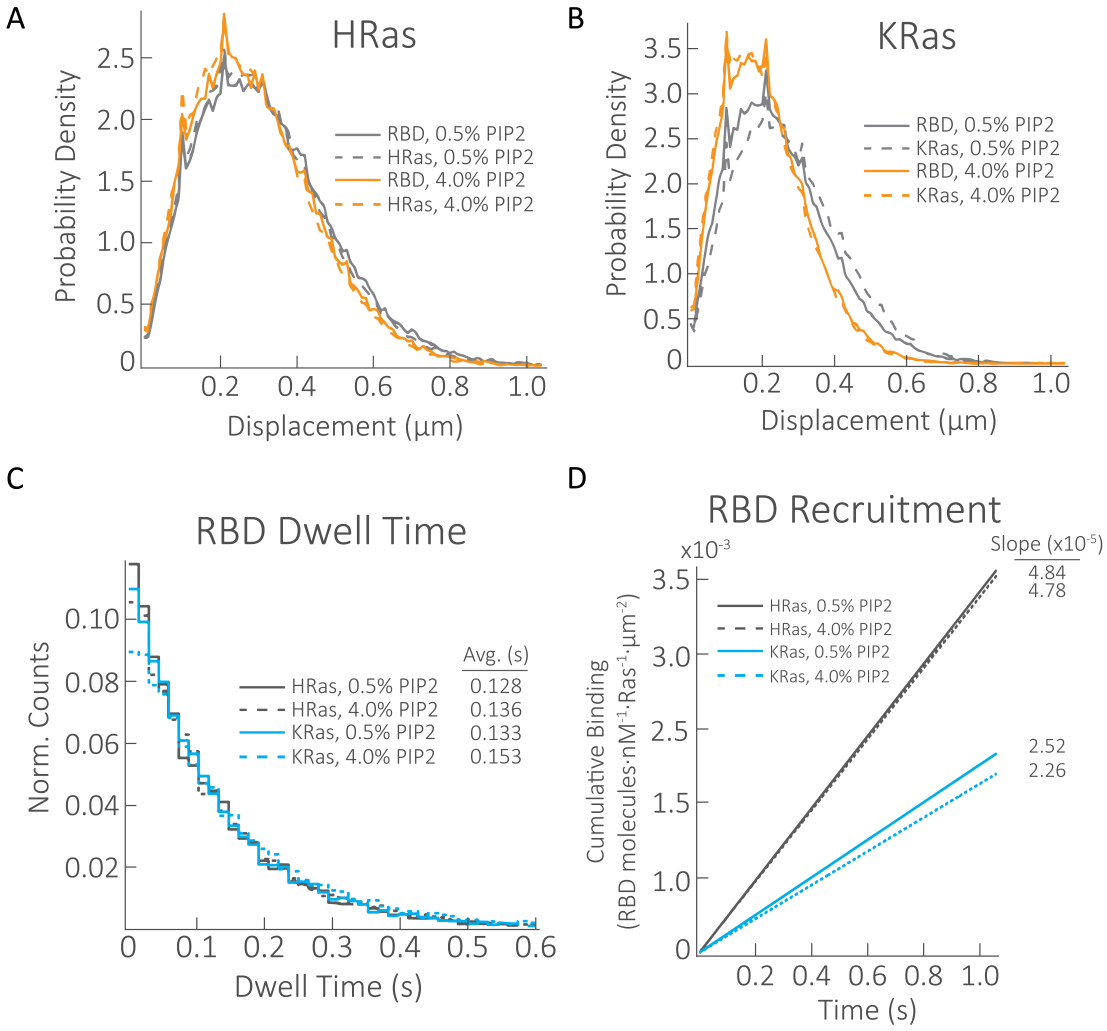


Figure 4.5: RBD diffusion follows Ras diffusion, while RBD dwell time and recruitment are affected by the diffusive state of Ras.

A-B. Step-size distributions for HRas (**A**) and KRas (**B**) functionalized bilayers with varying PIP2 content from SPT of SNAP647-RBD and GppNP-Ax647 (in separate, side-by-side channels). Distributions at 0.5 mol% and 4.0 mol% of PIP2 are shown via grey and gold lines respectively.

Distributions for RBD and Ras are shown as solid and dashed lines respectively. Step size: ~7.9 ms (FOV: 150x150 pixels). Lipid composition (in mol%): 95-98.5:0.5-4:1 DOPC:PIP2:MCC-DOPE. Total Ras surface density: ~200 μm^{-2}. Exposure time: 10 ms. SNAP647-RBD concentration: ~200 pM (11.5% labeled). Total tracks acquired: >10,000 for each condition. **C.** Dwell time histogram for SNAP647-RBD. Distributions at 0.5 mol% and 4.0 mol% of PIP2 are shown via solid and dashed lines respectively. Distributions for HRas and KRas are shown as light grey and blue lines respectively. Average dwell times for each distribution (in s) are shown in the inset. Lipid composition and densities/concentrations are the same as those in (**A,B**). FOV: 256 x 256 pixels. **D.** Cumulative binding plot for SNAP647-RBD. Recruitment for 0.5 mol% and 4.0 mol% of PIP2 is shown via solid and dashed lines respectively. Recruitment for HRas and KRas is shown as light grey and blue lines respectively. Slopes of each recruitment profile, corresponding to binding frequency, are shown to the right of the plot (units: molecules·nM^{-1}·um^{-2}·s^{-1}). Lipid composition and densities/concentrations are the same as those in (**A,B**). FOV: 256 x 256 pixels.

Any effect on RBD binding to Ras is most prominently going to appear in its recruitment and/or binding lifetime to Ras. Thus, we measured the dwell time and cumulative binding of RBD to Ras for the various conditions (Fig 4.5 C-D). Since the positional accuracy of particles for these measurements is less critical, we increased our camera's FOV to 256 x 256 pixels, allowing for the acquisition of many more binding events in the same time frame. We found that RBD dwell time and cumulative binding for HRas bilayers changed very little as a function of PIP2, while KRas bilayers showed a modest decrease in both when PIP2 was increased (Fig 4.5 C-D). This indicates a negative effect, however small, of PIP2 on the ability of KRas to bind to RBD.

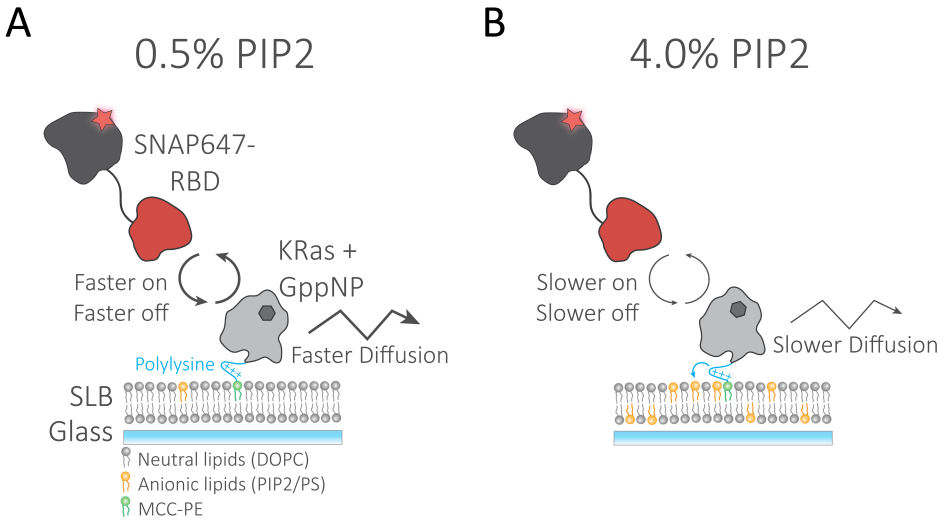


Figure 4.6: Ras effectors may be affected by changes in Ras-bilayer interactions related to bilayer composition.

A-B. Schematics summarizing the experimental results of measuring Ras diffusion and RBD binding dynamics on supported lipid bilayers. KRas-4B is faster on low PIP2 bilayers (**A**) and slower on bilayers with higher PIP2 content (**B**). Changes in diffusion map to changes in RBD recruitment and dwell time.

4.4 Conclusion

Ras, being a critical mediator of cellular proliferation across a multitude of cell lines, is of the utmost importance for study. We demonstrated above a simple yet effective methodology for the measurement of Ras and Ras-effector kinetics, with the ability to determine the effects of bilayer composition on these parameters. We used our supported bilayer platform and SPT via TIRF microscopy to expound on recent findings [85-86, 119] on the differential diffusion of KRas with respect to bilayer composition, determining PIP2 content in the bilayer to be a critical factor. Furthermore, we moved downstream and revealed a potential functional change in KRas according to its diffusive state. We found modest changes in the binding of RBD, a stand-in for Ras effectors (Fig 4.6). This could potentiate future therapeutic discoveries for constitutively active Ras mutations.

4.5 Experimental Methods

Protein purifications

All purified constructs utilized pET28a (Novagen-Cat. # 69864-3) or pETM (similar to Addgene #108943) backbones under the T7 promoter for expression in *E. Coli*. Expression vectors were transformed into BL21-CodonPlus competent *E. Coli* (Agilent) and cultured in TB. T7 expression was induced using 2 mM IPTG (final concentration) (Gold Biotechnology) overnight (18-20 hrs) at 18 °C with shaking. Pelleted cells were resuspended in bacterial lysis buffer typically containing 75 mM NaH_2PO_4 pH 8.0, 300-700 mM NaCl, 2 mM beta-mercaptoethanol (BME) (Sigma Aldrich), DNAse (Sigma Aldrich), 5-10 mM imidazole (Fisher Scientific), and 1-2 tablets of EDTA-free Pierce Protease Inhibitor Cocktail (A32965, ThermoFisher Scientific). All subsequent steps were done at 4 °C. Bacteria were lysed using an EmulsiFlex-C3 high-pressure homogenizer (Avestin). Subsequent steps are described for each protein below, with proteins generally stored at -80 °C in 20 mM Tris-HCl pH 7.4, 200 mM NaCl, 1 mM TCEP (Sigma Aldrich), and 10% glycerol (MCB grade, Fisher Scientific) after a final SEC polishing step (Superdex 75 or 200 column, 120 mL bed volume, Cytiva) and flash-freezing in liquid N_2.

HRas (1-181 aa, human), with the mutation C118S (leaving only C181 as a solvent-exposed cysteine), was expressed with a cleavable (TEV) N-terminal His6-tag and purified as described previously [120]. The N-terminal His6-tag was removed by TEV before use.

KRas-4B (1-185 aa, human), also with the mutation C118S (leaving only C185 as a solvent-exposed cysteine), was expressed and purified identically to HRas.

SNAPtag-Raf1 RBD(K65E) (56-131 aa, human) was expressed with a cleavable (PreScission) N-terminal His6-GST fusion protein and purified as described previously [29]. The N-terminal His6-GST was removed by PreScission before use. The protein was labeled with

SNAP-Surface Alexa 647 (S9136S, New England Biolabs) according to the manufacturer protocol, with the removal of excess dye by gravity desalting columns (PD10, Cytiva) and further by SEC via FPLC (Superdex 75 increase, 24 mL bed volume, Cytiva).

SUV and SLB preparation

Small unilamellar vesicles (SUVs) were made using 1,2-dioleoyl-sn-glycero-3-phosphocholine (DOPC), 1,2-dioleoyl-sn-glycero-3-phosphoethanolamine-N-[4-(p-maleimidomethyl)cyclohexane-carboxamide] (sodium salt) (MCC-PE), and L-α-phosphatidylinositol-4,5-bisphosphate (Brain, Porcine) (ammonium salt) (Brain PIP2) (Avanti Polar Lipids). Lipids were purchased, stored (-20 °C), and mixed solubilized in chloroform. Lipids were mixed in an etched round bottom flask to yield 2 mg total lipid mass at a ratio of 95-98.5:1:0.5-4 (mol%) DOPC:MCC-PE:PIP2. After mixing well, lipids were dried by rotovap in a 37 °C water bath, kept under vacuum to dry an additional 10 min at room temperature, then dried under continuous N_2 gas flow for >30 min. Lipid films were solubilized with 2 mL milli-Q water (to yield 1 mg/mL lipid concentration) and vigorously vortexed to ensure film liftoff. The cloudy aqueous lipid mixture was added to a 5 mL polypropylene tube and treated by 3 mm stepped tip sonication (Sonics VCX750 – 33% amplitude, 20 s sonication, 50 s rest, 5 cycles) while submerged in ice. The clarified SUV solution was then centrifuged at 20,000 g for 20 min to remove tip debris and any remaining large vesicles. The supernatant was stored at 4 °C in a sealed tube for use in experiments up to ~1 week.

Precision Schott D 263 M glass coverslips (#1.5H, 75 x 25 mm, custom ordered from ThorLabs, similar to Part# CG15CH) were first cleaned with warm 2% Hellmanex III (Fisher Scientific) solution with bath sonication at 45 °C for 30 min, then 50% IPA:mill-Q with sonication for >15 min, then milli-Q with sonication for >15 min. Substrates were then etched using a 1:3 ratio of concentrated H_2SO_4 to 30% H_2O_2 (piranha etch) for 3 min (while still warm). Substrates were rinsed excessively with milli-Q water between each cleaning step and after etching. Substrates were stored in milli-Q at room temperature for use in experiments up to ~1 week. To build chambers for experiments, etched substrates were blow-dried under N_2 and attached to simple 6-channel flow cells (sticky-Slide VI 0.4, ibidi). Chambers were cured at 37 °C for >10 min while pressed under a heavy weight. After curing, chambers were allowed to cool to room temperature for >10 min.

Supported lipid bilayers were formed via vesicle rupture the day before imaging. The 1 mg/mL SUV solution was diluted to 0.25 mg/mL in degassed 1X PBS. 100 µL of 0.25 mg/mL SUV (0.75X PBS) was added per chamber channel and incubated for >30 min at room temperature. Channels were washed via 1 mL degassed 1X PBS. SLBs were then blocked with 1 mg/mL casein solution (Blocker Casein, Thermo Scientific) diluted in 1X PBS for 10 min. HRasC181 and KRasC185 were thawed, diluted in 1X PBS to 0.5 mg/mL, and incubated for 1.5 hrs (yields ~200 μm^{-2} Ras density). Channels were washed with 1 mL 1X PBS, then MCC-PE was quenched with 10 mM BME in 1X PBS for 10 min. Channels were exchanged to 1X HBS (30 mM HEPES, 250 mM NaCl), then incubated with 50 mM EDTA in 1X HBS for 5 min

(2 times) to strip any nucleotides bound to Ras. Channels were exchanged to reaction buffer (30 mM HEPES, 250 mM NaCl, 1 mM $MgCl_2$), then incubated overnight at 4 °C with 1 μM of Atto488-GppNp in reaction buffer.

Imaging Hardware and Acquisition

TIRF imaging experiments were performed on an inverted Nikon Eclipse Ti microscope using a 100X Nikon oil-immersion TIRF objective (1.49 NA). We used a 1.5X lens tube (Nikon) before the camera for a total 150X magnification. Stage movement and automatic repositioning were done using a motor-controlled stage (MS-2000, ASI). Images were acquired with an iXon Ultra 897 EMCCD camera (Andor Technology). Fluorescently labeled proteins were excited with either a 488- or 637-nm diode laser (OBIS laser diode; Coherent) controlled with a custom laser driver (Solamere Technology) using TTL signals from the camera. Lasers were collimated with the objective position at the approximate sample z-focus before every experiment. A single quad-band dichroic cube was used for all acquisitions (ZT405/488/561/640rpcv2, Chroma). Fluorescence emission was additionally filtered by: ET525/50M (488 excitation) or ET700/75M (637 excitation) (Semrock). Microscope and accessory hardware was controlled using Micro-Manager, version 4.0 [109]. Experiments were conducted at 21-23 °C. Excitation conditions for each channel during background collection and kinetic measurements were as follows: Atto488-GppNp-loaded Ras was excited at 488 nm (~0.45 mW at the objective); Ax647-GppNp-loaded Ras and SNAP647-RBD were excited at 637 nm (~20 mW at the objective). Atto488-GppNp-loaded Ras images were acquired with a 20 ms camera exposure and 500 EM gain, and 20-30 images at varying positions were collected for background measurement. Image sequences for SPT (637 channel) were acquired at the fastest camera exposure possible (150x150 px: 7 ms, 256x256 px: 10 ms, 512x512 px: 20 ms) with frame transfer enabled (camera feature to increase framerate) and 1000 EM gain. Cropped imaging areas were achieved using the "ROI Cropping Mode" of the Andor EMCCD. The hexagonal field stop of the microscope was centered and closed around the cropped area in order to reduce unnecessary illumination of the bilayer outside the FOV. Image visualization and corrections were done in FIJI [117].

SPT experiments and Ras density measurements

All single particle tracking (SPT) measurements were performed using imaging buffer containing 1X HBS, 1 mM $MgCl_2$, 10 mM BME, 5 μM GppNP, 2 mM Trolox (UV treated), 0.32 mg/mL glucose oxidase (22778.01, Biophoretics), 0.05 mg/mL catalase (C40-100MG, Sigma Aldrich), 20 mM D-glucose (Fisher Scientific), and 0.1 mg/mL casein (final concentrations after addition of analytes). Trolox (Sigma Aldrich) was prepared as previously described [110]. Excess Atto488-GppNp from overnight incubation was first washed out with 1 mL of reaction buffer (see bilayer preparation). 100 μL of 5 μM GppNP (unlabeled) in reaction buffer was immediately added, and Atto488-GppNp images (20-30 at various non-overlapping positions) were acquired in quick succession for total Ras density measurements. Densities of Ras were estimated by establishing a calibration curve between TIRF average intensity and densities measured by fluorescence correlation spectroscopy

(FCS) (described previously [120]). The FOV was adjusted using cropping mode to 150 x 150 pixels (diffusion measurements) or 256 x 256 pixels (dwell time/recruitment measurements). A 10 x 10 grid of bilayer positions (FOVs) was mapped out using Micro-Manager with offsets of at least 80 μm, such that each bilayer section imaged would not be likely to exchange molecules [109]. 3 nM of Ax647-GppNp in imaging buffer (100 μL total) was added, and a streaming acquisition (shortest possible exposure time) was started immediately such that 1000 frames were programmatically acquired at each grid position. The first 200 frames at each position were removed using a custom FIJI script [117] to remove fast-bleaching fluorescent contamination. The script then stitched together the remaining 800 frames for each position with 5 blank images in between each subset (such that molecules from different positions could not mistakenly be joined as a single tracked particle). The TrackMate plugin of FIJI [118] was then used to build single particle tracks from the complete dataset, with a max gap of 1 frame between particle tracks. Tracks were filtered by a minimal mean velocity such that any remaining immobile particles were removed from the analysis. Track analysis and fitting were done in Igor Pro (WaveMetrics) as previously described [49].

References

(1) Bona, C. A. & Bonilla, F. A. *Textbook of Immunology*. (CRC Press, 2019).

(2) Rudolph, M. G., Stanfield, R. L. & Wilson, I. A. How TCRs bind MHCs, peptides, and coreceptors. *Annu Rev Immunol* **24**, 419-466 (2006).

(3) Davis, M. M., Boniface, J. J., Reich, Z., Lyons, D., Hampl, J., Arden, B. & Chien, Y. Ligand recognition by alpha beta T cell receptors. *Annu Rev Immunol* **16**, 523-544 (1998).

(4) Maroun, C. R. & Julius, M. Distinct roles for CD4 and CD8 as co-receptors in T cell receptor signaling. *Eur J Immunol* **24**, 959-966 (1994).

(5) T. W. McKeithan, Kinetic proofreading in T-cell receptor signal transduction. Proc. Natl. Acad. Sci. U. S. A. 92, 5042–5046 (1995).

(6) Ganti, R. S., Lo, W.-L., McAffee, D. B., Groves, J. T., Weiss, A. & Chakraborty, A. K. How the T cell signaling network processes information to discriminate between self and agonist ligands. *Proceedings of the National Academy of Sciences* **117**, 26020-26030 (2020).

(7) Tischer, D. K. & Weiner, O. D. Light-based tuning of ligand half-life supports kinetic proofreading model of T cell signaling. *eLife* **8**, e42498 (2019).

(8) Britain, D. M., Town, J. P. & Weiner, O. D. Progressive enhancement of kinetic proofreading in T cell antigen discrimination from receptor activation to DAG generation. *eLife* **11**, e75263 (2022).

(9) Courtney, A. H., Lo, W.-L. & Weiss, A. TCR Signaling: Mechanisms of Initiation and Propagation. *Trends in Biochemical Sciences* **43**, 108-123 (2018).

(10) Huang, J., Brameshuber, M., Zeng, X., Xie, J., Li, Q. J., Chien, Y. H., Valitutti, S. & Davis, M. M. A single peptide-major histocompatibility complex ligand triggers digital cytokine secretion in CD4(+) T cells. *Immunity* **39**, 846-857 (2013).

(11) Sykulev, Y., Joo, M., Vturina, I., Tsomides, T. J. & Eisen, H. N. Evidence that a single peptide-MHC complex on a target cell can elicit a cytolytic T cell response. *Immunity* **4**, 565-571 (1996).

(12) Lin, J. J. Y., Low-Nam, S. T., Alfieri, K. N., McAffee, D. B., Fay, N. C. & Groves, J. T. Mapping the stochastic sequence of individual ligand-receptor binding events to cellular activation: T cells act on the rare events. *Science Signaling* **12**, eaat8715 (2019).

(13) Chakraborty, A. K., Weiss, A. Insights into the initiation of TCR signaling. *Nature Immunology* **15**, 798–807 (2014).

(14) Iwashima, M., Irving, B., van Oers, N., Chan, A., Weiss, A. Sequential interactions of the TCR with two distinct cytoplasmic tyrosine kinases. *Science* **263**, 1136–1139 (1994).

(15) Stepanek, O., Prabhakar, Arvind S., Osswald, C., King, Carolyn G., Bulek, A., Naeher, D., Beaufils-Hugot, M., Abanto, Michael L., Galati, V., Hausmann, B., Lang, R., Cole, David K., Huseby, Eric S., Sewell, Andrew K., Chakraborty, Arup K. & Palmer, E. Coreceptor Scanning by the T Cell Receptor Provides a Mechanism for T Cell Tolerance. *Cell* **159**, 333-345 (2014).

(16) Zhou, S., Shoelson, S. E., Chaudhuri, M., Gish, G., Pawson, T., Haser, W. G., King, F., Roberts, T., Ratnofsky, S., Lechleider, R. J., Neel, B. G., Birge, R. B., Fajardo, J. E., Chou, M. M., Hanafusa, H., Schaffhausen, B. & Cantley, L. C. SH2 domains recognize specific phosphopeptide sequences. *Cell* **72**, 767-778 (1993).

(17) Liu, B. A., Engelmann, B. W. & Nash, P. D. The language of SH2 domain interactions defines phosphotyrosine-mediated signal transduction. *FEBS Letters* **586**, 2597-2605 (2012).

(18) Deindl, S., Kadlecek, T. A., Brdicka, T., Cao, X., Weiss, A. & Kuriyan, J. Structural basis for the inhibition of tyrosine kinase activity of ZAP-70. *Cell* **129**, 735-746 (2007).

(19) Wang, H., Kadlecek, T. A., Au-Yeung, B. B., Goodfellow, H. E., Hsu, L. Y., Freedman, T. S. & Weiss, A. ZAP-70: an essential kinase in T-cell signaling. *Cold Spring Harb Perspect Biol* **2**, a002279 (2010).

(20) Thill, P. A., Weiss, A. & Chakraborty, A. K. Phosphorylation of a Tyrosine Residue on Zap70 by Lck and Its Subsequent Binding via an SH2 Domain May Be a Key Gatekeeper of T Cell Receptor Signaling In Vivo. *Molecular and Cellular Biology* **36**, 2396-2402 (2016).

(21) Zhang, W., Sloan-Lancaster, J., Kitchen, J., Trible, R. P. & Samelson, L. E. LAT: the ZAP-70 tyrosine kinase substrate that links T cell receptor to cellular activation. *Cell* **92**, 83-92 (1998).

(22) Lin, J. & Weiss, A. Identification of the minimal tyrosine residues required for linker for activation of T cell function. *J Biol Chem* **276**, 29588-29595 (2001).

(23) Zhu, M., Janssen, E. & Zhang, W. Minimal requirement of tyrosine residues of linker for activation of T cells in TCR signaling and thymocyte development. *J Immunol* **170**, 325-333 (2003).

(24) Zhang, W., Trible, R. P., Zhu, M., Liu, S. K., McGlade, C. J. & Samelson, L. E. Association of Grb2, Gads, and phospholipase C-gamma 1 with phosphorylated LAT tyrosine residues. Effect of LAT tyrosine mutations on T cell angigen receptor-mediated signaling. *J Biol Chem* **275**, 23355-23361 (2000).

(25) Houtman, J. C. D., Yamaguchi, H., Barda-Saad, M., Braiman, A., Bowden, B., Appella, E., Schuck, P. & Samelson, L. E. Oligomerization of signaling complexes by the multipoint binding of GRB2 to both LAT and SOS1. *Nature Structural & Molecular Biology* **13**, 798-805 (2006).

(26) Balagopalan, L., Kortum, R. L., Coussens, N. P., Barr, V. A. & Samelson, L. E. The linker for activation of T cells (LAT) signaling hub: from signaling complexes to microclusters. *J Biol Chem*

(27) Su, X., Ditlev, J. A., Hui, E., Xing, W., Banjade, S., Okrut, J., King, D. S., Taunton, J., Rosen, M. K. & Vale, R. D. Phase separation of signaling molecules promotes T cell receptor signal transduction. *Science* **352**, 595-599 (2016).

(28) Huang, W. Y. C., Yan, Q., Lin, W.-C., Chung, J. K., Hansen, S. D., Christensen, S. M., Tu, H.-L., Kuriyan, J. & Groves, J. T. Phosphotyrosine-mediated LAT assembly on membranes drives kinetic bifurcation in recruitment dynamics of the Ras activator SOS. *Proceedings of the National Academy of Sciences* **113**, 8218-8223 (2016).

(29) Huang, W. Y. C., Alvarez, S., Kondo, Y., Lee, Y. K., Chung, J. K., Lam, H. Y. M., Biswas, K. H., Kuriyan, J. & Groves, J. T. A molecular assembly phase transition and kinetic proofreading modulate Ras activation by SOS. *Science* **363**, 1098-1103 (2019).

(30) Sun, S., GrandPre, T., Limmer, D. T. & Groves, J. T. Kinetic frustration by limited bond availability controls the LAT protein condensation phase transition on membranes. *Science Advances* **8**, eabo5295 (2022).

(31) McAffee, D. B., O'Dair, M. K., Lin, J. J., Low-Nam, S. T., Wilhelm, K. B., Kim, S., Morita, S. & Groves, J. T. Discrete LAT condensates encode antigen information from single pMHC:TCR binding events. *Nature Communications* **13**, 7446 (2022).

(32) Boriack-Sjodin, P. A., Margarit, S. M., Bar-Sagi, D. & Kuriyan, J. The structural basis of the activation of Ras by Sos. *Nature* **394**, 337-343 (1998).

(33) Cherfils, J. & Zeghouf, M. Regulation of small GTPases by GEFs, GAPs, and GDIs. *Physiol Rev* **93**, 269-309 (2013).

(34) Jeng, H. H., Taylor, L. J. & Bar-Sagi, D. Sos-mediated cross-activation of wild-type Ras by oncogenic Ras is essential for tumorigenesis. *Nat Commun* **3**, 1168 (2012).

(35) Genot, E. & Cantrell, D. A. Ras regulation and function in lymphocytes. *Curr Opin Immunol* **12**, 289-294 (2000).

(36) Kortum, R. L., Sommers, C. L., Alexander, C. P., Pinski, J. M., Li, W., Grinberg, A., Lee, J., Love, P. E. & Samelson, L. E. Targeted Sos1 deletion reveals its critical role in early T-cell development. *Proc Natl Acad Sci U S A* **108**, 12407-12412 (2011).

(37) Gureasko, J., Galush, W. J., Boykevisch, S., Sondermann, H., Bar-Sagi, D., Groves, J. T. & Kuriyan, J. Membrane-dependent signal integration by the Ras activator Son of sevenless. *Nature Structural & Molecular Biology* **15**, 452-461 (2008).

(38) Iversen, L., Tu, H.-L., Lin, W.-C., Christensen, S. M., Abel, S. M., Iwig, J., Wu, H.-J., Gureasko, J., Rhodes, C., Petit, R. S., Hansen, S. D., Thill, P., Yu, C.-H., Stamou, D., Chakraborty, A. K., Kuriyan, J. & Groves, J. T. Ras activation by SOS: Allosteric regulation by altered fluctuation dynamics. *Science* **345**, 50-54 (2014).

(39) Lee, Y. K., Low-Nam, S. T., Chung, J. K., Hansen, S. D., Lam, H. Y. M., Alvarez, S. & Groves, J. T. Mechanism of SOS PR-domain autoinhibition revealed by single-molecule assays on native protein from lysate. *Nat Commun* **8**, 15061 (2017).

(40) Bonvini, E., DeBell, K. E., Verí, M. C., Graham, L., Stoica, B., Laborda, J., Aman, M. J., DiBaldassarre, A., Miscia, S. & Rellahan, B. L. On the mechanism coupling phospholipase Cgamma1 to the B- and T-cell antigen receptors. *Adv Enzyme Regul* **43**, 245-269 (2003).

(41) Braiman, A., Barda-Saad, M., Sommers, C. L. & Samelson, L. E. Recruitment and activation of PLCgamma1 in T cells: a new insight into old domains. *Embo j* **25**, 774-784 (2006).

(42) Groves, J. T., Ulman, N. & Boxer, S. G. Micropatterning Fluid Lipid Bilayers on Solid Supports. *Science* **275**, 651-653 (1997).

(43) Galush, W. J., Nye, J. A. & Groves, J. T. Quantitative Fluorescence Microscopy Using Supported Lipid Bilayer Standards. *Biophysical Journal* **95**, 2512-2519 (2008).

(44) Cremer, P. S. & Boxer, S. G. Formation and Spreading of Lipid Bilayers on Planar Glass Supports. *The Journal of Physical Chemistry B* **103**, 2554-2559 (1999).

(45) Lin, W.-C., Yu, C.-H., Triffo, S. & Groves, J. T. Supported Membrane Formation, Characterization, Functionalization, and Patterning for Application in Biological Science and Technology. *Current Protocols in Chemical Biology* **2**, 235-269 (2010).

(46) Nair, P. M., Salaita, K., Petit, R. S. & Groves, J. T. Using patterned supported lipid membranes to investigate the role of receptor organization in intercellular signaling. *Nature Protocols* **6**, 523-539 (2011).

(47) Hardy, G. J., Nayak, R. & Zauscher, S. Model cell membranes: Techniques to form complex biomimetic supported lipid bilayers via vesicle fusion. *Current Opinion in Colloid & Interface Science* **18**, 448-458 (2013).

(48) Nye, J. A. & Groves, J. T. Kinetic Control of Histidine-Tagged Protein Surface Density on Supported Lipid Bilayers. *Langmuir* **24**, 4145-4149 (2008).

(49) Chung, J. K., Lee, Y. K., Denson, J.-P., Gillette, W. K., Alvarez, S., Stephen, A. G. & Groves, J. T. K-Ras4B Remains Monomeric on Membranes over a Wide Range of Surface Densities and Lipid Compositions. *Biophysical Journal* **114**, 137-145 (2018).

(50) Axelrod, D. Cell-substrate contacts illuminated by total internal reflection fluorescence. *J Cell Biol* **89**, 141-145 (1981).

(51) Axelrod, D. Total Internal Reflection Fluorescence Microscopy in Cell Biology. *Traffic* **2**, 764-774 (2001).

(52) Millis, B. A. in *Molecular Profiling: Methods and Protocols* (eds Virginia Espina & Lance A. Liotta) 295-309 (Humana Press, 2012).

(53) Poulter, N. S., Pitkeathly, W. T. E., Smith, P. J. & Rappoport, J. Z. in *Advanced Fluorescence Microscopy: Methods and Protocols* (ed Peter J. Verveer) 1-23 (Springer New York, 2015).

(54) Ditlev, J. A., Vega, A. R., Köster, D. V., Su, X., Tani, T., Lakoduk, A. M., Vale, R. D., Mayor, S., Jaqaman, K. & Rosen, M. K. A composition-dependent molecular clutch between T cell signaling condensates and actin. *eLife* **8**, e42695 (2019).

(55) Case, L. B., Ditlev, J. A. & Rosen, M. K. Regulation of Transmembrane Signaling by Phase Separation. *Annu Rev Biophys* **48**, 465-494 (2019).

(56) Maignan, S., Guilloteau, J.-P., Fromage, N., Arnoux, B., Becquart, J. & Ducruix, A. Crystal Structure of the Mammalian Grb2 Adaptor. *Science* **268**, 291-293 (1995).

(57) Lin, C.-W., Nocka, L. M., Stinger, B. L., DeGrandchamp, J. B., Lew, L. J. N., Alvarez, S., Phan, H. T., Kondo, Y., Kuriyan, J. & Groves, J. T. A two-component protein condensate of the EGFR cytoplasmic tail and Grb2 regulates Ras activation by SOS at the membrane. *Proceedings of the National Academy of Sciences* **119**, e2122531119 (2022).

(58) Zeng, L., Palaia, I., Šarić, A. & Su, X. PLCγ1 promotes phase separation of T cell signaling components. *Journal of Cell Biology* **220** (2021).

(59) Hajicek, N., Keith, N. C., Siraliev-Perez, E., Temple, B. R. S., Huang, W., Zhang, Q., Harden, T. K. & Sondek, J. Structural basis for the activation of PLC-γ isozymes by phosphorylation and cancer-associated mutations. *eLife* **8**, e51700 (2019).

(60) Gresset, A., Hicks, S. N., Harden, T. K. & Sondek, J. Mechanism of Phosphorylation-induced Activation of Phospholipase C-γ Isozymes. *Journal of Biological Chemistry* **285**, 35836-35847 (2010).

(61) Bunney, Tom D., Esposito, D., Mas-Droux, C., Lamber, E., Baxendale, Rhona W., Martins, M., Cole, A., Svergun, D., Driscoll, Paul C. & Katan, M. Structural and Functional Integration of the PLCγ Interaction Domains Critical for Regulatory Mechanisms and Signaling Deregulation. *Structure* **20**, 2062-2075 (2012).

(62) Hajicek, N., Charpentier, T. H., Rush, J. R., Harden, T. K. & Sondek, J. Autoinhibition and Phosphorylation-Induced Activation of Phospholipase C-γ Isozymes. *Biochemistry* **52**, 4810-4819 (2013).

(63) Liu, Y., Bunney, T. D., Khosa, S., Macé, K., Beckenbauer, K., Askwith, T., Maslen, S., Stubbs, C., de Oliveira, T. M., Sader, K., Skehel, M., Gavin, A.-C., Phillips, C. & Katan, M. Structural insights and activating mutations in diverse pathologies define mechanisms of deregulation for phospholipase C gamma enzymes. *EBioMedicine* **51**, 102607 (2020).

(64) Siraliev-Perez, E., Stariha, J. T. B., Hoffmann, R. M., Temple, B. R. S., Zhang, Q., Hajicek, N., Jenkins, M. L., Burke, J. E. & Sondek, J. Dynamics of allosteric regulation of the phospholipase C-γ isozymes upon recruitment to membranes. *eLife* **11**, e77809 (2022).

(65) Le Huray, K. I. P., Bunney, T. D., Pinotsis, N., Kalli, A. C. & Katan, M. Characterization of the membrane interactions of phospholipase Cγ reveals key features of the active enzyme. *Science Advances* **8**, eabp9688 (2022).

(66) Yablonski, D., Kuhne, M. R., Kadlecek, T. & Weiss, A. Uncoupling of Nonreceptor Tyrosine Kinases from PLC-γ1 in an SLP-76-Deficient T Cell. *Science* **281**, 413-416 (1998).

(67) Yablonski, D., Kadlecek, T. & Weiss, A. Identification of a Phospholipase C-γ1 (PLC-γ1) SH3 Domain-Binding Site in SLP-76 Required for T-Cell Receptor-Mediated Activation of PLC-γ1 and NFAT. *Molecular and Cellular Biology* **21**, 4208-4218 (2001).

(68) Singer, A. L., Bunnell, S. C., Obstfeld, A. E., Jordan, M. S., Wu, J. N., Myung, P. S., Samelson, L. E. & Koretzky, G. A. Roles of the Proline-rich Domain in SLP-76 Subcellular Localization and T Cell Function. *Journal of Biological Chemistry* **279**, 15481-15490 (2004).

(69) Beach, D., Gonen, R., Bogin, Y., Reischl, I. G. & Yablonski, D. Dual Role of SLP-76 in Mediating T Cell Receptor-induced Activation of Phospholipase C-γ1. *Journal of Biological Chemistry* **282**, 2937-2946 (2007).

(70) Lugassy, J., Corso, J., Beach, D., Petrik, T., Oellerich, T., Urlaub, H. & Yablonski, D. Modulation of TCR responsiveness by the Grb2-family adaptor, Gads. *Cellular Signalling* **27**, 125-134 (2015).

(71) Yablonski, D. Bridging the Gap: Modulatory Roles of the Grb2-Family Adaptor, Gads, in Cellular and Allergic Immune Responses. *Frontiers in Immunology* **10** (2019).

(72) Manna, A., Zhao, H., Wada, J., Balagopalan, L., Tagad, H. D., Appella, E., Schuck, P. & Samelson, L. E. Cooperative assembly of a four-molecule signaling complex formed upon T cell antigen receptor activation. *Proceedings of the National Academy of Sciences* **115**, E11914-E11923 (2018).

(73) Yi, J., Balagopalan, L., Nguyen, T., McIntire, K. M. & Samelson, L. E. TCR microclusters form spatially segregated domains and sequentially assemble in calcium-dependent kinetic steps. *Nature Communications* **10**, 277 (2019).

(74) Wada, J., Rathnayake, U., Jenkins, L. M., Singh, A., Mohammadi, M., Appella, E., Randazzo, P. A. & Samelson, L. E. In vitro reconstitution reveals cooperative mechanisms of adapter protein-mediated activation of phospholipase C-γ1 in T cells. *Journal of Biological Chemistry* **298** (2022).

(75) O'Dair, M. K. *Timing and Nucleation of Membrane Protein Condensation by Single Peptide-MHC:T Cell Receptor Complex Control Antigen Discrimination*, University of California, Berkeley, (2021).

(76) Melowic, H. R., Stahelin, R. V., Blatner, N. R., Tian, W., Hayashi, K., Altman, A. & Cho, W. Mechanism of Diacylglycerol-induced Membrane Targeting and Activation of Protein Kinase Cθ. *Journal of Biological Chemistry* **282**, 21467-21476 (2007).

(77) Rahman, G. M., Sanker, S., Lewin, N., Prasad, B. V. V., Blumberg, P. M. & Das, J. Identification of the activator binding residues in protein kinase C theta C1B domain. *The FASEB Journal* **26**, 749.742-749.742 (2012).

(78) Huse, M., Klein, L. O., Girvin, A. T., Faraj, J. M., Li, Q. J., Kuhns, M. S. & Davis, M. M. Spatial and temporal dynamics of T cell receptor signaling with a photoactivatable agonist. *Immunity* **27**, 76-88 (2007).

(79) Lin, C.-C., Suen, K. M., Jeffrey, P.-A., Wieteska, L., Lidster, J. A., Bao, P., Curd, A. P., Stainthorp, A., Seiler, C., Koss, H., Miska, E., Ahmed, Z., Evans, S. D., Molina-París, C. & Ladbury, J. E. Receptor tyrosine kinases regulate signal transduction through a liquid-liquid phase separated state. *Molecular Cell* **82**, 1089-1106.e1012 (2022).

(80) Hancock, J. F. Ras proteins: different signals from different locations. *Nature Reviews Molecular Cell Biology* **4**, 373-385 (2003).

(81) Parker, J. A. & Mattos, C. The K-Ras, N-Ras, and H-Ras Isoforms: Unique Conformational Preferences and Implications for Targeting Oncogenic Mutants. *Cold Spring Harb Perspect Med* **8** (2018).

(82) Janosi, L. & Gorfe, A. A. Segregation of Negatively Charged Phospholipids by the Polycationic and Farnesylated Membrane Anchor of Kras. *Biophysical Journal* **99**, 3666-3674 (2010).

(83) Zhou, Y., Prakash, P., Gorfe, A. A. & Hancock, J. F. Ras and the Plasma Membrane: A Complicated Relationship. *Cold Spring Harb Perspect Med* **8** (2018).

(84) Cao, S., Chung, S., Kim, S., Li, Z., Manor, D. & Buck, M. K-Ras G-domain binding with signaling lipid phosphatidylinositol (4,5)-phosphate (PIP2): membrane association, protein orientation, and function. *Journal of Biological Chemistry* **294**, 7068-7084 (2019).

(85) Ingólfsson, H. I., et. al. Machine learning–driven multiscale modeling reveals lipid-dependent dynamics of RAS signaling proteins. *Proceedings of the National Academy of Sciences* **119**, e2113297119 (2022).

(86) Shrestha, R., Chen, D., Frank, P., Nissley, D. V. & Turbyville, T. J. Recapitulation of cell-like KRAS4b membrane dynamics on complex biomimetic membranes. *iScience* **25**, 103608 (2022).

(87) Brangwynne, C. P., Eckmann, C. R., Courson, D. S., Rybarska, A., Hoege, C., Gharakhani, J., Jülicher, F. & Hyman, A. A. Germline P Granules Are Liquid Droplets That Localize by Controlled Dissolution/Condensation. *Science* **324**, 1729-1732 (2009).

(88) Li, P., Banjade, S., Cheng, H.-C., Kim, S., Chen, B., Guo, L., Llaguno, M., Hollingsworth, J. V., King, D. S., Banani, S. F., Russo, P. S., Jiang, Q.-X., Nixon, B. T. & Rosen, M. K. Phase transitions in the assembly of multivalent signalling proteins. *Nature* **483**, 336-340 (2012).

(89) Case, L. B., Zhang, X., Ditlev, J. A. & Rosen, M. K. Stoichiometry controls activity of phase-separated clusters of actin signaling proteins. *Science* **363**, 1093-1097 (2019).

(90) Jaqaman, K. & Ditlev, J. A. Biomolecular condensates in membrane receptor signaling. *Current Opinion in Cell Biology* **69**, 48-54 (2021).

(91) Huang, W. Y. C., Alvarez, S., Kondo, Y., Kuriyan, J. & Groves, J. T. Relating cellular signaling timescales to single-molecule kinetics: A first-passage time analysis of Ras activation by SOS. *Proceedings of the National Academy of Sciences* **118**, e2103598118 (2021).

(92) Ahmed, Z., Timsah, Z., Suen, K. M., Cook, N. P., Lee, G. R., Lin, C.-C., Gagea, M., Marti, A. A. & Ladbury, J. E. Grb2 monomer–dimer equilibrium determines normal versus oncogenic function. *Nature Communications* **6**, 7354 (2015).

(93) Lo, W.-L., Shah, N. H., Rubin, S. A., Zhang, W., Horkova, V., Fallahee, I. R., Stepanek, O., Zon, L. I., Kuriyan, J. & Weiss, A. Slow phosphorylation of a tyrosine residue in LAT optimizes T cell ligand discrimination. *Nature Immunology* **20**, 1481-1493 (2019).

(94) Sicheri, F., Moarefi, I. & Kuriyan, J. Crystal structure of the Src family tyrosine kinase Hck. *Nature* **385**, 602-609 (1997).

(95) Seeliger, M. A., Young, M., Henderson, M. N., Pellicena, P., King, D. S., Falick, A. M. & Kuriyan, J. High yield bacterial expression of active c-Abl and c-Src tyrosine kinases. *Protein Science* **14**, 3135-3139 (2005).

(96) Huang, W. Y. C., Ditlev, J. A., Chiang, H.-K., Rosen, M. K. & Groves, J. T. Allosteric Modulation of Grb2 Recruitment to the Intrinsically Disordered Scaffold Protein, LAT, by Remote Site Phosphorylation. *Journal of the American Chemical Society* **139**, 18009-18015 (2017).

(97) Hughes, L. D., Rawle, R. J. & Boxer, S. G. Choose Your Label Wisely: Water-Soluble Fluorophores Often Interact with Lipid Bilayers. *PLOS ONE* **9**, e87649 (2014).

(98) Lam, K. & Tajkhorshid, E. Membrane Interactions of Cy3 and Cy5 Fluorophores and Their Effects on Membrane-Protein Dynamics. *Biophysical Journal* **119**, 24-34 (2020).

(99) Li, G., Huang, Z., Zhang, C., Dong, B.-J., Guo, R.-H., Yue, H.-W., Yan, L.-T. & Xing, X.-H. Construction of a linker library with widely controllable flexibility for fusion protein design. *Applied Microbiology and Biotechnology* **100**, 215-225 (2016).

(100) Shah, N. H., Wang, Q., Yan, Q., Karandur, D., Kadlecek, T. A., Fallahee, I. R., Russ, W. P., Ranganathan, R., Weiss, A. & Kuriyan, J. An electrostatic selection mechanism controls sequential kinase signaling downstream of the T cell receptor. *eLife* **5**, e20105 (2016).

(101) McDonald, C. B., Balke, J. E., Bhat, V., Mikles, D. C., Deegan, B. J., Seldeen, K. L. & Farooq, A. Multivalent Binding and Facilitated Diffusion Account for the Formation of the Grb2–Sos1 Signaling Complex in a Cooperative Manner. *Biochemistry* **51**, 2122-2135 (2012).

(102) McDonald, C. B., Seldeen, K. L., Deegan, B. J., Lewis, M. S. & Farooq, A. Grb2 adaptor undergoes conformational change upon dimerization. *Archives of Biochemistry and Biophysics* **475**, 25-35 (2008).

(103) Schiering, N., Casale, E., Caccia, P., Giordano, P. & Battistini, C. Dimer Formation through Domain Swapping in the Crystal Structure of the Grb2-SH2−Ac-pYVNV Complex. *Biochemistry* **39**, 13376-13382 (2000).

(104) Benfield, A. P., Whiddon, B. B., Clements, J. H. & Martin, S. F. Structural and energetic aspects of Grb2-SH2 domain-swapping. *Archives of Biochemistry and Biophysics* **462**, 47-53 (2007).

(105) Papaioannou, D., Geibel, S., Kunze, M. B. A., Kay, C. W. M. & Waksman, G. Structural and biophysical investigation of the interaction of a mutant Grb2 SH2 domain (W121G) with its cognate phosphopeptide. *Protein Science* **25**, 627-637 (2016).

(106) Hosoe, Y., Numoto, N., Inaba, S., Ogawa, S., Morii, H., Abe, R., Ito, N. & Oda, M. Structural and functional properties of Grb2 SH2 dimer in CD28 binding. *Biophysics and Physicobiology* **16**, 80-88 (2019).

(107) Cruz-Orcutt, N., Vacaflores, A., Connolly, S. F., Bunnell, S. C. & Houtman, J. C. D. Activated PLC-γ1 is catalytically induced at LAT but activated PLC-γ1 is localized at both LAT- and TCR-containing complexes. *Cellular Signalling* **26**, 797-805 (2014).

(108) Invitrogen. in *Example calculations. MAN0019835* (ThermoFisher Scientific, 2021). https://www.thermofisher.com/document-connect/document-connect.html?url=https://assets.thermofisher.com/TFS-Assets%2FLSG%2Fmanuals%2FMAN0019835_AlexaFluor_ProteinLabelingKits_UG.pdf

(109) Edelstein, A., Amodaj, N., Hoover, K., Vale, R. & Stuurman, N. Computer Control of Microscopes Using μManager. *Current Protocols in Molecular Biology* **92**, 14.20.11-14.20.17 (2010).

(110) Hansen, S. D., Huang, W. Y. C., Lee, Y. K., Bieling, P., Christensen, S. M. & Groves, J. T. Stochastic geometry sensing and polarization in a lipid kinase–phosphatase competitive reaction. *Proceedings of the National Academy of Sciences* **116**, 15013-15022 (2019).

(111) Cho, S., Velikovsky, C. A., Swaminathan, C. P., Houtman, J. C., Samelson, L. E. & Mariuzza, R. A. Structural basis for differential recognition of tyrosine-phosphorylated sites in the linker for activation of T cells (LAT) by the adaptor Gads. *The EMBO Journal* **23**, 1441-1451 (2004).

(112) Verger, R., Mieras, M. C. E. & de Haas, G. H. Action of Phospholipase A at Interfaces. *Journal of Biological Chemistry* **248**, 4023-4034 (1973).

(113) Serrano, C. J., Graham, L., DeBell, K., Rawat, R., Veri, M. C., Bonvini, E., Rellahan, B. L. & Reischl, I. G. A New Tyrosine Phosphorylation Site in PLCγ1: The Role of Tyrosine 775 in Immune Receptor Signaling. *The Journal of Immunology* **174**, 6233-6237 (2005).

(114) Nocka, L. M., Groves, J. T. & Kuriyan, J. Stimulation of the catalytic activity of the tyrosine kinase Btk by the adaptor protein Grb2. *bioRxiv*, 2022.2008.2025.505243 (2022).

(115) Cho, W., Digman, M., Ananthanarayanan, B. & Stahelin, R. V. in *Protein Kinase C Protocols* (ed Alexandra C. Newton) 291-298 (Humana Press, 2003).

(116) Yan, Q., Barros, T., Visperas, P. R., Deindl, S., Kadlecek, T. A., Weiss, A. & Kuriyan, J. Structural basis for activation of ZAP-70 by phosphorylation of the SH2-kinase linker. *Mol Cell Biol* **33**, 2188-2201 (2013).

(117) Schindelin, J., Arganda-Carreras, I., Frise, E., Kaynig, V., Longair, M., Pietzsch, T., Preibisch, S., Rueden, C., Saalfeld, S., Schmid, B., Tinevez, J.-Y., White, D. J., Hartenstein, V., Eliceiri, K., Tomancak, P. & Cardona, A. Fiji: an open-source platform for biological-image analysis. *Nature Methods* **9**, 676-682 (2012).

(118) Tinevez, J.-Y., Perry, N., Schindelin, J., Hoopes, G. M., Reynolds, G. D., Laplantine, E., Bednarek, S. Y., Shorte, S. L. & Eliceiri, K. W. TrackMate: An open and extensible platform for single-particle tracking. *Methods* **115**, 80-90 (2017).

(119) Goswami, D., Chen, D., Yang, Y., Gudla, P. R., Columbus, J., Worthy, K., Rigby, M., Wheeler, M., Mukhopadhyay, S., Powell, K., Burgan, W., Wall, V., Esposito, D., Simanshu, D. K., Lightstone, F. C., Nissley, D. V., McCormick, F. & Turbyville, T. Membrane interactions of the globular domain and the hypervariable region of KRAS4b define its unique diffusion behavior. *eLife* **9**, e47654 (2020).

(120) Huang, W. Y. C., Chiang, H.-K. & Groves, J. T. Dynamic Scaling Analysis of Molecular Motion within the LAT:Grb2:SOS Protein Network on Membranes. *Biophysical Journal* **113**, 1807-1813 (2017).

(121) Lin, W.-C., Iversen, L., Tu, H.-L., Rhodes, C., Christensen, S. M., Iwig, J. S., Hansen, S. D., Huang, W. Y. C. & Groves, J. T. H-Ras forms dimers on membrane surfaces via a protein–protein interface. *Proceedings of the National Academy of Sciences* **111**, 2996-3001 (2014).

(122) Lindén, M., Ćurić, V., Amselem, E. & Elf, J. Pointwise error estimates in localization microscopy. *Nature Communications* **8**, 15115 (2017).

(123) English, B. & Singer, R. *A three-camera imaging microscope for high-speed single-molecule tracking and super-resolution imaging in living cells*. Vol. 9550 OPN (SPIE, 2015).

(124) Xiang, L., Chen, K., Yan, R., Li, W. & Xu, K. Single-molecule displacement mapping unveils nanoscale heterogeneities in intracellular diffusivity. *Nature Methods* **17**, 524-530 (2020).

(125) Yan, R., Chen, K. & Xu, K. Probing Nanoscale Diffusional Heterogeneities in Cellular Membranes through Multidimensional Single-Molecule and Super-Resolution Microscopy. *Journal of the American Chemical Society* **142**, 18866-18873 (2020).